ENHANCED CATALYTIC ACTIVITIES OF NANOSTRUCTURED MATERIALS

A Dissertation

by

JULIBETH MILENA MARTINEZ DE LA HOZ

Submitted to the Office of Graduate and Professional Studies of
Texas A&M University
in partial fulfillment of the requirements for the degree of

DOCTOR OF PHILOSOPHY

Chair of Committee,	Perla B. Balbuena
Committee Members,	Zhengdong Cheng
	Jorge Seminario
	Haiyan Wang
Head of Department,	Ibrahim Karaman

December 2014

Major Subject: Materials Science and Engineering

ABSTRACT

Catalysis has enabled the development of very important industrial processes, especially those related to the petroleum and chemical industries. This has led to a significant influence in the worldwide economy, with 20% of it depending on catalysis. Current reliance of the industrial world on catalysis and rapidly increasing worldwide energy prices have motivated the search for improved catalysts allowing more energy-efficient processes. Catalysts performance is affected by the shape, structure, and chemical composition of the catalysts. Fortunately, the development of nanotechnology has allowed researchers to control the structure and morphology of catalyst nanoparticles, as well as that of solid supports. Even though, these approaches have enhanced the reactivity of materials towards specific reactions, there is still much more room for improvement. In this work, the incorporation of *electron-rich* environments into the structure of nanocatalysts is proposed as a new approach for the enhancement of the catalytic activity of nanomaterials. This study is conducted in its entirety using computational quantum-based simulations.

The effect of electron-rich regions on activation barriers for the dissociation of diatomic molecules is studied using metallic slit-type pores, finding that electron-rich environments enhance the reactivity of nanomaterials by reducing activation barriers required for the dissociation of molecules. The influence of electronic and geometric effects in the pores is also evaluated. It is found that local geometric characteristics, such as stacking planes forming the pore, and the presence of step-like defects influence adsorption energies and barriers for dissociation of molecules. Additionally, electrons inside the metallic pores have energies close to the Fermi-energy of the metal surfaces, which may allow tuning their energies for interactions with LUMO anti-bonding orbitals of specific molecules.

Subsequently, electron-rich regions are incorporated into a 3D nanostructured material (Pt_{22}/NPG). This proposed catalyst shows enhanced reactivity towards the dissociation of gas-phase molecules. Additionally, Pt_{22}/NPG may display enhanced reactivity, even when electron-rich regions do not interact with the molecules of interest, due to the good dispersion of Pt-clusters. Therefore, the incorporation of electron-rich environments into nanocatalysts is shown to be an efficient approach for the enhancement of the catalytic activity of nanomaterials.

ACKNOWLEDGEMENTS

I would like to thank my committee members, Dr. Cheng, Dr. Wang, and Dr. Seminario, for their guidance and support throughout the course of this research. Special thanks to Dr. Balbuena, who has been an excellent professor and leader. Thank you for all of your support and patience, thank you for teaching me how to be a researcher, and above all, thank you for teaching with your example how to become a better person.

Thanks also go to my friends and colleagues and the department faculty and staff for making my time at Texas A&M University a great experience. Finally, thanks to my mother, father, and siblings for their encouragement and to my husband for his patience and love.

TABLE OF CONTENTS

Page

LIST OF FIGURES

Page

LIST OF TABLES

Page

1. INTRODUCTION

Catalysis has enabled the development of very important industrial processes over the past decades, especially those related to the petroleum and chemical industries. Currently, petroleum refining is carried out almost entirely with the help of catalytic processes, as well as the production of important chemicals such as ammonia, sulfuric, and nitric-acids.[1] This has led to a significant influence in the worldwide economy, with 20% of it depending directly or indirectly on catalysis.[1,2] Among the different types of catalytic processes, heterogeneous catalysis is undoubtedly the most utilized form (80% of all catalytic processes), mainly due to its high turnover to yield products and low deactivation rates.[1]

Current reliance of the industrial world on heterogeneous catalysis and rapidly increasing worldwide energy prices have motivated the search for improved catalysts, allowing processes to take place in more energy-efficient ways. Traditionally, heterogeneous catalysis takes place on the surface of solid nanoparticles dispersed on high surface-area materials. Catalyst performance is directly affected by factors such as the shape, structure, and chemical composition of the catalyst and/or support.[2] Fortunately, the development of nanotechnology has allowed researchers to control, at the atomic level, the structure and morphology of catalyst nanoparticles as well as those of solid substrates. Nanocatalysts can now be made with tailored reactivity, and with much more homogenous structures. Nanoparticle size distributions can be held around narrow values for nanoparticle size-dependent reactions,[3-5] nanochanels in catalysts such as zeolites can be built with specific size/morphology for the interaction with particular molecules,[6-10] much better dispersion of nanoparticles in solid supports can now be obtained,[11-14] and solid supports can easily be doped with species such as lithium, nitrogen, or oxygen.[15-20] Although these approaches have resulted in enhanced reactivity of materials towards specific reactions, there is still much more room for improvement.

In this work, a new approach is proposed for the enhancement of the catalytic activity of nanostructured materials. This approach consists of the incorporation of *electron-rich* environments into the structure of the nanocatalyst. Electron-rich environments are spatial regions in which finite electronic densities are present. They are formed when two metallic nanostructures are in close proximity to one another.[21-30] The electron potential barrier between nanostructures decreases at subnanometer separations, and quantum effects become important, allowing the tunneling of some of the conduction electrons to the gap between nanostructures. Several experimental and theoretical works have reported the formation of a conductive channel in the interparticle region between metallic nanoparticles, as a result of migration of electrons to this gap.[21-30] This phenomenon is strongly dependent on the gap distance; small but finite electronic densities have been calculated for interparticle distances below 7 Å.[29] For even smaller separations, the electronic coupling becomes stronger, allowing higher electronic densities to be present at the interparticle region.[21-23,25-27,31]

Previous investigations found that interaction of gas-phase adsorbates with *electron-rich* regions results in interesting phenomena, such as the conversion of ethylene into a radical anion ready to initiate polymerization,[27] and the facilitation of the dissociation of oxygen molecules.[31] Additionally, Corma et al revealed that enhanced catalytic activity of zeolites may be a result of electronic confinement of molecules inside microscopic pores.[32] When channels in the zeolite have a similar size to that of guest molecules, modification of the electronic orbitals of the molecules and changes in their energy levels are induced due to interaction with delocalized electronic clouds of the lattice. As a result, pre-activation of molecules inside the channels is observed, enhancing the catalytic activity of host zeolites. Based on these results, it is postulated as the *hypothesis* of this work that catalyzed reactions taking place in the presence of electron-rich environments will require lower energy barriers, thereby improving the performance of catalysts.

The specific *goals* of this work involve (i) proving the hypothesis using as the pore model two metallic surfaces interacting at subnanometer separations (4-7 Å), (ii) understanding the different geometric and electronic effects that may be present in these types of metallic pores and their effect on the reactivity of the material, and finally, (iii) proposing a nanostructured material in which electron-rich regions are incorporated, and testing its reactivity towards specific reactions. The electron-rich regions must be incorporated in such a way that channels and/or pores in the material do not hinder the diffusion of reactants and products, a problem that has been widely reported in zeolite-type catalysts.[2]

Goals (i) to (iii) are achieved with the help of atomistic, quantum-based simulations. Computational methods allow studying molecular processes in detail, taking into account the high complexity of catalysts used in real processes. A wide range of information can be derived from quantum-based simulations, including surface reaction rates, adsorption geometries and energies, diffusion rates, charge densities, electronic density of states, phonon spectrum and vibrational properties, among others. In most cases, the experimental determination of these properties is still challenging.[33] Therefore, computational tools constitute a key strategy to understand the underlying mechanisms of chemical reactions, and to develop novel, cutting-edge technologies.

This dissertation is organized as follows: section two describes the general principles governing the computational methods employed in this work, including ab-initio Hartree-based simulations, density functional theory (DFT), and ab-initio Molecular Dynamics (AIMD). Section three describes how goal (i) is achieved. Specifically, two metallic surfaces interacting at 4.9 Å are used to generate an electron-rich region in the gap between them. These slit-type pores are formed using different transition metals, including Pt, Ir, Rh, Ni, and Pd. Subsequently, activation barriers for the dissociation of diatomic molecules are calculated inside these *pores* and compared to those of the same molecules dissociating on a single surface of the given metal. At the end of the section,

the hypothesis is proved, i.e., it is shown that catalyzed reactions taking place in the presence of electron-rich environments require lower energy barriers.

Successively, sections four and five help achieve goal (ii). Section four sheds light on the effect of local geometry of metallic pores on adsorption strengths and barriers for molecular dissociation. The adsorption and dissociation of molecular oxygen is studied in platinum slit-pores formed by different stacking planes, and/or in the presence of step-like defects. The role that local surface geometry plays on the reactivity of metallic pores is clearly established at the end of this chapter. Section five analyzes the electronic changes experienced by the system as the metallic surfaces approach each other and their relation with the specific metal forming the pore. Precisely, electronic densities of states of several transition metal nanopores are calculated for different pore sizes (i.e., surface−surface separations). Results in this section clearly define the energetic state of electrons inside the different metallic pores. This information may allow effective electron transfer from the electron-rich region to the lowest unoccupied molecular orbital (LUMO) of molecules of interest.

Chapter six focuses on the incorporation of electron-rich regions as building blocks in a three-dimensional nanostructured material, and the evaluation of its reactivity (goal (iii)). The chosen nanomaterial is a Nanopillared graphene structure (NPG) decorated with metallic nanoparticles. The chapter describes how electron-rich regions are formed in the material, their expected electronic densities, and the enhancement given by them to the dissociation of molecular oxygen, carbon monoxide, molecular nitrogen, and methane. Lastly, Chapter seven presents the conclusions of this work, and future work suggested for further understanding of the role that electron-rich regions play in catalysis, as well as new ways in which their effect can be exploited.

2. COMPUTATIONAL QUANTUM CHEMISTRY METHODS

2.1.The Schrödinger Equation

An adequate description of molecular systems, such as those found in surface science and catalysis, involve a direct consideration of atoms and its elementary particles, e.g., protons and electrons. These particles display a "wave-like" behavior that is properly described by a probability function known as the "wave-function", Ψ, whose mathematical expression results in one of the fundamental equations of quantum mechanics, i.e., the Schrödinger equation:

$$\hat{H}\,\Psi(r) = E\,\Psi(r) \tag{2.1}$$

Equation 2.1 is the time-independent Schrödinger equation, which describes stationary systems by omitting the time variable in the probability function, Ψ. $\hat{H}$ is the Hamiltonian operator, and E is the eigenvalue of the Hamiltonian or ground state energy of the material. The exact solution of this equation would yield the electronic distribution of the system under consideration, permitting the evaluation of physical observables related to its electronic structure.

In order to solve equation 2.1, the precise form of the Hamiltonian operator must be known. The non-relativistic Hamiltonian is obtained from the classic kinetic and potential energy contributions of nuclei and electrons:

$$\hat{H} = \hat{T}_N + \hat{T}_E + \hat{V}_{NE} + \hat{V}_{NN} + \hat{V}_{EE} \tag{2.2}$$

The different terms on the right-hand side of equation 2.2 correspond to the kinetic energy operator for nuclei, kinetic energy operator for electrons, and potential energy operators describing electrostatic interactions between electrons-nuclei, nuclei-nuclei,

and electrons-electrons, respectively. For a system with N nuclei and L electrons, the kinetic energy operators, $\hat{\mathrm{T}}_{\mathrm{N}}$ and $\hat{\mathrm{T}}_{\mathrm{E}}$, are written in terms of the momentum operator $(\hbar/i)\vec{\nabla}$ and the mass of electrons and nuclei, M_E and M_N, respectively:

$$\hat{\mathrm{T}}_{\mathrm{N}} = -\sum_{k=1}^{N} \frac{\hbar^2}{2M_{N,k}} \nabla^2 \tag{2.3}$$

$$\hat{\mathrm{T}}_{\mathrm{E}} = -\sum_{k=1}^{L} \frac{\hbar^2}{2M_{E,k}} \nabla^2 \tag{2.4}$$

On the other hand, the potential energy operators describe simple electrostatic interactions resulting from pairs of charged nuclei and/or electrons (charges *Z* and *e*, and spatial positions $\vec{R}$ and $\vec{r}$, respectively):

$$\hat{\mathrm{V}}_{\mathrm{NE}} = -\sum_{k=1}^{L} \sum_{i=1}^{N} \frac{1}{4\pi\varepsilon_0} \frac{Z_k e^2}{|\overrightarrow{R_k} - \overrightarrow{r_i}|} \tag{2.5}$$

$$\hat{\mathrm{V}}_{\mathrm{NN}} = \frac{1}{2} \sum_{k_1 \neq k_2=1}^{N} \frac{1}{4\pi\varepsilon_0} \frac{Z_{k1} Z_{k2} e^2}{|\overrightarrow{R_{k1}} - \overrightarrow{R_{k2}}|} \tag{2.6}$$

$$\hat{\mathrm{V}}_{\mathrm{EE}} = \frac{1}{2} \sum_{i_1 \neq i_2=1}^{L} \frac{1}{4\pi\varepsilon_0} \frac{e^2}{|\overrightarrow{r_{i1}} - \overrightarrow{r_{i2}}|} \tag{2.7}$$

Even though equations 2.3-2.7 define explicitly the total Hamiltonian operator, equation 2.1 can only be solved exactly in a few selected simple cases. This is because the solution, Ψ, to this equation is a very complicated function that depends on 3L position coordinates of the L electrons, L spin coordinates of the electrons, and 3N position coordinates of the nuclei.[34] Consequently, some approximations are needed to simplify the problem and make equation 2.1 solvable within reasonable accuracy.

2.2.Born-Oppenheimer Approximation

This approximation separates nuclei and electrons into two different mathematical problems. Nuclei are much heavier than electrons, a reasonable justification to this physical observation can be made through the uncertainty principle or even using classical statistical mechanics, both of which lead to $M_E/M_N << 1$.[34] Thus, electrons are expected to move much faster, and for each nuclei movement electrons *instantly* adapt their ground state. This assumption permits expressing the wave-function, Ψ, as the product of a nuclei wave-function and an electronic wave-function:

$$\Psi (R, r) = \Psi (R). \Psi (r) \tag{2.8}$$

Ψ (R) and Ψ (r), are obtained by solving two separate Schrödinger equations. In the one for the nuclei, the Hamiltonian is composed of the terms in equations 2.3 and 2.6. However, the kinetic energy of nuclei is usually neglected, resulting in a nuclei energy (E_{nuclei}) defined solely by the electrostatic interactions among nuclei. On the other hand, the electronic Hamiltonian is composed of the terms in equations 2.4, 2.5, and 2.7:

$$\frac{1}{2}\sum_{k_1\neq k_2=1}^{N}\frac{1}{4\pi\varepsilon_0}\frac{Z_{k1}Z_{k2}e^2}{|\overrightarrow{R_{k1}}-\overrightarrow{R_{k2}}|} = E_{\text{nuclei}}(R) \tag{2.1.a}$$

$$[\hat{T}_E + \hat{V}_{EE} + \hat{V}_{NE}]\,\Psi (r) = E_{\text{electrons}}\,\Psi (r) \tag{2.1.b}$$

The total energy of the system is obtained by adding the nuclei and the electronic contributions, E_{nuclei} and $E_{\text{electrons}}$, respectively.

When theoretically optimizing a structure, the ground state or lowest energy of the system is searched. This is done by first, defining a set of fixed nuclei coordinates, which easily allows solving equation 2.1.a and finding the E_{nuclei} contribution. Moreover, since the nuclei coordinates are present in the operator $\hat{V}_{NE}$ of equation 2.1.b, they also

act as parameters generating an electrostatic potential in which electrons are moving. Once equation 2.1.b is solved and $E_{\text{electrons}}$ is known, the total energy of the system for that set of nuclei coordinates is calculated. Subsequently, a new set of nuclear coordinates can be generated by using the gradient of the total energy on the nuclei. Assuming there are no external fields, the Hellmann-Freynman theorem suggest that the force acting on a given nucleus ($F_{n,i}$) will correspond to the exact computed electrostatic potential due to interaction with electrons and other nuclei:[35]

$$F_{n,\,i} = -\frac{\partial}{\partial R_i} E(R_i) = -\frac{d}{dR_i}\langle \Psi | \hat{H} | \Psi \rangle = -\int \rho_R(r) \frac{\partial}{\partial R_i} \hat{V}_{NE}\, dr - \frac{\partial}{\partial R_i} \hat{V}_{NN} \qquad (2.9)$$

The new set of nuclear coordinates is then used to solve equations 2.1.a and 2.1.b again, and the process is repeated until the total calculated energy is lowest (usually the stopping criteria is based on a tolerance value set for $E_{total,\,j} - E_{total,\,j-1}$). Figure 2.1 schematizes the geometry optimization process described. This process does not explain, however, how equation 2.1.b is solved. The solution to the electronic equation, Ψ (r), is still a very complicated function that depends on 3L position coordinates of the L electrons, and their L spin coordinates. In the next sections further approximations employed to make equation 2.1.b solvable will be briefly reviewed, and self-consistent algorithms proposed to solve it will be presented in sections 2.6 (HF-based) and 2.8.4 (DFT-based).

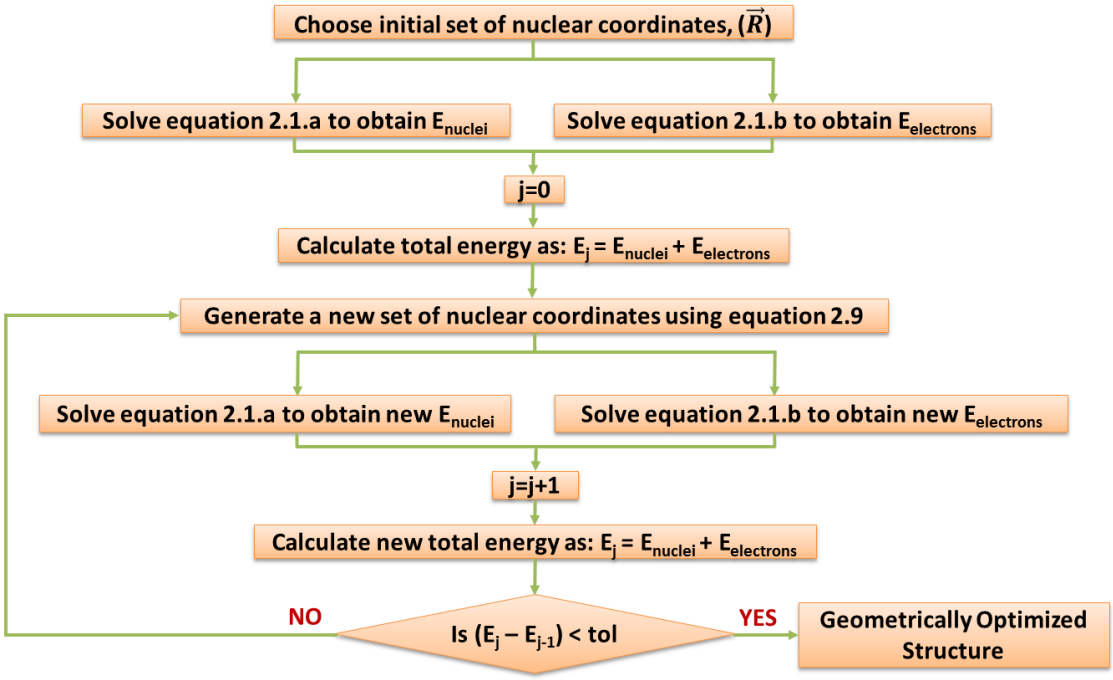

Figure 2.1 Theoretical geometry optimization process described in section 2.2

2.3.The Hartree Product

The goal of this approach is to simplify the electronic wave-function, Ψ (r), by expressing it as a function of individual orbitals, ψ_i (r_i), each one containing a single electron. In this manner, the wave-function of an L-electron system will be formed as the product of L different individual probability functions, ψ_i (r_i):

$$\Psi(r) = \frac{1}{\sqrt{L!}} [\psi_1(r_1).\psi_2(r_2).\ \psi_3(r_3)\ldots\psi_L(r_L)] \qquad (2.10)$$

Equation 2.10 is known as the Hartree product, and it implies that electrons can move as independent particles in the system. For this reason, this approach is also known as the

independent particle approximation.[36] Each individual wave-function, ψ_i (r_i), can be calculated from a one-electron Schrödinger equation:

$$\hat{h}\ \psi_i\ (r_i) = E_i\ \psi_i\ (r_i) \tag{2.11}$$

The Hamiltonian operator, $\hat{h}$, acting on the single particle wave-functions, is defined equivalently to that in equation 2.1.b: $\hat{h} = \hat{T}_E + \hat{V}_{EE} + \hat{V}_{NE}$, and the total electronic energy corresponds to the sum of the individual contributions:

$$E_{electrons} = E_1 + E_2 + E_3 + \ldots + E_L \tag{2.12}$$

Although the Hartree product simplifies the calculation of Ψ (r), it does not take into account the Pauli antisymmetry principle for fermions (electrons), which requires an antisymmetric wave-function describing an L-electron system. In other words, the wave-function must change sign if two electrons exchange places.[37] Accordingly, a better approximation is needed to properly describe the antisymmetric behavior of electronic wave-functions.

2.4.The Hartree-Fock Method (HF)

This method improves the Hartree product by expressing the electronic wave-function as a determinant of the individual electronic orbitals (*Slater* determinant):

$$\Psi\ (r) = \frac{1}{\sqrt{L!}} \begin{vmatrix} \psi 1\ (r1) & \psi 2\ (r1). \cdots \psi L\ (r1) \\ \vdots & \vdots \quad \ddots \quad \vdots \\ \psi 1\ (rL) & \psi 2\ (rL). \cdots \psi L\ (rL) \end{vmatrix}$$

The Slater determinant satisfies the Pauli Exclusion Principle, changing sings if two electrons are exchanged. After incorporating this determinant into the one-electron Schrödinger equation, 2.11, the potential energy operator describing electron-electron interactions takes the following form:[34]

$$\hat{V}_{EE} = \sum_{i=1}^{L}(\hat{J}_i - \hat{K}_i) \tag{2.13}$$

$\hat{J}_i$ and $\hat{K}_i$ are called the *Coulomb* and *Exchange* operators, respectively. The first one, describe electrostatic interactions between different individual orbitals, $|\psi_i|^2$ and $|\psi_k|^2$, while the second operator is a result of the required antisymmetric property of electronic wave-functions:

$$\hat{J}_i = \int \frac{|\psi_i(\vec{r}_2)|^2}{|\vec{r}_2 - \vec{r}_1|} d\vec{r}_2 \psi_k(\vec{r}_1) \tag{2.14}$$

$$\hat{K}_i = \int \frac{\psi_i^*(\vec{r}_2)\vec{P}_{12}[\psi_i(\vec{r}_2)\psi_k(\vec{r}_1)]}{|\vec{r}_2 - \vec{r}_1|} d\vec{r}_2 \tag{2.15}$$

Using these operators, equation 2.11 is now expressed as:

$$[\hat{T}_E + \hat{V}_{NE} + \sum_{i=1}^{L}(\hat{J}_i - \hat{K}_i)]\ \psi_i(r_i) = E_i\ \psi_i(r_i) \tag{2.16}$$

Operators $\hat{T}_E$ and $\hat{V}_{NE}$ are still defined by equations 2.4 and 2.5 but adopting a simpler form since they are evaluating a single electron and the summation from 1 to L is not needed. Moreover, defining a *Fock* operator as $\hat{F} = \hat{T}_E + \hat{V}_{NE} + \sum_{i=1}^{L}(\hat{J}_i - \hat{K}_i)$, equation 2.11 takes the simple form:

$$\hat{F}\ \psi_i(r_i) = E_i\ \psi_i(r_i) \tag{2.17}$$

The equation above is known as the *Hartree-Fock equation*. The next step required to reach a numerical solution for equation 2.17, involves expressing the individual wave-functions (present in the definition of the Coulomb and Exchange operators) in a practical, efficient way. An interesting alternative was proposed by Roothan, and it will be described in the next section.

2.5.The Hartree-Fock-Roothan Method

Roothan proposed for individual electronic orbitals, ψ_i, to be approximated as a linear combination of *basis functions*, ϕ_i*:*

$$\psi_i (r_i) = \sum_{j=1}^{S} \phi_i(r_i)\alpha_{j,i} \quad (2.18)$$

The basis functions (ϕ_i) and their number (S) are predetermined, leaving the expansion coefficients ($\alpha_{j,i}$) as the only parameters to be varied. Since this is an approximation, the accuracy with which equation 2.18 represents the real electronic orbitals depends on the choice of basis functions. In sections 2.5.1 to 2.5.3, the most common type of basis functions will be briefly presented.

2.5.1. Slater-Type Functions

Basis functions of this type have a similar form to the solution of the Schrödinger equation calculated for hydrogen, consisting of a radial function multiplying an angular function part (spherical harmonics):[36]

$$\phi_i(r_i) = R_{nl}(r_i)Y_{lm}(\theta,\phi) \quad (2.19)$$

Slater-type functions express the radial part, R_{nl}, as a Laguerre polynomial multiplied by an exponential function:[34]

$$R_{nl}(r_i) = \frac{(2\xi)^{n+1/2}}{(2n!)^{1/2}} r_i^{n-1} e^{-\xi r_i} \quad (2.20)$$

A disadvantage of Slater-type functions in that they lead to numerical problems during integration, especially in systems with a large number of electrons.[36]

2.5.2. Gaussian-Type Functions

These functions are much more commonly employed than Slater functions, mainly because they are numerically easier to handle. In this case, the radial part in equation 2.19 is expressed as:

$$R_{nl}(r_i) = 2^{n+1} \frac{\phi^{(2n+1)/4}}{[(2n-1)!!]\frac{1}{2}(2\pi)^{1/4}} r_i^{n-1} e^{-\phi r^2} \quad (2.21)$$

Usually, at least three Gaussian type functions are required to reach the same level of accuracy describing electronic orbitals as with one Slater-type function.[36]

2.5.3. Plane Waves

While Slater- and Gaussian-type functions are localized and suitable to describe small groups of atoms and molecules, plane waves are completely delocalized functions more appropriate for the description of free electrons. Accordingly, they are mostly employed for the study of solid crystalline materials. Equation 2.22 shows the electronic orbitals represented by this type of function:

$$\psi_j(\vec{r}_j) = e^{i\vec{j}.\vec{r}} \quad (2.22)$$

The main advantage of this function is that numerically, the matrix elements are easy to calculate. Thus, allowing using relatively large basis sets. However, this can also make more difficult the interpretation of the basis functions in terms of physical observables of the system.[34]

2.6.Self-Consistent Solution of HF Equations

After considering the different approximations presented in sections 2.3, 2.4, and 2.5, it is possible to introduce a self-consistent algorithm for solving equation 2.1.b, and

obtaining the electronic energy contribution ($E_{electrons}$) using the Hartree-Fock approach. As mentioned above, the solution to equation 2.1.b, Ψ (r), can be calculated with a determinant of the individual electronic orbitals (ψ_j). These individual orbitals can be obtained solving the one-electron Hartree-Fock equations (equation 2.17). However, in order to calculate the Coulomb and Exchange operators in the Hartree-Fock equations (equations 2.14 and 2.15), the individual electronic orbitals must be known. Thus, an iterative procedure is needed to break this cycle.

The first step is to define some *trial* electronic orbitals (ψ_j) as those in equation 2.18, using any of the basis functions described in the previous section, and defining some expansion coefficients $\alpha_{j,i}$. Then, the Coulomb and Exchange operators in the Hartree-Fock equations are calculated and used to solve equation 2.17. The calculated electronic orbitals are compared to those initially proposed. If they do not match, a new estimate of the expansion coefficients is made using the calculated E_i contributions, until they converge. Figure 2.2 schematizes the self-consistent Hartree Fock procedure.

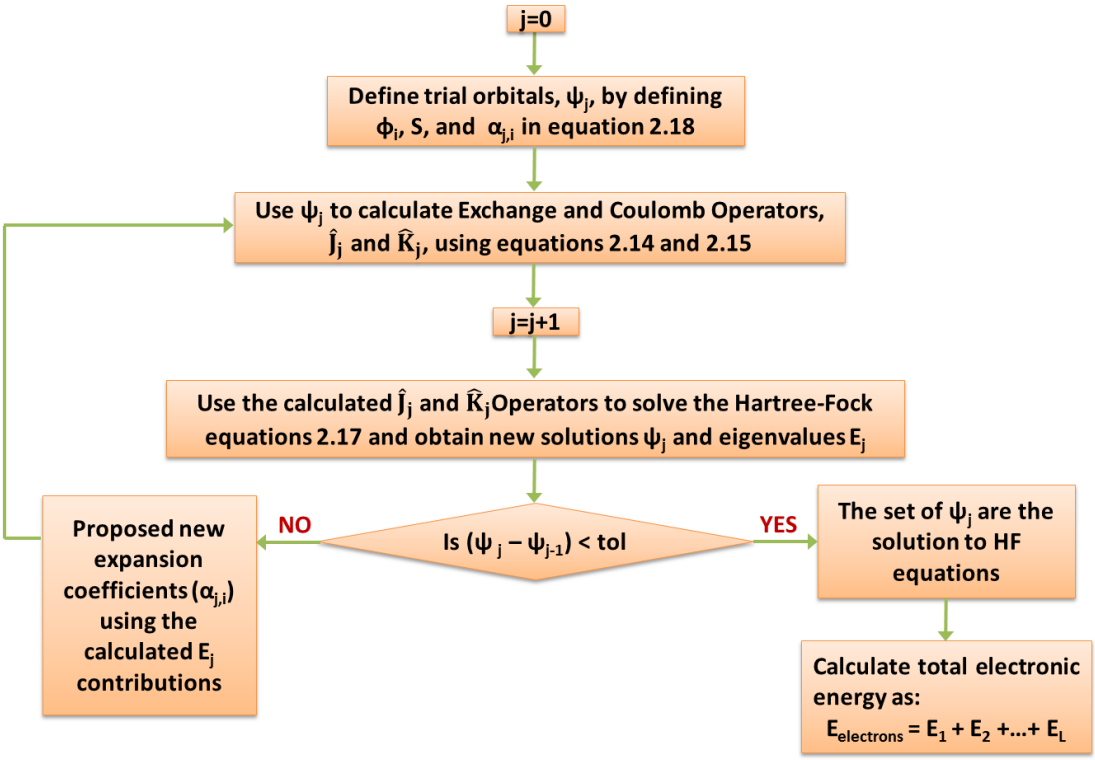

Figure 2.2 Self-consistent Hartree-Fock procedure

2.7.Correlation Effects

The Hartree-Fock method is based on the independent particle approximation mentioned in section 2.3. As such, electrons are assumed to behave independently, being only affected by an *average field* generated by other electrons. This approximation may lead to significant errors, especially when dealing with systems in which energy differences between occupied and unoccupied orbitals for the ground state configuration are small,[38] and when dealing with regions of concentrated electronic density in which electron movements are less independent of each other.[34]

The *correlated motion* of electrons can be taken into account explicitly by expanding the electronic wave-function into a linear combination of Slater determinants. In that way, some excited configurations are included in the search for the ground state of the system, providing more flexibility to the description of electron distribution. Among the most commonly used correlated methods are the configuration interaction method (CI), multiple configuration method (MC-SCF), Coupled-Cluster methods (CC), and Møller-Plesset perturbation theory.[38] The biggest downside of this approach is the demanding computational effort required.

2.8.Density Functional Theory (DFT)

DFT methods work by solving an equation that finds directly the electronic density of the system, ρ (r), which is a function of only 3-spatial coordinates:

$$\rho(r) = 2\sum\psi_i^*(r)\psi_i(r) \tag{2.23}$$

In this way, finding the electronic state of the system is simpler than dealing with the 3-L dimensional electronic wave-function, Ψ (r). DFT methods scales more favorably with system size than Hartree-Fock based methods, and can be applied to relatively large systems with energy accuracies between 10-40 kJ/mol.[39] The theory is based on the Hohenberg-Kohn theorems, formulated in the 1960s. The first theorem states that the ground state energy from the Schrödinger equation is a functional of the electronic density: E [ρ (r)], and any ground-state property can be uniquely defined from it.[40] Even though this theorem guarantees the existence of the energy functional, it does not say anything about its shape.

The second Hohenberg-Kohn theorem proves a variational principle for the energy functional, E [ρ (r)].This is, once the functional is known, the ground state density can be found by inserting approximate electronic densities until the calculated energy is a minimum. Although the Hohenberg-Kohn theorems prove important points required for

any calculation scheme, they do not directly provide the practical steps for finding the electronic density using the energy functional. These steps were provided by Kohn and Sham, as it will be presented in the next section.

2.8.1. The Kohn-Sham Method (KS)

The *unknown* energy functional is expected to contain a kinetic energy term (T), an external potential term coming from the nuclei (V_{ext}), a third term due to classical columbic interactions between electrons, and a final term due to exchange and correlation contributions (E_{XC}):

$$E = T[\rho(r)] + \int V_{ext}(\vec{r})\rho(\vec{r})d\vec{r} + \iint \frac{\rho(\vec{r}_1)\rho(\vec{r}_2)}{|\vec{r}_1-\vec{r}_2|}d\vec{r}_1\, d\vec{r}_2 + E_{XC} \quad (2.24)$$

Kohn and Sham proposed a fictitious system of non-interacting particles, moving under some external potential (V_{eff}), and having the same electronic density and energy as the real system. Since the particles are not interacting with each other, the classical columbic term describing interactions between electrons is not necessary. The resulting energy functional is shown below:

$$E = T_0[\rho(r)] + \int V_{eff}(\vec{r})\rho(\vec{r})d\vec{r} = \hat{h}_{eff} \quad (2.25)$$

The kinetic energy (T_0) is not the same as that of the real system (T) because of the different nature of the non-interacting particles. Also, the effective potential (V_{eff}) is defined below:

$$V_{eff} = V_{ext} + \iint \frac{\rho(\vec{r}_1)\rho(\vec{r}_2)}{|\vec{r}_1-\vec{r}_2|}d\vec{r}_1\, d\vec{r}_2 + \frac{\delta E'_{XC}}{\delta\rho} + \frac{\delta T}{\delta\rho} - \frac{\delta T_0}{\delta\rho} \quad (2.26)$$

The total Hamiltonian operator for this system can be written as a function of the single particle operators defined in equation 2.25:

$$\hat{H} = \sum_{i=1}^{L} \hat{h}_{eff}(i) \tag{2.27}$$

Analogous to the one-electron Hartree-Fock equations presented in section 2.4, single-electron Kohn-Sham equations (K-S) are developed to determine the single electron orbitals:

$$\hat{h}_{eff}\ \psi_i(r) = [T_0\,[\rho\,(r)] + \int V_{eff}(\vec{r})\rho(\vec{r})d\vec{r}]\ \ \psi_i(r) = E_i\,\psi_i(r) \tag{2.28}$$

The problem in trying to solve equation 2.28 lies in the unknown nature of the terms $\frac{\delta E'_{XC}}{\delta\rho} + \frac{\delta T}{\delta\rho} - \frac{\delta T_0}{\delta\rho}$ defining V_{eff}. Thus, approximate functionals have been proposed to calculate these terms, which are put together in a potential known as the exchange-correlation potential (V_{XC}):

$$V_{XC} = \frac{\delta E'_{XC}}{\delta\rho} + \frac{\delta T}{\delta\rho} - \frac{\delta T_0}{\delta\rho} + s_i = \frac{\delta E_{XC}}{\delta\rho} \tag{2.29}$$

The exchange-correlation potential also includes a self-interaction correction (s_i), because electrons described in the K-S equations are also part of the total electronic density, thus, the columbic term in V_{eff} includes interaction between the electron and itself.[39] Different approaches proposed to specify V_{XC} will be reviewed in the next section.

2.8.2. Approximated Functionals for the Exchange Correlation Potential

There is one case in which the *true* form of V_{XC} can be derived exactly: the uniform electron gas.[39] In this case, the electronic density is constant in space and the exchange-correlation potential (V_{XC}) can be calculated for different constant electronic-densities. In real systems, however, the electronic density is different at every point in space. By applying the *Local Density Approximation (LDA)*, V_{XC} is obtained at every location

using the local density at that point and calculating the exchange-correlation potential for the uniform electron gas. This approach neglects the effect of the environment and focuses only in the local electronic density. Another approach known as *Generalized Gradient Approximation (GGA)* uses information about the local electronic density and the local gradient of the electron density. Popular GGA functionals include BP86,[41,42] BLYP,[43] PW91,[44] and PBE.[45]

Even though GGA functionals include more information about the electronic environment, it does not always produce more accurate results than LDA approaches. In general, LDA provides accurate descriptions of molecular structures, vibrational and elastic properties, and charge densities of a wide range of systems. But, it fails to describe heats of reactions and energy barriers. On the other hand, GGA calculates heats of reaction within 25 kJ/mol of experimental values, but fail at describing dispersion interactions (van der Waals). [46]

2.8.3. The Frozen Core and the Pseudopotential Approximation

The heavier the atoms in the system being studied become, the more accurate are the basis functions required to correctly describe their electronic behavior (Slater-type, Gaussian-type, plane-waves, etc.). In addition, near the nucleus electronic wave-functions display nodal, oscillating behavior.[34] Trying to reproduce these features would result in prohibitively expensive calculations. However, it is possible to take advantages of some phenomena related to the chemical activity of electrons. For example, tightly-bound core electrons are hardly affected by the atomic environment, and most physical properties are determined by valence electrons. Therefore, the *frozen-core approximation* is introduced. In this approach, electronic wave-functions of core-electrons electrons are pre-calculated and used to describe the inner electrons of atoms in the system. These wave-functions are kept *frozen* during the calculation and only the wave-functions of valence electrons are varied.[34,39]

Pseudopotentials are introduced as a way of getting rid of the nodal, oscillating features of the electronic wave-functions near the nucleus. They replace the true atomic wave-function with a smoother function that reproduces the ionic potential arising from nuclear charges and the frozen-core electron charges. Additionally, the pseudopotentials agree with the true wave-function in the region of the valence electrons.[34,39] Both of the approximations presented in this section reduce significantly the computational cost required for solving the K-S equations.

2.8.4. Self-Consistent Solution of KS Equations

After considering the different approximations presented in sections 2.8.2 and 2.8.3, it is possible to introduce a self-consistent algorithm for solving equation 2.1.b, and obtaining the electronic energy contribution ($E_{electrons}$) using the Kohn-Sham approach. The first step is to define a trial electronic density, ρ (r), and solve the K-S equations (eq. 2.28) to determine the single electron orbitals, ψ_j. As before, the shape of the electronic orbitals (ψ_j) is defined using the basis functions described in section 2.5.

Subsequently, the calculated electronic orbitals are used to calculate an electronic density, using equation 2.23. This calculated density is compared to the one initially proposed. If they do not match, a new estimate is made using the calculated E_i contributions, until they converge. Figure 2.3 schematizes the self-consistent KS procedure.

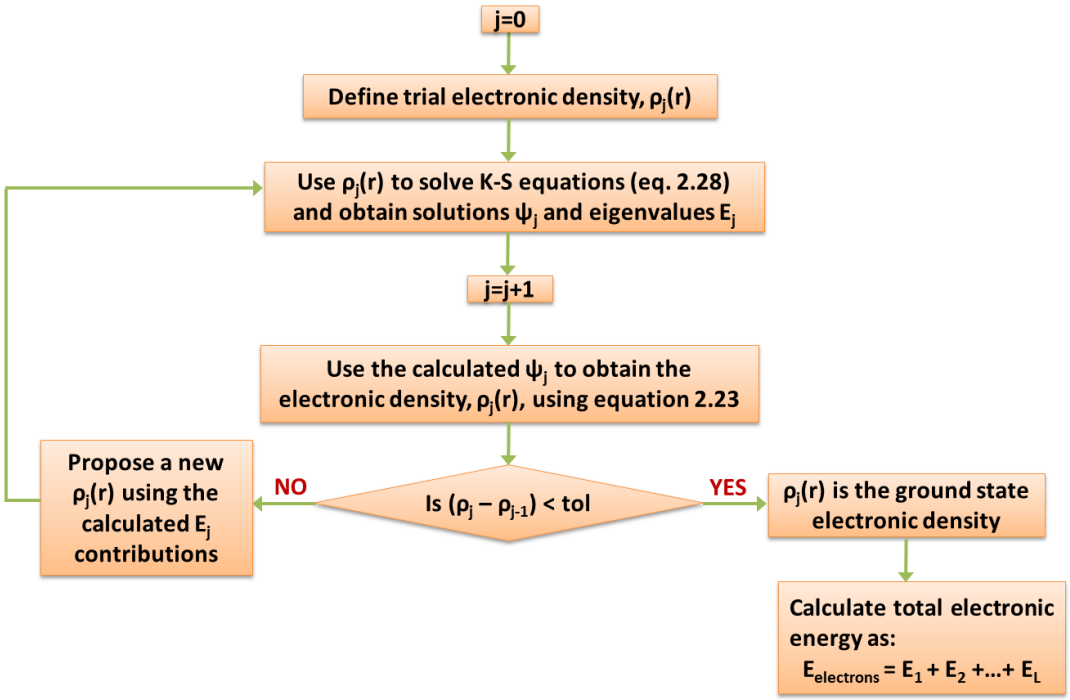

Figure 2.3 Self-consistent Kohn-Sham procedure

2.9.Hybrid Methods

As mentioned in section 2.7, including correlation effects in HF-based methods is a highly demanding computational task, especially when dealing with multi-reference systems. Alternatively, Including correlation effects in DFT-based methods is a simpler task that is accomplished with the help of LDA and GGA functionals presented in section 2.8.2, and yields relatively accurate results.[38] However, the solution of the exchange part of the functional in DFT-based methods is very approximate. Thus, it seems appropriate to combine the correlation functional from DFT with the exact exchange part from the HF formalism. This methodology reduces some of the inaccuracies of the LDA and GGA functionals and at the same time maintains the computational efficiency of DFT-based methods.[46]

In some of the most popular of such hybrid functionals, the DFT-exchange part is mixed with a percentage (X) of HF-exchange.[38] Examples include B3LYP (BLYP with X = 20),[47,48] B3PW91 (PW91 with X = 20),[15] and PBE0 (PBE with X = 25).[49,50]

2.10. Ab-Initio Molecular Dynamics Simulations (AIMD)

AIMD refers to a general approach in which the forces acting on the nuclei are calculated using classical mechanics, and electronic structure calculations are performed using quantum mechanics. For each set of nuclei coordinates, electronic structure calculations as those showed in Figure 2.2 and Figure 2.3 are performed, generating a simulation trajectory. This approach has some advantages compared to pure quantum mechanics optimization, including the incorporation of the time variable into the simulation, and the ability to handle larger systems (up to a few hundred atoms). Compared to classical MD simulations, AIMD provides much more accuracy because the chemistry of the system is accounted for using quantum mechanics rather than empirical parameterized potentials. Additionally, AIMD methods based on the Kohn-Sham formalism agree well with experimental results, and are usually more efficient than those based on Hartree-Fock, making it the most popular scheme for AIMD simulations.[39]

2.10.1. Equations Describing the Dynamics of Atoms

When describing the dynamics of a set of atoms (N) in a given volume (V), it is useful to define a few terms such as the total kinetic and potential energy of the system (K and U, respectively), using the 3N spatial coordinates of the atoms (r_1, r_2,…,r_{3N}), their 3N velocities (v_1, v_2,…,v_{3N}), and their mass (m_1, m_2,…,m_{3N}):

$$K = \frac{1}{2}\sum_{i=1}^{3N} m_i v_i^2 \tag{2.30}$$

$$U = U(r_1, r_2,\ldots,r_{3N}) = E_{total} \tag{2.31}$$

As mentioned above, the potential energy of the system (U) is calculated using quantum-based methods (E_{total}), commonly the K-S approach shown in Figure 2.3. Subsequently, this potential energy generates a force that drives nuclei movement:

$$F_{n,\,i} = -\frac{dU}{dr_i} \tag{2.32}$$

This force is related to the dynamics of the atoms through Newton's equation:

$$F_{n,\,i} = m_i.a_i = m_i\frac{dv_i}{dt} \tag{2.33}$$

This leads to the equation below, relating the calculated potential energy with atomic coordinates and velocities:

$$\frac{d^2r}{dt^2} = \frac{dv_i}{dt} = -\frac{1}{m_i}\frac{dU}{dr_i} \tag{2.34}$$

Typically, equations 2.32-2.34 are solved numerically. One of the most common approaches is the so-called *Verlet algorithm*, which uses a truncated Taylor expansion to define the trajectory of the particles in the system:[37]

$$r_i\,(t + \Delta t) \approx 2r_i\,(t) - r_i\,(t - \Delta t) + \frac{F_i(t)}{m_i}\Delta t^2 \tag{2.35}$$

The accuracy of equation 2.35 depends on the use of a very small time step (Δt), usually no larger than 10 femtoseconds.[37] A slightly different approach for describing the dynamics of atoms involves defining a *Lagrangian (L)* term using the kinetic and potential energies:

$$L = K - U = \frac{1}{2}\sum_{i=1}^{3N} m_i v_i^2 - E_{total} \quad (2.36)$$

In this case, the equation of motion will be given by:

$$\frac{d}{dt}\left(\frac{\partial L}{\partial v_i}\right) = \frac{\partial L}{\partial r_i} \quad (2.37)$$

2.10.2. Statistical Ensembles

Ensemble is a statistical term denoting the probability distribution of microstates of a system reproducing a set of macroscopic quantities (For example Number of particles (N), Volume (V), Temperature (T), Pressure (P), or Energy (E)). In order to calculate the properties of the system, expectation values of such properties are calculated as ensemble averages over a large number of microstates. In cases in which the total energy of the system (K + U) is conserved, the system evolves in a *microcanonical ensemble*, i.e., all different microstates reproduce constant values of N, V, and E. This ensemble reproduces a situation in which a system is thermically isolated.

Another interesting ensemble is the *canonical ensemble*, in which the system is allowed to exchange heat with its surroundings. Therefore, the energy is not conserved but N, V, and T. The temperature is defined using the Maxwell-Boltzmann distribution of velocities (v_i):

$$T = \frac{2}{6Nk_B}\sum_{i=1}^{3N} m_i v_i^2 \quad (2.38)$$

Usually the temperature is controlled by using the Lagrangian and adding an extra term including a fictitious thermostat. Equations of motion derived from such Lagrangian include a *friction term* (ξ) that can increase or decreases the velocities in the system to maintain T on target:

$$\frac{d^2r}{dt^2} = \frac{dv_i}{dt} = -\frac{1}{m_i}\frac{dU}{dr_i} - \frac{\xi}{m_i} v_i \quad (2.39)$$

In summary, AIMD is a sequential approach in which electronic structure calculations are performed using quantum mechanics, typically the Kohn-Sham formalism in Figure 2.3, for a set of fixed nuclear coordinates. This energy is then used as the potential energy (U) of the system and is employed to solve classical equations of motion that describe the dynamics of the nuclei. These may be either equations 2.34 or 2.39, depending on the canonical ensemble being used (microcanonical or canonical, respectively). After nuclei are moved using the equations of motion, another electronic structure calculation is performed, which generates a new potential energy affecting the nuclei. This process is repeated as long as necessary to generate a sufficiently large simulation trajectory (usually up to a few tens/hundreds picoseconds).

3. GEOMETRIC AND ELECTRONIC CONFINEMENT EFFECTS ON CATALYSIS [*]

3.1.Summary

We report a density functional theory-based study of the electronic and geometric effects exerted on molecules confined between transition metal surfaces. We first investigate changes in adsorption energies and activation barriers for dissociation of O_2 and NO_2 on Pt(111) and Fe(111) respectively. It is found that the energy barrier for dissociation of an O_2 molecule adsorbed on bridge site is 35 % lower than that on a single surface when the molecule is confined between two Pt (111) surfaces, and the barrier becomes negligible when the molecule adsorbs with its axis forming and angle of 60^o or 90^o with the plane of the surfaces. In the case of NO_2 confined between Fe (111) surfaces, the decrease is from 5-12% in the first deoxygenation and 10-15% in the second deoxygenation reaction. For both confined molecules, there is a substantial charge transfer from the metal surfaces that induces bond weakening thus facilitating dissociation. It is also found that the dissociation of CO, NO and O_2 on various confined transition metal surfaces follows the well-known linear Brønsted-Evans-Polanyi relationships between adsorption and activation energies, yielding smaller slopes than the same reactions on single surfaces, thus evidencing facilitation of the catalytic reaction. These findings suggest that the reported phenomena could be useful for the design of nanoporous catalytic structures as well as sensors and nanoelectronic devices.

---

[*] Reprinted with permission from Julibeth M. Martinez de la Hoz and Perla B. Balbuena. "Geometric and Electronic Confinement Effects on Catalysis". The Journal of Physical Chemistry C 2011 115 (43), 21324-21333. Copyright (2011) American Chemical Society

3.2.Introduction

Heterogeneous catalysis is an important field, crucial to most of the large scale industrial chemical processes [51]. When a solid surface is acting as a catalyst a sequence of elementary steps occur to accomplish the desired chemical reaction: reactants from a fluid phase are adsorbed onto the surface, adsorbed species react on the surface and finally, the products are desorbed back into the fluid phase. Thus, the adsorption energies of reactants, intermediates and products along with the activation energies separating the different intermediate steps, provide an adequate description of the given catalytic reaction. In general, the activation energy defines the rate at which the reaction occurs and the adsorption energies of the different species determine their rate of removal from the surface. A good catalyst is expected to display a good compromise between these two events.

A new interesting phenomenon that could help improve the catalytic activity of heterogeneous catalysts, is the confinement effect given by the proximity of two metal surfaces. Recent findings indicate that this confined environment is related to changes in the chemical, electronic, and magnetic properties of the material.[27,31,52,53] Structural changes in the metal as a function of the surface – surface separation, in the range of 3 – 10 Å, have been recently observed in metal alloy surfaces [52-31]. Regarding catalytic enhancements, Mahmoud and El-Sayed reported that the reduction of 4-nitrophenol by sodium borohydride catalyzed inside the cavity of cubic hollow nanoparticles displayed a higher catalytic activity than on solid or partially hollow nanoparticles[54]. Similarly, an ethylene molecule confined between two metallic surfaces may experience significant chemical changes becoming a radical anion able to initiate a polymerization reaction[27]. Interestingly, the initiation of polymerization reactions due to confinement that was first shown through theoretical calculations[27] has been recently demonstrated experimentally using an STM tip. [55,56] Indeed, the electronic distribution in confined molecules is modified by the strong enhanced interaction of the metal surfaces, which determines a distinctive characteristic observed in confined systems: the presence of electrons in the

gap between the surfaces [31,53]. The highly populated electronic region results in variations of the electronic properties that are reflected in changes in the density of states (DOS) of a given metallic system, as a function of metal – metal separation. Broader d-bands, lower DOS at the Fermi level and decrease in the exchange splitting have been observed in a system of a Ti monolayer over Pt, when interacting with another Pt surface at distances smaller than 6 Å. In this case, the electronic modifications are also closely related to variations of the magnetic properties of the given metallic system [53]. All these alterations are expected to affect the geometrical structure and reactivity of species confined between the two metal overlayers. For example, variations in electron confinement in ultra-thin metal films have been found to modify the O_2 dissociative adsorption on Mg films. [57] These examples suggest that understanding how confinement influences the adsorption and dissociation of adsorbates should be vital not only for the design of new improved catalysts but also may find novel applications in sensors and nanoelectronics.

In the first part of this work, we use density functional theory (DFT) methods with the aim of elucidating whether or not a given reaction is facilitated by spatial confinement of the adsorbate among metal surfaces focusing on the changes observed at the electronic level of the molecules and the metallic system. DFT has been shown to have the ability to make reliable semi-quantitative predictions of catalytic phenomena, including adsorption and activation energies for dissociation of molecules over a range of metal surfaces [58,59]. The first case studied in this section, is the well known O_2 dissociation on Pt (111). There are two molecular chemisorbed precursor states: the paramagnetic superoxo O_2^-, centered at bridge sites, and the non-magnetic peroxo O_2^{2-} centered over fcc sites [60]. According to the adsorption energies calculated by Eichler and Hafner using ab-initio calculations on the O_2/Pt(111) system, the superoxo state should be the most stable chemisorption state [61]. Thus, the variation of the energies due to adsorption and consequent dissociation of the superoxo precursor on Pt (111) is calculated as a function of the separation between Pt (111) surfaces. This analysis is very important because of

the significant role of platinum as a catalyst in many processes such as fuel cell technologies. Another important industrial process is the exhaust gas cleaning in automobiles through catalytic conversion. The adsorption and dissociation of NO_X, especially NO_2 on metal surfaces has been widely studied using theoretical and experimental procedures[62-71]. Thus, the second case studied in this part, is the dissociation of NO_2 on Fe (111) as a function of the separation between two Fe (111) exposed surfaces.

In the second part of this work, the confinement effect on specific reactions is intended to be further quantified. Calculations performed using DFT methods have allowed the establishment of relationships between adsorption and transition state energies, known as Brønsted-Evans-Polanyi (BEP) relations [72,73]. Linear correspondences between activation and reaction free energies were proposed first by Brønsted back in 1928 [72] and then by Evans and Polanyi in 1938 [73]. Currently, there are several such relationships providing a way to estimate activation energies using the adsorption energies of the intermediates [74-78]. A remarkable fact is that for a given metal surface structure, the transition state energy of similar molecules scales with the reaction energy in an analogous way, giving place to universal BEP relations. One of these relations is the one found by Nørskov et al for the diatomic molecules CO, N_2, NO and O_2 over transition metal surfaces [74]. These molecules present a transition state geometry close to that of the final state, for this reason they are known as "late transition" molecules. Changes in the adsorption energy of the final state are directly related to variations in the transition state energy, which is reflected through a linear correspondence with a slope close to one. Nørskov et al found that the line describing the dissociation of the molecules on stepped surfaces is positively shifted respect to that of the dissociation on close-packed planes [74]. Thus, when comparing the dissociation process on these two surfaces, a molecule that binds to them with the same strength would need a smaller activation energy to dissociate in the stepped surface. This means, stepped surfaces are more active catalyst

for the reactions studied, providing a better compromise between the energy needed for the dissociation and the rate of product removal.

Given that BEP relations provide valuable information related to the catalytic activity of metal surfaces toward specific reactions, in the second part of this work we study the dissociation of the diatomic molecules CO, NO and O_2 over the close packed plane of different transition metal surfaces for both a normal surface slab and the "confined" system, defined by the proximity of the two metal slabs separated about 4.9 Å. These universal relations are independent of the reactant and of the metal, varying only with the structure of the active site [76,77,79]; the comparison of the two BEP relations then allow determining and quantifying the influence of the confinement on the facilitation of the given reactions.

Lastly, we describe some catalysis scenarios where the suggested confinement effects can be realized. Electrochemical and surface science experiments[80-83] and continuum[84] and Kinetic Monte Carlo[85] simulations suggest that a porous structure might be present after the dealloying process. Experimental studies by Dimitrov et al[86] have concluded that dealloying of a less-noble component is sometimes accompanied by surface oxide formation involving the less-noble element, increasing the retention of such element in the porous matrix and modifying the catalytic activity. However, the structural models inferred from the experiments lack specific information and are only qualitative. On the other hand, a recent assessment of the catalytic activity of bimetallic and trimetallic alloys of composition PtM_3 and $PtNi_3M$ (with M = Co, Cu, Cr) [81] has clearly shown an enhanced ORR electrocatalytic activity claimed to be one of the highest currently achieved. But the actual reasons of the activity benefit which are attributed to the "nanoscale structure" of the dealloyed particles are not yet explained. The examples shown in this work suggest that such activity enhancement may be originated by the geometric and electronic confinement resulting from the nanoporous structure originated after the dealloying process.

3.3.Computational and System Details

Calculations were performed using the Vienna ab initio simulation package, VASP [87-91], with the exchange–correlation functional Perdew–Burke–Ernzerhof (GGA-PBE)[45] in the first part of the paper, where the systems are studied mostly at an electronic level. The revised PBE functional (GGA-rPBE) is employed in the second part of this work, where the BEP relationships are calculated, since this functional has been shown to improve the chemisorption energetic of atoms and molecules on transition-metal surfaces [92]. The projector augmented wave (PAW) pseudopotentials [93,94] provided in the VASP databases were used to describe the electron-ion interactions. The plane wave was expanded up to a cutoff energy of 400 eV. The convergence criteria for ionic relaxation loop and for electronic self-consistent iteration were set to 10^{-3} and 10^{-4} eV respectively, and a Methfessel–Paxton smearing of 0.2 eV was employed. A 4x4x1 k-points Monkhorst–Pack [95] mesh sampling in the surface Brillouin zone was applied for the DFT calculations. Whereas, for the electronic density of states calculations a 16x16x1 k-points mesh sampling was used. Spin polarization was included in every simulation. The calculations of the activation energies for dissociation of the adsorbates on the metal surfaces were performed using the nudged elastic band (NEB) method.[96-98] The method works by optimizing a number of intermediate images along the reaction path, while the initial and the final images corresponding to the reactant and product respectively are optimized previous to the NEB calculation. In all cases, four intermediate images were employed maintaining equal spacing between neighboring images. The Bader charge analysis was used to calculate the total electronic charge of an atom [99,100]. Within this method, the total electronic charge of an atom is approximated by the charge enclosed within the Bader volume defined by zero flux surfaces.

3.3.1. O_2 Dissociation on Pt (111) and NO_2 Dissociation on Fe (111) Surfaces

In the case of the O_2/Pt(111) system, the metal slab consisted of 6 layers modeled using 2 x 2 supercells (Figure 3.1). The close-packed plane (111) of the platinum face centered cubic (fcc) structure was used. The two top and the two bottom layers were allowed to

relax, whereas the two layers in the middle were kept fixed, representing the ‘‘bulk’’ material. Periodic boundary conditions were applied in x, y, and z directions for all the systems studied. Thus, the metal slabs are considered infinite in the x and y directions but the top (111) surface is separated from the image of the bottom (111) surface in the z direction by a distance H. Two different values of H were chosen: 15 Å to evaluate the properties of the O_2 molecule on the Pt (111) “surface”, where there is no interaction between the metal slab and its periodic image; and 4.7 Å to evaluate the properties of the O_2 molecule confined between two Pt (111) surfaces. The optimum bulk lattice constant of Pt was determined as 3.98 Å, which compares well with the experimental value of 3.92 Å. [101]

The simulations were carried out by locating the O_2 molecule parallel to the surface and centered on bridge sites in order to calculate the adsorption energy of the precursor superoxo chemisorbed state. In each simulation, the initial O–O distance was the gas phase value of 1.23 Å, as obtained from DFT calculations. Once the adsorption energies were calculated for both systems (H= 4.7 and 15 Å), the activation energies for O_2 dissociation were then obtained using the NEB method. In the final state, the oxygen atoms are located in threefold fcc hollow sites, which were determined as the most favorable location for the dissociated oxygen atoms on Pt (111) [61]. Adsorption energies (E_{ads}) are defined as the variation in energy due to taking the adsorbed O_2 molecule to the gas phase, and calculated using equation 3.1. $E_{2O/surf}$ stands for the total energy of the interacting surface and the adsorbed O_2 molecule, E_{Surf} stands for the total energy of the clean Pt (111) surface and E_{O2} represents the total energy of the molecular oxygen in gas phase.

$$E_{ads} = E_{2O/surf} - E_{surf} - E_{O2} \quad (3.1)$$

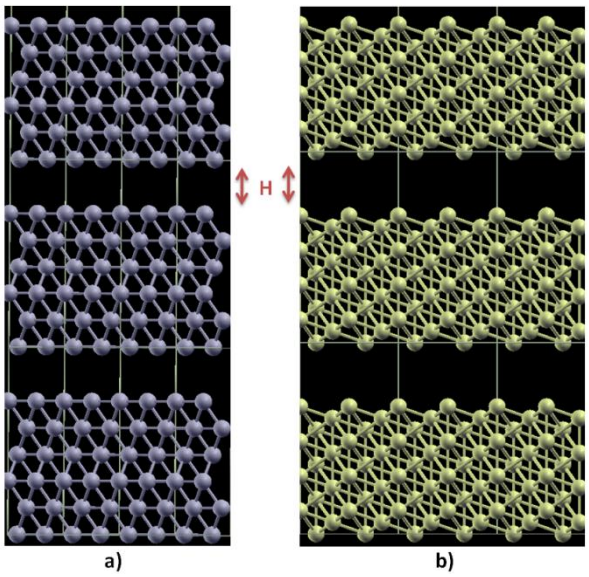

Figure 3.1 a) Pt slab, consisting of 6 layers modeled using 2x2 super cells and the close-packed plane (111) of the platinum face centered cubic structure b) Fe slab, consisting of 12 layers modeled using 2x2 super cells and the close-packed plane (111) of the iron body centered cubic structure. H represents in both cases the surface-surface separation in the z-direction

In the case of the NO_2/Fe (111) system, the metal slab consisted of 12 layers modeled using 2 x 2 supercells (Figure 3.1.b). The close-packed plane (111) of the iron body centered cubic (bcc) structure was used. The four top and the four bottom layers were allowed to relax, whereas the four layers in the middle were kept fixed, representing the ‘‘bulk’’ material. Periodic boundary conditions were applied in x, y and z directions for all the systems studied as in the previous case. Three different values of H were used in this case: 15 Å to evaluate the properties of the NO_2 molecule on the Fe (111) “surface”, whereas 5 and 4.5 Å were used to evaluate the properties of the NO_2 molecule confined between the two Fe (111) surfaces. The optimum bulk lattice constant of Fe was determined as 2.82 Å, which compares well with the experimental value of 2.87 Å. [101] Simulations were carried out by adding the NO_2 molecule in a threefold hollow site, which have been determined to be the most stable adsorption form for NO_2 on Fe(111)[71].

Adsorption energies were calculated for the three cases studied: H = 4.5, 5 and 15 Å. The initial geometry for the NO_2 molecule was obtained from DFT calculations in the gas phase. From these calculations the N-O bond length is 1.21 Å and the O-N-O angle is 133.8°. Once the adsorption energies were calculated, the activation energies for the first and second deoxygenation of the NO_2 molecule were then obtained using the NEB method and the reaction path proposed by Chen et al [71]. Adsorption energies (E_{ads}) in this case are defined as the variation in energy due to taking the adsorbed NO_2 molecule to the gas phase, calculated using equation 3.2. Here $E_{2O/surf}$ stands for the total energy of the interacting surface and the adsorbed NO_2 molecule, E_{Surf} stands for the total energy of the clean Fe (111) surface and E_{NO2} represents the total energy of the NO_2 molecule in gas phase.

$$E_{ads} = E_{2O,N/surf} - E_{surf} - E_{NO2} \quad (3.2)$$

3.3.2. BEP Relationships for O_2, CO and NO Dissociation on Transition Metals

The dissociation reactions of O_2, CO and NO were studied over Pt, Ir, Rh, Ni and Pd. The metal slab used in all the cases, is the same as the one described in section 3.3.1 for the O_2/Pt (111) system (Figure 3.1.a). Two different values of the separation distance H were used in this case: 15 Å to evaluate the adsorption and dissociation energies in the single surface and 4.9 Å to evaluate them in confinement. The optimum bulk lattice constants of Ir, Rh, Ni and Pd were determined as 3.88, 3.84, 3.52 and 3.95 Å, respectively, which compare well with the experimental values of 3.84, 3.92, 3.52 and 3.89 Å. [101]

The simulations were carried out by locating the molecules in their most stable chemisorption state on the given metal surface [102-104] to calculate their initial adsorption energy. In the final state, the atoms are located in threefold fcc hollow sites, which were determined as the most favorable location for the dissociated atoms on these surfaces.[102-104] In each simulation, the initial O–O, C-O and N-O distances were the gas phase values

of 1.23, 1.14 and 1.17 Å, as obtained from DFT calculations. Once the adsorption energies were calculated for both systems (H= 4.9 and 15 Å), the activation energies for the dissociation were then obtained using the NEB method. Adsorption energies (E_{ads}) are defined in a similar way to that in section 3.3.1 and calculated using equation 3.3. $E_{XX/surf}$ stands for the total energy of the interacting surface and the adsorbed molecule, E_{Surf} stands for the total energy of the clean (111) surface and E_{XX} represents the total energy of the molecule in gas phase.

$$E_{ads} = E_{XX/surf} - E_{surf} - E_{XX} \quad (3.3)$$

Since O_2, CO and NO display a "late transition" state, the universal BEP relationships are obtained by plotting the adsorption energies of the molecules in their final state vs. the activation energies for dissociation (E_{diss}). E_{diss} is obtained by subtracting the Adsorption energy of the molecule in the initial state from the transition state energy (E_{Tr}).

3.4.Results

3.4.1. O_2 Dissociation on Pt (111)

3.4.1.1.Adsorption of the O_2 Molecule

For H = 15 Å (surface), the O - O bond length and the adsorption energy of the optimized chemisorbed O_2 molecule are 1.35 Å and -0.62 eV, respectively. The bond length is in good agreement with previous values calculated for the O_2^- superoxo precursor using theoretical and experimental works.[61,105-109] However, the adsorption energy is slightly larger compared to the experimental values of -0.4 eV[105] and -0.5 eV[106], determined for the molecular precursors. This can be explained since chemisorption energies are found to be slightly overestimated within density functional theory, especially with the PBE functional [110]. As expected, charge transfer from the Pt surface to the molecule is observed. The charge of the adsorbed molecule is found to be

-0.43 electron units (e.u.), this is also in good agreement with the value -0.48 e.u. previously calculated[107] and in fair agreement with the charge -0.53 e.u. found in the superoxo state[109].

When evaluating the same properties for the chemisorbed O_2 molecule in the confined system (H = 4.7 Å), significant differences are found. The O – O bond length is longer and charge transfer to the adsorbed molecule is larger, with values of 1.4 Å and -0.6 e.u, respectively. These values may suggest in this case the molecular precursor correspond to the peroxo O_2^{2-} state, where reported values for bond length and charge are 1.43 Å and -0.64 e.u. respectively.[61,108,109]

The differences in charge transfer from the Pt surface to the adsorbate are also reflected on the electronic density of states (DOS) of the O_2 adsorbed molecule. As can be observed in Figure 3.2 and in agreement with previously calculated DOS for O_2 adsorbed on a Pt (111) surface [107,111] the discrete molecular orbitals of the O_2 molecule are broadened and shifted due to the interaction with the Pt substrate, resulting in a new set of electronic levels. Nevertheless, the energy splitting between bonding and antibonding states in the confined system (H = 4.7 Å) is significant smaller. This is related to a weaker O – O bond in which the bonding orbitals are being destabilized and the antibonding orbitals are stabilized. In addition, the larger population in the antibonding π^* orbital found in the confined system with respect to the surface, is in agreement with the larger transfer of charge to the former. This is reflected in the DOS diagram by a larger proportion of the π^* orbital lying below the Fermi level in the confined system. All of these suggest weaker bond strength in the O_2 molecule confined between the Pt (111) surfaces and explain the longer O – O bond length found in that case.

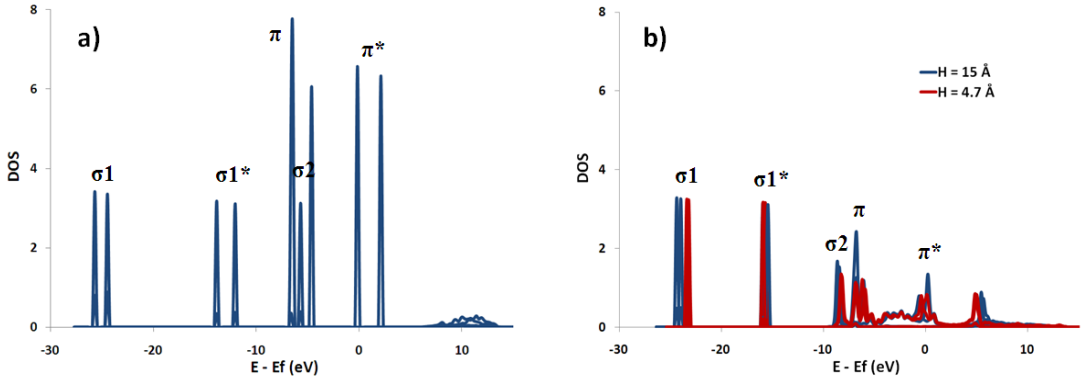

Figure 3.2 Electronic density of states of the O_2 molecule a) in gas phase b) Chemisorbed on the Pt (111) surface for two different values of the surface-surface separation H: 4.7 and 15 Å

The adsorption energy calculated for H = 4.7 Å is -0.53 eV, this is slightly weaker than the value calculated for H = 15 Å. The adsorption strength can be related to certain characteristics of the electronic structure. In this case, it is related to a shift of the p-band center of the molecule away from the Fermi level, which weakens the strength of the adsorbate–metal bond. The p-band center evolves from -6.7 eV to -8.2 eV for H=15 and 4.7 Å, respectively. The oxygen p-band center has been correlated to the adsorption energy on metallic surfaces before. [112] The shifting of the oxygen p-band center away from the Fermi level was found to coincide with weaker adsorption energies, in agreement with our results. The position of the Pt d-band center was also calculated, a value of -2.31 eV was found in both cases, which suggests that the difference in adsorption strength is only influenced by the shifting of the p-band center of the O_2 molecule.

3.4.1.2.Activation Energy for the Dissociation of O_2 on Pt (111)

Figure 3.3 shows the energy path for the dissociation of the chemisorbed O_2 molecule on the Pt (111) surface (H = 15 Å) and that in the confined system (H = 4.7 Å). The

activation energy for the dissociation in the surface is relatively high: 0.57 eV, in fairly good agreement with a previous theoretical calculation where it was found to be 0.63 eV[107]. On the other hand, a significantly smaller activation energy is needed when H = 4.7 Å. Following the same reaction path, the activation energy calculated for the dissociation of the confined molecule is 0.37 eV. This smaller barrier agrees with both the weaker O – O bond strength and the longer bond length observed in the chemisorbed state. Geometric details and images of the intermediate configurations are provided as Supplementary Information, as well as maps of the electronic density at the reactant, transition state, and product of the reaction for the two cases shown in Figure 3.3.

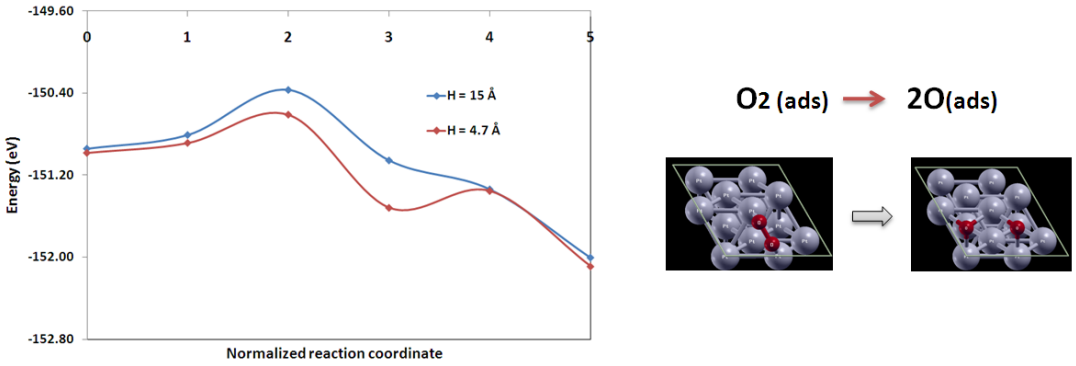

Figure 3.3 Left: Energy path for the dissociation of the chemisorbed O2 molecule on the Pt (111) surface, for separations H = 4.7 and 15 Å. Right: Reaction followed and configuration of the initial and final states

Thus, a facilitation of the O_2 dissociation when the molecule is confined between Pt (111) surfaces is observed as a result of a larger charge transfer from the substrate to the adsorbate. This is perhaps, not the only advantage that the confinement can provide when trying to dissociate molecular oxygen. It has been previously found that when the separation among the Pt (111) surfaces is smaller than 4.8 Å, spontaneous dissociation of

the O_2 molecule, placed initially in a vertical position between the surfaces, occurs.[113] This is explained as a consequence of the enhanced, stronger interaction of the top and bottom surfaces with the atoms in the molecule and is also reflected by the sharing of a high electronic density between them. Therefore, to quantify further advantages offered by the confinement, activation energies for the dissociation of both, an initially vertical O_2 and a slightly tilted O_2 molecule (approximately 60° with respect to the x-y plane), confined among the Pt (111) surfaces were calculated. The same value of H = 4.7 Å was used in both cases for comparison. The reaction paths for these cases are shown in Figure 3.4. For the initially vertical O_2 molecule, there is no activation barrier for the dissociation, in agreement with the spontaneous dissociation observed in reference [112]. In the case of the tilted molecule a really small energy is needed to activate the dissociation, corresponding to 0.03 eV. All the intermediate configurations as well as details on the geometry in Figure 3.4 are included as Supporting Information.

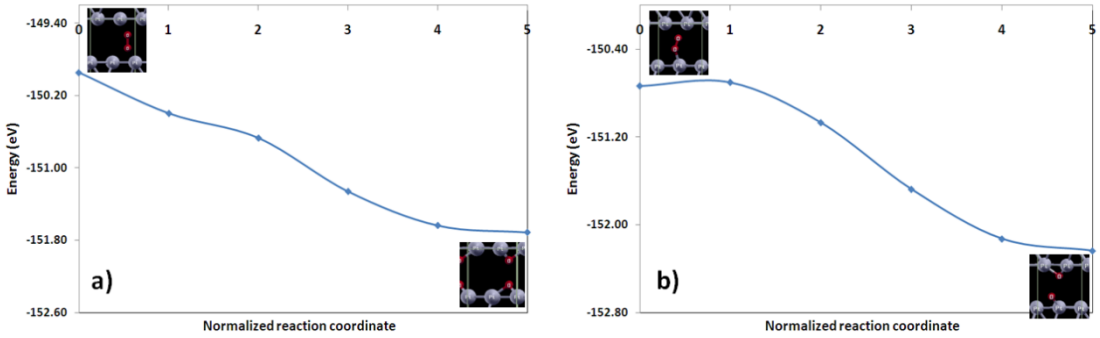

Figure 3.4 Energy path for the dissociation of an O2 molecule on the Pt (111) surface with H = 4.7 Å a) O2 molecule placed vertically among the surfaces b) O2 molecule slightly tilted, approximately 60o with respect to the surface plane

3.4.2. NO_2 Dissociation on Fe (111)

3.4.2.1.Adsorption of the NO_2 Molecule on the Fe (111) Surface

Table 3.1 displays adsorption energies and charges for the NO_2 molecule, as a function of the Fe (111) surface-surface separation (H). For H = 15 Å (single surface), the calculated adsorption energy of -3.07 eV is in reasonable agreement with the value of -2.8 eV, calculated for NO_2 adsorbed in the same configuration on the Fe (111) surface[71]. The trend observed in the data in Table 3.1, suggests slightly stronger bond strength between the molecule and the substrate and increases in the charge transfer to the NO_2 as the surface-surface separation H decreases. However, the difference among the adsorption energies and among charges is rather small, leading to very small differences in the DOS of the adsorbed NO_2 as a function of H (Figure 3.5). A relatively larger broadening of the bands is observed as H decreases.

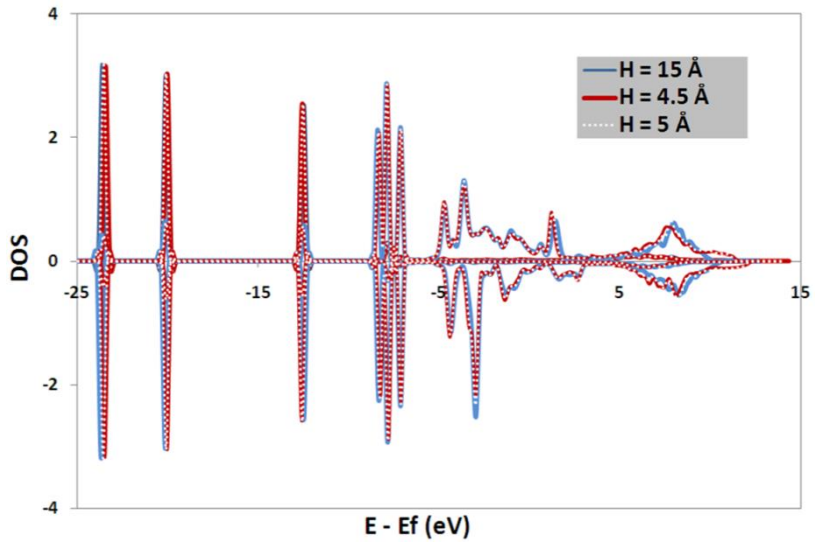

Figure 3.5 Electronic density of states of the NO_2 molecule adsorbed on the Fe (111) surface for the three different values of H: 4.5, 5 and 15 Å

The larger charge transfers from the surface to the molecule, however, seem to weaken the bonds in the molecule, as reflected by the slightly longer N – O bond lengths (Table 3.1). Electronic density maps provided as Supporting Information illustrate the differences in the adsorbed states for the single surface and two values of confinement. Differences among the d-band center of the Fe (111) substrate (-0.76 eV) and the p-band center of the adsorbed NO_2 molecule (-7.96 eV) were not found with variations in H.

Table 3.1 Adsorption energies, charges and N-O bond lengths corresponding to the NO_2 molecule adsorbed on the Fe (111) surface, as a function of H

Surface – Surface separation, H (Å)	**Adsorption energy (eV)**	**Charge of the NO_2 molecule (e. u.)**	**N – O bond length (Å)**
15	-3.07	-1.19	1.37
5	-3.29	-1.30	1.38
4.5	-3.39	-1.33	1.39

3.4.2.2.Activation Energy for the Dissociation of NO_2 on Fe (111)

Figure 3.6 shows the energy path for the first deoxygenation of the NO_2 molecule as proposed by Chen et al [71]. This reaction path is in good agreement with the experimental finding of the transition metal cleaving the N-O bond of the NO_2 and following the reaction mechanism called *electron-transfer-assisted oxygen abstraction*.[114] The energy barrier to activate the first deoxygenation of NO_2 on the surface (H = 15 Å) is 0.35 eV, in reasonable agreement with the barrier calculated by Chen et al (0.45 eV) [71]. Also, as expected from the weakened N-O bonds found with decreasing H, the barrier for deoxygenation is slightly smaller as H decreases (Table 3.2).

Table 3.2 Activation energies for the first and second deoxygenation of the NO_2 molecule on Fe (111), as a function of the surface-surface separation, H

Surface – Surface separation, H (Å)	Activation energy for the first deoxygenation (eV)	Activation energy for the second deoxygenation (eV)
15	0.35	0.77
5	0.33	0.70
4.5	0.31	0.66

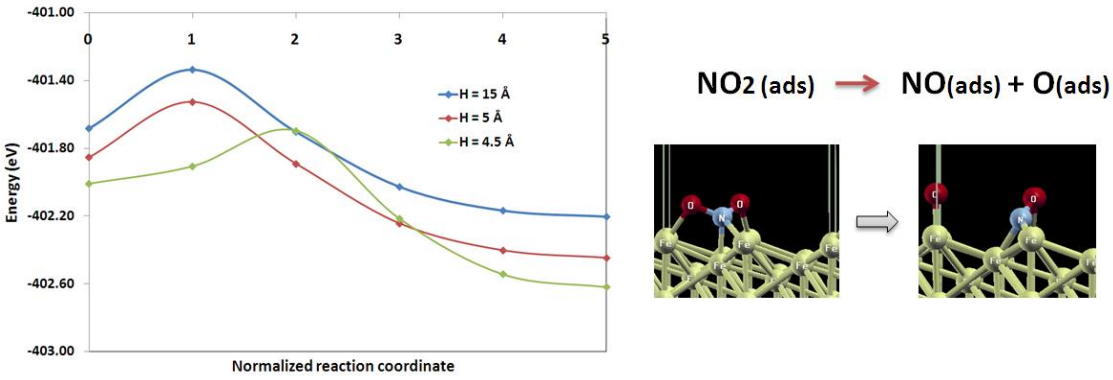

Figure 3.6 Left: Energy path for the first deoxygenation of the NO_2 molecule on the Fe (111) surface, for H = 4.5, 5 and 15 Å. Right: Reaction followed and configuration of the initial and final states

The energy path for the second deoxygenation of the NO_2 molecule is shown in Figure 3.7. In the initial state, there are a NO molecule and one oxygen atom adsorbed on the Fe (111) surface. Calculated adsorption energies, charges and N-O bond lengths are shown in Table 3.3. As in the previous case, slightly stronger bond strength between the

molecule and the substrate and increases in the charge transfer to the adsorbate are found when H decreases. In addition, the N-O bond strength is weakened, reflected in longer N-O bond lengths for smaller values of H. Thus, as in the previous deoxygenation, the barrier decreases slightly with decreasing H (Table 3.2). The energy barrier to activate the second deoxygenation of NO_2 on the surface (H = 15 Å) is 0.77 eV (Table 3.2), which is again in reasonable agreement with the barrier 0.84 eV [71]. Differences with the values calculated in reference [71] are mostly due to the difference in the choice of functional: the GGA(r-PBE) functional vs. the GGA (PBE) used in this work. Details of the geometries of the various intermediate states of Figure 3.6 and Figure 3.7 are provided as Supporting Information.

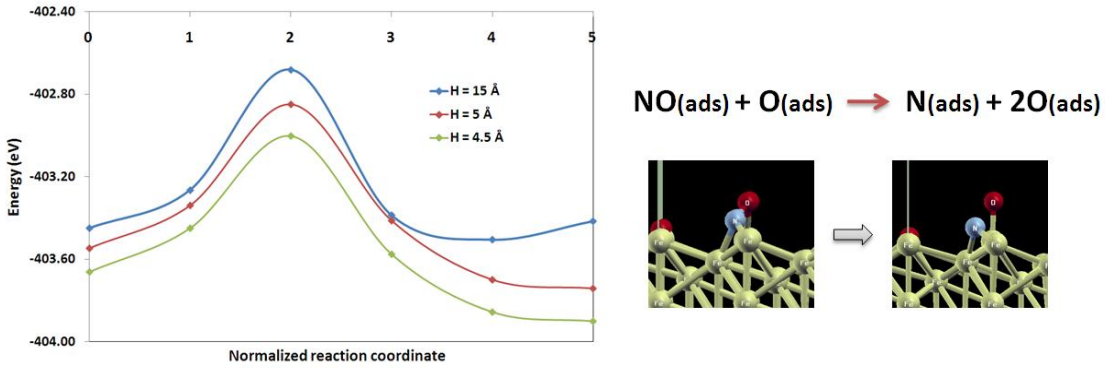

Figure 3.7 Left: Energy path for the second deoxygenation of the NO_2 molecule on the Fe (111) surface, for H = 4.5, 5 and 15 Å. Right: Reaction followed and configuration of the initial and final states

Table 3.3 Adsorption energies, charges and N-O bond lengths corresponding to the NO molecule adsorbed on the Fe (111) surface, as a function of H

Surface – Surface separation, H (Å)	**Adsorption energy (eV)**	**Charge of the NO molecule (e. u.)**	**N – O bond length (Å)**
15	**-4.83**	**-0.88**	**1.30**
5	-4.98	-0.92	1.31
4.5	-5.05	-0.95	1.31

The results obtained in sections 3.4.1 and 3.4.2 show that the spatial confinement of adsorbates between metallic surfaces influences their adsorption energies and energy barriers for dissociation. However, the degree of confinement-driven facilitation for a given reaction appears to depend on the nature of the surface and also on the specific reaction. Thus, with the aim of further exploring these influences in a systematic way, BEP relationships are calculated in section 3.4.3 for the dissociation reactions of O_2, CO and NO on different close packed transition metal surfaces.

3.4.3. BEP Relationships for O_2, CO and NO Dissociation on Transition Metals

Figure 3.8 shows the activation energies for the dissociation of CO, NO and O_2 on the close packed plane of different transition metals plotted as a function of the adsorption energy of the dissociated products ($E_{ads\text{-}F}$). For both the surfaces and the confined systems we found actual linear relationships like those in the Brønsted–Evans–Polanyi relations:

$$E_{diss} = A*(E_{ads\text{-}F}) + B$$

In the case of the surface slabs (Figure 3.8.a), A = 0.92 and B = 2.58; these results are in very good agreement with the values A = 0.90 ± .04 and B = 2.07 ± .07 found by

Nørskov et al for the dissociation of CO, N_2, NO and O_2 over the close packed plane of transition metal surfaces [74]. In the case of the confined systems (Figure 3.8.b), A = 0.81 and B = 2.22, the line is slightly shifted positively with respect to that of the surfaces (B decreases from 2.58 to 2.22). However, the most significant change between these two relationships is found in the decrease of the slope from 0.92 to 0.81. The smaller slope in confinement is the consequence of larger decreases on the activation energies for the molecules in the following order: CO > NO > O_2. On average the decrease in activation energies for the dissociation of the confined molecules with respect to that on the surface were 0.62, 0.34 and 0.09 eV for CO, NO and O_2 respectively. Table 3.4 displays the adsorption energies in the initial ($E_{ads\text{-}I}$) and final-dissociated state ($E_{ads\text{-}F}$), and the transition (E_{Tr}) and activation energies for the dissociation (E_{diss}) for every system studied, relative to the free molecules in gas phase. Also, the charges of the initially adsorbed molecules on both single surfaces and confined systems are provided.

The reason for the different degrees of confinement-driven facilitation seems to be related to the degree of interaction of the atoms in the molecule with the top metallic layer of the confined system and relatively independent of the transition metal. This can be better understood by observing Figure 3.9.a, where the shortest distance between the atoms in the molecule and the top metallic layer is plotted as a function of the variation in the activation energy with respect to the dissociation in the surface. A direct relation can be observed, implying larger facilitations of the given reaction for those molecules closer to the top metallic layer. The proximity of the molecule and the metallic layer allows a better electronic interaction between them, which would work by increasing the additional charge transferred to the molecule (Figure 3.9.b) and debilitating the molecular bond as was also found in section 3.4.1. As an example, Figure 3.10 shows the electronic density maps for the adsorbed CO, NO and O_2 on Pt (111), whose shortest distance to the top layer of this surface are 2.41, 2.51 and 3.03 Å, respectively. It is clear that the strongest interaction is found in the case CO/Pt, reflected in larger electronic densities shared between the molecule and the top metallic layer.

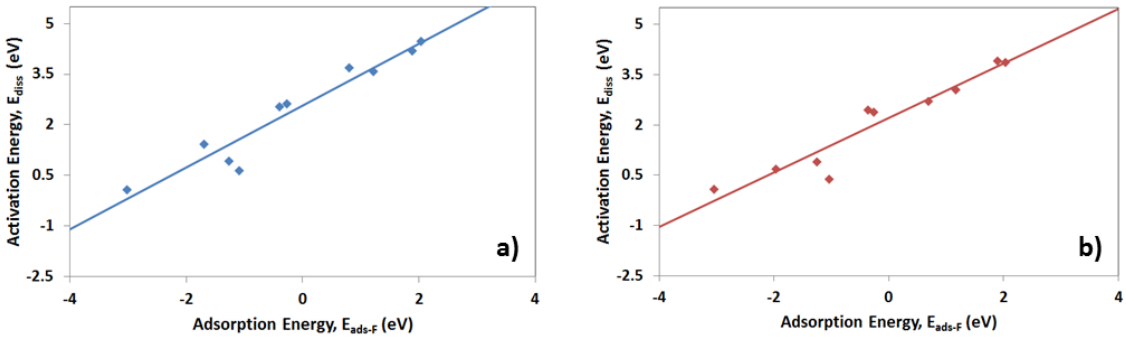

Figure 3.8 Calculated activation energies ($E_{\_diss}$) for CO, NO and O_2 dissociation on the close packed plane of different transition metals plotted as a function of the calculated adsorption energy of the dissociated products (E_{ads-F}). The data are shown in Table 3.4. a) Calculations performed on a single slab surface. b) Calculations performed on confined systems defined by the proximity of the two metal slabs separated about 4.9 Å

Table 3.4 Adsorption energies of the initially adsorbed (Eads-I) and dissociated molecules (E_{ads-F}), transition ($E_{\_Tr}$) and activation energies ($E_{\_diss}$) for the dissociation, and charges of the initially adsorbed molecule for every system studied

System	H = 15 Å					H = 4.9 Å				
	E_{ads-I} (eV)	E_{ads-F} (eV)	E_{Tr} (eV)	E_{diss} (eV)	Charge molecule (e.u.)	E_{ads-I} (eV)	E_{ads-F} (eV)	E_{Tr} (eV)	E_{diss} (eV)	Charge molecule (e.u.)
CO/Pt (111)	-1.43	1.88	2.76	4.19	-0.18	-1.13	1.89	2.79	3.92	-0.32
CO/Pd (111)	-1.59	2.04	2.87	4.46	-0.21	-1.40	2.03	2.45	3.86	-0.33
CO/Ni (111)	-1.54	1.22	2.05	3.59	-0.34	-1.44	1.17	1.60	3.04	-0.54

Table 3.4 continued

System	H = 15 Å					H = 4.9 Å				
	E_{ads-I} (eV)	**E_{ads-F} (eV)**	**E_{Tr} (eV)**	**E_{diss} (eV)**	**Charge molecule (e.u.)**	**E_{ads-I} (eV)**	**E_{ads-F} (eV)**	**E_{Tr} (eV)**	**E_{diss} (eV)**	**Charge molecule (e.u.)**
CO/Ir (111)	-1.83	0.80	1.85	3.69	-0.07	-0.54	0.69	1.84	2.70	-0.28
NO/Pt (111)	-1.46	-0.40	1.07	2.53	-0.36	-1.09	-0.36	1.36	2.46	-0.49
NO/Pd (111)	-1.83	-0.27	0.78	2.61	-0.34	-1.58	-0.26	0.81	2.38	-0.48
NO/Ni (111)	-2.06	-1.69	-0.65	1.41	-0.55	----	----	----	----	----
NO/Rh(111)	----	----	----	----	----	-1.90	-1.96	-1.21	0.69	-0.58
O_2/Pt (111)	-0.20	-1.09	0.44	0.64	-0.43	-0.05	-1.04	0.33	0.39	-0.54
O_2/Pd (111)	-0.42	-1.27	0.50	0.92	-0.54	-0.35	-1.25	0.56	0.91	-0.65
O_2/Ni (111)	-0.98	-3.01	-0.90	0.08	-0.78	-1.02	-3.05	-0.94	0.09	-0.91

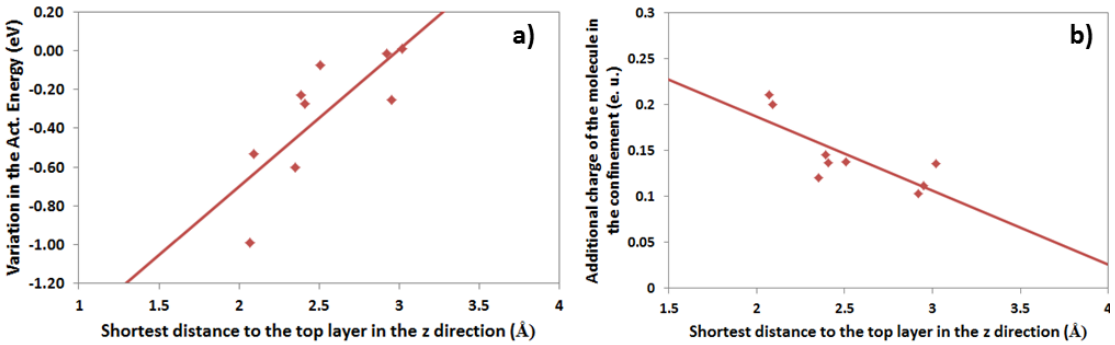

Figure 3.9 a) Variations on the activation energies for dissociation compared to that on normal surfaces, as a function of the shortest distance of the atoms in the molecule to the surface top layer. b) Additional charge of the molecule in the confinement (with respect to that on a surface) as a function of the shortest distance of the atoms in the molecule to the surface top layer. Data were obtained from Table 3.4 in cases when comparisons were possible

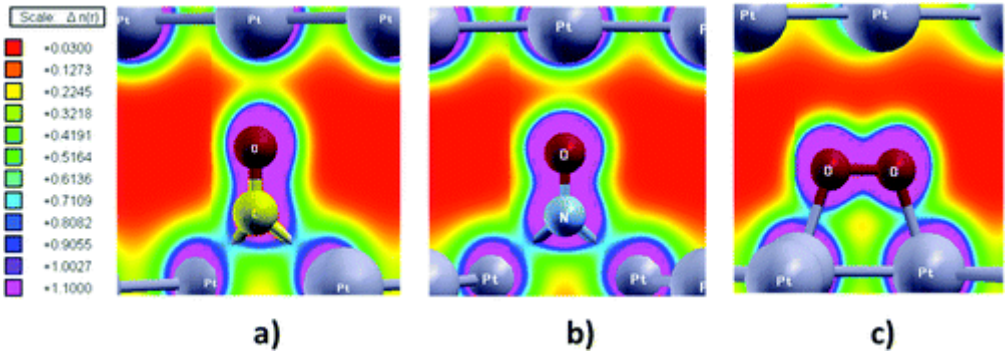

Figure 3.10 Electronic density maps for molecules adsorbed between two Pt (111) surfaces at a surface–surface separation distance H = 4.9 Å. (a) CO, (b) NO, and (c) O_2

3.5.Conclusions

Spatial confinement of adsorbates between metallic surfaces influences their adsorption energies and energy barriers for dissociation. Molecular oxygen chemisorbed among Pt (111) surfaces dissociates with a significantly smaller energy when the surface – surface separation is 4.7 Å (confinement), compared to that of a single surface. The difference

between these energies is related to a larger charge transfer from the substrate to the O_2 molecule in confinement, which generates larger changes in the electronic structure of the molecule and weakens the O – O bond strength. Changes in the p-band center of the molecule are also observed, with a shifting away from the Fermi level in the confined state, resulting in the weaker adsorption energy found for H = 4.7 Å. We also studied the influence of confinement on the adsorption and dissociation of NO_2 on Fe (111), obtaining similar qualitative results to the ones found for O_2./Pt (111). The charge transfer from the surface to the adsorbate increases as H decreases, which seems to weaken the N – O bonds in the molecule and facilitate the dissociation under confinement. However in the NO_2/Fe(111) system, quantitative differences between the charges transferred to the adsorbate as a function of H, and thus differences among energy barriers for dissociation are rather small. We conclude that the degree of confinement-driven facilitation for a given reaction depends strongly on the nature of the surface (close packed vs. stepped surfaces) and also on the specific reaction.

To further understand confinement effects on reactivity, BEP relationships were found for the dissociation of CO, NO and O_2 on the close packed plane of transition metals for both single surfaces and confined systems. The main difference found is the smaller slope in confined systems, which is reflected in different degrees of facilitation for the reactions studied. On average, the decrease in activation energies for the dissociation of CO, NO and O_2 with respect to those on the surface were 0.62, 0.34 and 0.09 eV, respectively. The confinement-driven facilitation is found to be related to the degree of interaction of the atoms in the molecule with the top metallic layer of the confined system and relatively independent of the transition metal. The proximity between the molecule and the metallic layer allows a better electronic interaction between them, which would work by increasing the additional charge transferred to the molecule and debilitating the molecular bond as shown in the first part of this work. To conclude, we emphasize the relevance of the present findings for the design of novel catalytic

nanoporous metal structures with enhanced activity. Similar phenomena can be useful in the design of nanosensors and nanoelectronic devices.

4. LOCAL SURFACE STRUCTURE EFFECT ON REACTIVITY OF MOLECULES CONFINED BETWEEN METALLIC SURFACES [*]

4.1.Summary

Interactions between metallic surfaces separated by nanometer distances create an unusual reactivity environment. Here we evaluate the effect of the geometry given by differences in the structures of the interacting surfaces and by the presence of steps. Adsorption of an oxygen molecule and its dissociation is examined in gaps defined by interacting platinum surfaces of separations between 5.36 and 4.70 Å, comparing the effect of the different gap geometries on the adsorption strength and barriers for dissociation. It is found that specific surface-surface configurations influence the electronic structure of the surface where the molecule is adsorbed, modifying the width of its d-orbital and therefore the adsorption strength due to changes in the overlap of the adsorbate molecular orbitals with the metal d-band. In addition, the degree of the molecule/metal interaction with the other surface may restrict the adsorbate mobility and its dissociation. The presence of defects may decrease the adsorbate/surface interaction strength, but the net result depends on the specific reaction and nature of the intermediates since in some cases weaker adsorptions may result in lower dissociation barriers.

---

[*] Reprinted with permission from Martinez de la Hoz, J. M.; Balbuena, P. B.: "Local surface structure effect on reactivity of molecules confined between metallic surfaces". Phys. Chem. Chem. Phys. **2013,** 15, 1647-1654- Reproduced by permission of the PCCP Owner Societies. Copyright (2013) PCCP Owner Societies

4.2.Introduction

Solid surfaces are employed as heterogeneous catalysts for a large number of chemical reactions. The catalytic effectiveness of such surfaces is given by their ability to adsorb, dissociate, and desorb chemical species. Some reactions require strong adsorption of a given species, while others require weak adsorption strengths. Similarly, when a reaction involves cleavage of molecular bonds, small activation barriers for the dissociation allow higher reaction rates, whereas in other cases, the dissociation of the adsorbed molecule is undesired and high energy barriers for dissociation are more suitable. All of these suggest that controlling the factors determining adsorption strengths and barriers for dissociation on a given system, allows ultimately controlling the reactivity of the system toward specific reactions.

Several recent studies have addressed the importance of understanding confinement effects on reactivity.[115-122] In the early 90's, Corma et al. had already described the phenomena in a series of studies associated with their observations of reactivity in zeolites;[123-125] a topic that is currently revisited by several groups.[121,126-128] Other work focuses on reactions inside carbon nanotube systems,[116,120] where it is claimed that due to the curvature effect there is an electronic redistribution of the π electron density of the graphene layers. Both in zeolites and inside carbon nanotubes, the electronic density of the atoms constituting the "caged" environment and those of the reactants, intermediates and products, may experience significant changes which make their chemical behavior to differ from bulk. These changes should be further enhanced if the participant atoms belong to transition metals, of well-known catalytic activity. In previous work, the reactivity of transition metal surfaces toward the dissociation reaction of diatomic molecules was found to increase when the dissociations take place in a confined space defined by two interacting metal surfaces separated by distances smaller than 5 Å.[22] The proximity of the metal surfaces at these small distances has been found to result in the presence of electrons in the gap between the surfaces.[22,25,27,31] Such electrons along with the interaction between the surfaces and the adsorbate, help reducing the activation

barriers for dissociation. The extent to which the barrier decreases was found to be directly related to the *additional charge* transferred to the molecule in these confined systems with respect to that on a single surface. This additional charge could be controlled by two main factors. First, the type of metal atoms forming the confined system since the electronic coupling with the states of the adsorbed molecule and the magnitude of the electron densities on the gap [25] depend on the nature of the specific element. The second factor is the specific reaction, since the most stable adsorption site and configuration of a molecule being adsorbed is a property of the molecule/surface system which also determines the distance between adsorbate and metal atoms on one of the surfaces.

Our previous results related the extent to which adsorption energies and energy barriers for dissociation of specific reactions are modified with respect to those on a single surface to the nature of the transition metal employed to build the metallic gap. In this work, we are interested in learning how the geometry of a specific system confined between metallic surfaces can affect adsorption strengths and dissociation barriers of adsorbates. The reaction chosen for the study is the dissociation of molecular oxygen confined between Pt (111) surfaces. This dissociation has been very well-studied on the Pt (111) surface due to its importance on relevant industrial catalytic processes, such as the oxygen reduction reaction in proton-exchange membrane fuel cells. In order to investigate the influence of the local structure of the surfaces forming the metallic gap, two different approaches are taken. First we analyze the relative positions of the platinum atoms forming the gap, with respect to each other. Second, we evaluate the influence of possible step-defects on the energetic of the reaction. The computational and system details are presented in section 2, the results in section 3 and the conclusions in section 4 of the paper.

4.3.Computational and System Details

Calculations were performed using the Vienna *ab initio* simulation package, VASP, [87-91] with the revised PBE functional (GGA-rPBE),[92] since this functional has been shown to improve the energetic for chemisorption of atoms and molecules on transition-metal surfaces. The projector augmented wave (PAW) pseudopotentials [93,94] provided in the VASP databases were used to describe the electron-ion interactions. The plane wave was expanded up to a cutoff energy of 400 eV. The convergence criteria for ionic relaxation loop and for electronic self-consistent iteration were set to 10^{-3} and 10^{-4} eV respectively, and a Methfessel–Paxton smearing of 0.2 eV was employed. Spin polarization was included in every simulation.

The adsorption strength of the molecular precursor was calculated by locating the O_2 molecule parallel to the surface and centered on bridge sites (known as top-bridge-top or t-b-t configuration), since this is the most stable chemisorption state for an oxygen molecule on a Pt-(111) surface.[61] In each simulation, the initial O–O distance was the gas phase value of 1.23 Å, as obtained from our DFT calculations. Adsorption energy (E_{ads}) was defined as the variation in energy due to bringing the O_2 molecule from the gas phase to the surface, and calculated using equation 2.1. $E_{2O/surf}$ stands for the total energy of the interacting surface and the adsorbed O_2 molecule, Es_{urf} is the total energy of the clean Pt (111) surface and E_{O2} represents the total energy of the molecular oxygen in gas phase.

$$E_{ads} = E_{2O/surf} - E_{surf} - E_{O2} \qquad (4.1)$$

Once the adsorption energies were calculated, the activation energies for O_2 dissociation were then obtained using the nudged elastic band (NEB) method.[96-98] In the final state, the separated oxygen atoms are located in threefold face centered cubic (FCC) hollow sites, which were determined as the most favorable locations for the dissociated oxygen atoms on Pt (111).[61] Bader charge analysis was used to calculate the total electronic

charge of an atom.[99,100] Within this method, the total electronic charge of an atom is approximated by the charge enclosed within the Bader volume defined by zero flux surfaces.

4.3.1. Influence of the Type of Planes Forming the Gap

The (111) crystallographic face of FCC-platinum was employed. The metallic gap was formed by bringing together two metal slabs, each with 6 layers modeled using 2 x 2 supercells (Figure 4.1). The two top and the two bottom layers of both slabs were allowed to relax, whereas the two layers in the middle were kept fixed, representing the ‘‘bulk’’ material. The optimum bulk lattice constant of Pt was determined as 3.98 Å, which compares well with the experimental value of 3.92 Å.[101] A 4x4x1 k-points Monkhorst–Pack [95] mesh sampling in the surface Brillouin zone was applied for the DFT calculations. Whereas, for the electronic density of states (DOS) calculations, a 16x16x1 k-points mesh sampling was used.

Periodic boundary conditions were applied in the x, y, and z directions for all the systems studied. Thus, the metal slabs are considered infinite in the x and y directions but the two slabs are separated from each other in the z-direction by a distance H and each system is separated from its periodic image in the z-direction by a 15 Å vacuum gap. Three different gap systems were studied, which are designated as A-A, A-B and A-C. The notation was chosen by using each of the three stacking planes of an FCC-(111) slab, A, B, and C, respectively, as shown in Figure 4.1. Basically, the three systems differ in the position of the atoms forming the gap, with respect to each other; e.g. in the case A-A the gap is formed by two A layers, meaning the platinum atoms on the top layer of the gap are exactly positioned above the atoms on the lower layer of the gap, separated by the distance H.

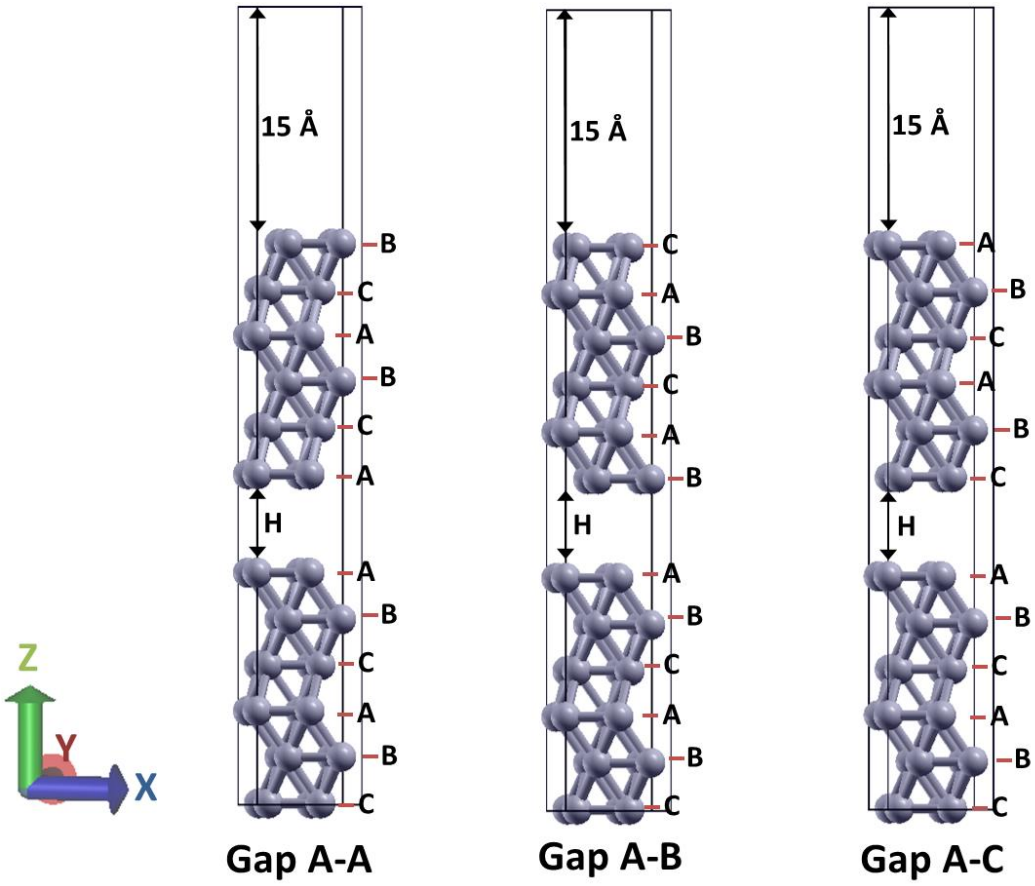

Figure 4.1 Unit cells of the three systems studied. Each one consisted of 2 slabs of 6 layers modeled using 2 x 2 supercells. The two slabs are separated from each other in the z-direction by a distance H and each system is separated from its periodic image in the z-direction by a 15Å vacuum gap

4.3.2. Role of Defects on the Layers Forming the Gap

For the results in this section, the metal slab consisted of 7 layers modeled using 2x8 supercells (Figure 4.2.a). In the case of the surface with steps (representing defects on a perfectly flat surface), some of the atoms on the layers forming the gap were removed (Figure 4.2.b). The close-packed plane (111) of the platinum FCC structure was used. The two top and the two bottom layers were allowed to relax, whereas the three layers in the middle were kept fixed, representing the ‘‘bulk’’ material. Periodic boundary

conditions were applied in x, y, and z directions for all the systems studied, resulting in infinite slabs in the x and y directions. The top (111) surface is separated from the image of the bottom (111) surface in the z direction by a distance H. In both cases (flat surface and surface with steps), the gap is defined by A-A layer interactions. Therefore, in this case the geometry, rather than the type of layers forming the gap, will be the variable to be studied. A 8x2x1 k-points Monkhorst–Pack [95] mesh sampling in the surface Brillouin zone was applied for the DFT calculations. Whereas, for the electronic density of states (DOS) calculations, a 16x4x1 k-points mesh sampling was used. In the case of the step, the oxygen molecule was also adsorbed on the t-b-t configuration on platinum atoms on the step, since is there where the gap is formed. However, it is important to notice that in this case, the platinum atoms involved on the adsorption of the molecule have also 9 nearest neighbors, as in the case of the flat surface, i.e. the molecule was not adsorbed on the low-coordinated platinum atoms at the edge of the step.

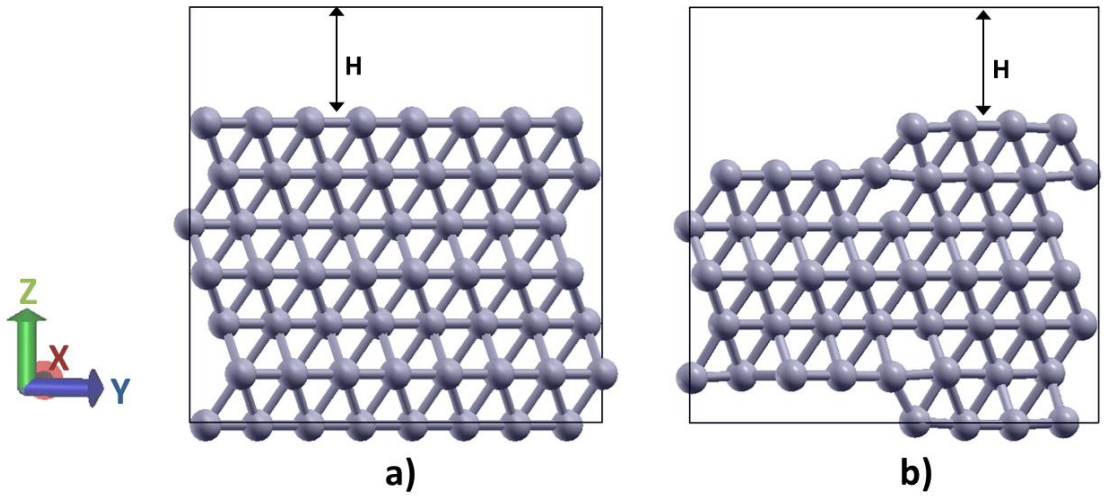

Figure 4.2 Unit cells of the two systems studied a) flat system, consisting of a slab of 7 layers modeled using 2x8 supercells b) surface with steps; in this case some of the atoms on the layers forming the gap were removed to model a step on the surface. After applying periodic boundary conditions, the top (111) surface of each system, is separated from the image of the bottom surface in the z-direction by a distance H

4.4.Results

4.4.1. Influence of the Type of Planes Forming the Gap

4.4.1.1.Optimization of the Metallic Gaps

The final surface-surface separation in the gap after the optimization was 4.9 Å, and the average charge of the layers forming the gap was -0.05 e/ atom, in the three different systems. No differences were observed between the electronic DOS of the different metallic systems shown in Figure 4.1, and the calculated number of electrons in the center of the gap corresponds to 0.03 electrons/Pt-atom in all the cases, in agreement with the value previously calculated with the PBE functional for a gap between platinum surfaces separated 5 Å.[25] All of this suggests that differences in the interactions with the adsorbates will be only given by geometric factors, i.e. the relative position of the layers forming the gap with respect to the adsorbate, since no electronic differences are observed between the different systems.

4.4.1.2.Adsorption of an Oxygen Molecule

The adsorption energies, bond lengths, and charges of the adsorbed oxygen molecules are reported in Table 4.1. The charge transferred to the molecules and their bond lengths are similar in the three cases. These values agree well with a previously calculated O-O bond length of 1.4 Å and charge of the O_2 molecule of -0.6 e, using the GGA-PBE functional for a molecule adsorbed on a Pt (111) confined system with a gap separation of 4.7 Å.[22] The larger bond-length and charge of the molecule with respect to the one adsorbed on a single platinum surface (1.35 Å and -0.43 e) ratifies the weakening of the oxygen-oxygen bond in confinement; specifically for gap separations smaller than 5 Å.

Table 4.1 Adsorption energies, charges and O-O bond lengths corresponding to the O_2 molecule adsorbed on the Pt (111) surface of the three different gaps

System	Adsorption Energy (eV)	O-O Bond Length (Å)	Charge O_2 molecule (e. u.)
Gap A-A	-0.14	1.39	-0.58
Gap A-B	-0.04	1.40	-0.61
Gap A-C	-0.04	1.40	-0.61

With respect to the adsorption strength, it is found to vary among the systems. The adsorption energy is 0.1 eV stronger in the case where the gap is formed by A-A planes than in the other two cases. In order to understand the origin of this difference, we calculated the DOS of the adsorbed molecules (Figure 4.3). The DOS of the molecule adsorbed on the A-B and A-C gaps are almost identical but that on the A-A gap displays some distinct features. The main difference with respect to the A-B and A-C cases is the energy splitting between the up and down spin configurations. Close to the Fermi energy, the spin-up π^* anti-bonding orbital of the A-A case is filled, while the spin-down π^* orbital is unoccupied. In the A-B and A-C cases, both the spin-up and down π^* orbitals appear half occupied. Therefore, even though the O_2 molecule is adsorbed on the t-b-t configuration in all the cases, the distributions of electrons inside the π^* anti-bonding orbitals of the molecules are different due to the relative positions of the metallic atoms forming the gap. This is reflected in the calculated magnetic moment of the adsorbed molecules; in the A-A gap system this is 0.48 μ_B, while it is 0.40 μ_B in the A-B and A-C systems. The latter value agrees with the magnetic moment of an oxygen molecule adsorbed on the t-b-t configuration on a platinum (111) surface, corresponding to a superoxo like paramagnetic precursor.[61]

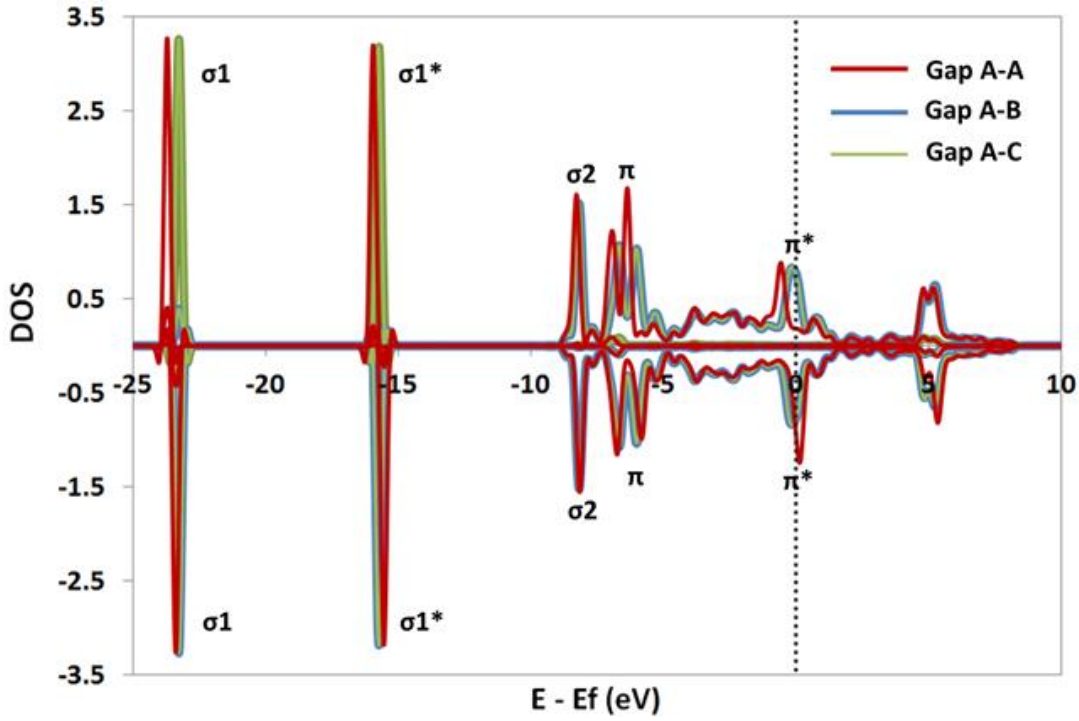

Figure 4.3 Electronic density of states (DOS) of the O_2 molecule chemisorbed on the Pt (111) surface of the three different gaps. The gap separation H is 4.9 Å. The horizontal axis represents the energy relative to that of the Fermi level (Ef)

Variations in adsorption strength can be related to two main factors: first, occupancy of the π^* anti-bonding orbital, which is related to the position of the p-band center of the O_2 molecule relative to the Fermi energy; and second, Pauli repulsion between the adsorbate states and the platinum d-states. Given the fact that all the adsorbed molecules possess similar transferred charges, the influence of the relative occupancy of the π^* anti-bonding orbital in the three cases may be negligible. This is corroborated by the position of the p-band center of the adsorbed molecules, which is equal in the three cases and corresponds to -8.2 eV. Therefore, the main factor influencing the adsorption energies in the different systems is related to the Pauli repulsion, i.e. the overlap between the orbitals of the oxygen molecules and the orbitals of the metallic system.

This overlap is expected to change among the systems in Figure 4.1 for two reasons. First, as mentioned above, the distribution of electrons inside the π^* anti-bonding orbital vary among the systems, and second, the platinum atoms on the top layer of the gap are positioned differently with respect to the surface where the molecule is adsorbed, which causes the electronic structure of the surface, on the three different cases, to be to some extent different from each other. The Pauli repulsion can be quantitatively estimated taking into account the coupling of the electronic structure of the molecule with that of the metal. Within the Newns-Anderson model, the position of the d-band center of a specific metal is related to the width of its projected d-DOS; [51] this is because its number of d-electrons must be preserved. Therefore, a d-band shifted up in energy means a DOS with a smaller band-width, and in this case, where all the molecules display the same p-band center, it means a smaller overlap of the molecular orbitals with those of the surface metal atoms, resulting in stronger adsorption energies. The calculated d-band centers for the systems in Figure 4.1 were -2.45 eV for the A-A gap and -2.50 eV for the A-B and A-C gaps. These values suggest a slightly larger Pauli repulsion on the A-B and A-C gaps, resulting on their weaker adsorption energies.

Another difference among the systems is a purely geometric factor that causes dissimilar strengths of electrostatic interaction between the adsorbate and the metal atoms on the top layer of the gap. In the case of the A-A gap, the oxygen atoms are closer to the platinum atoms on this top layer, than in the A-B and A-C systems. Such distances between the oxygen and Pt atoms are shown in Figure 4.4 as dotted red lines, and correspond to 2.95, 3.15 and 3.16 Å in the A-A, A-B and A-C cases, respectively. The greater proximity between the oxygen atoms and the top layer of the gap in the case A-A results in a stronger electrostatic interaction that can be observed in Figure 4.4**,** that shows the isosurfaces for an electron density of 0.09 e/Å^3. The observed sharing of electrons between the top layer of the gap and the molecule is clearly larger in the A-A system. This electrostatic interaction between the gap and the molecular precursor for dissociation seems to also enhance the adsorption of the molecule in the metallic gap.

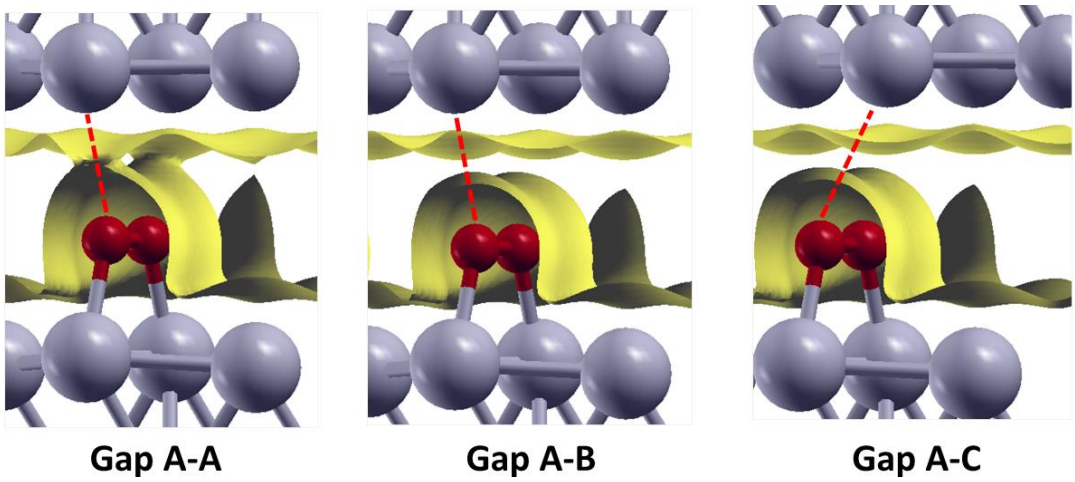

Figure 4.4 Isosurfaces corresponding to an electronic density of 0.09 e/Å³. The sharing of electrons between the adsorbed oxygen molecule and the metal atoms on the top layer of the gap is clearly larger in the gap A-A. Platinum atoms are gray and oxygen atoms are red. The red dotted line represents the shortest distance from the oxygen atoms to the platinum atoms on the top layer

4.4.1.3.Dissociation of an Oxygen Molecule

Figure 4.5 shows the energy pathway for dissociation of chemisorbed O_2 molecules in the metallic gaps shown in Figure 4.1, and the images of the corresponding intermediate configurations. The calculated activation energies are 0.50, 0.47 and 0.43 eV in the A-A, A-B and A-C systems respectively. The value for the A-C system agrees fairly well with the value 0.39 eV calculated using the GGA-rPBE functional, for the dissociation of O_2 in an equivalent gap of Platinum separated 4.9 Å.[22] The difference of 0.04 eV may be due to the use of updated potentials in the latest version of VASP.

Since the molecular precursors have similar charges and bond lengths, the strength of the O-O bond is similar at the beginning of the dissociation in the three metallic systems (Configuration 0, Figure 4.5). The different activation energies are most likely related to the interaction of the respective intermediate images with the top layer of the gap. In order to analyze this influence, isosurfaces of constant electron density were also plotted

(Figure 4.6) for the molecule adsorbed on the intermediate configurations leading to the transition state. Again, the strongest interaction between oxygen and platinum atoms on the top layer of the gap is observed in the A-A system. Therefore, the calculated activation barriers suggest that this interaction hinders the diffusion of the atoms to a different adsorption site, resulting in a higher barrier for the dissociation in the A-A gap; which is the system in which the oxygen molecule interacts strongly with this top layer.

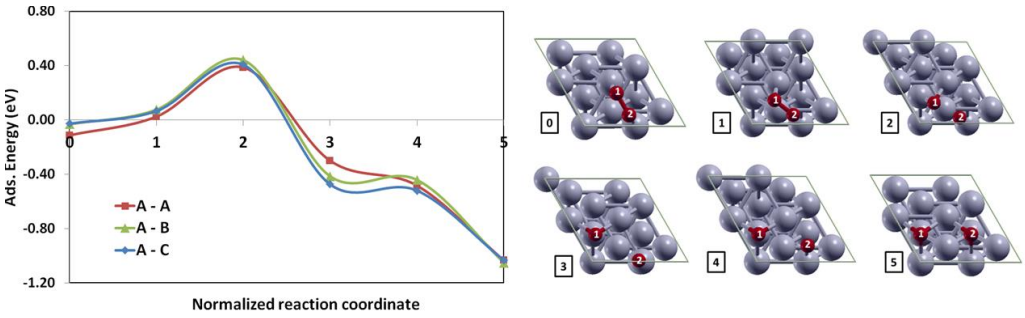

Figure 4.5 Left: Energy path for the dissociation of the chemisorbed O_2 molecules, on the Pt (111) surface of the metallic gaps shown in Figure 1. Right: Geometric configuration of the adsorbed molecule on the various intermediate images

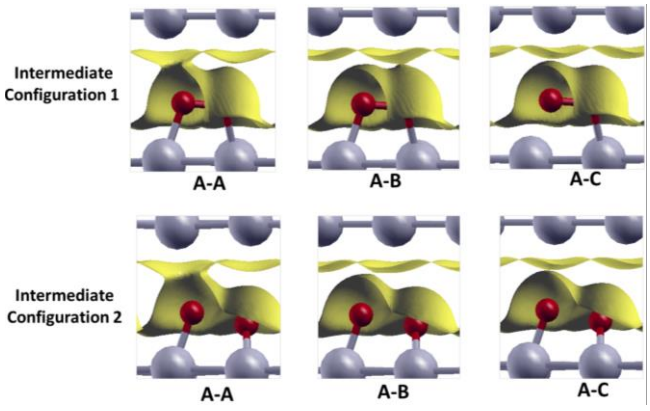

Figure 4.6 Isosurfaces corresponding to an electronic density of 0.07 e/Å^3, for the intermediate configurations leading to the transition states

The calculated results discussed in this section show the role that the top layer of the gap plays on the adsorption and dissociation of adsorbates in the metallic gap. This top layer modifies the electronic structure of the surface where the molecule is adsorbed, and also its interaction with the adsorbate helps its stabilization on the surface. On the other hand, the stronger the interaction, the more difficult is for the molecule to move away and therefore dissociate, resulting in higher energy barriers for dissociation.

4.4.2. Influence of Defects on the Layers Forming the Gap

4.4.2.1.Optimization of the Metallic Gaps

The average gap separations for the optimized systems shown in Figure 4.2 are presented in Table 4.2. A stronger attraction in the confined geometry is evidenced for the flat surfaces, resulting in smaller final gap separations; this stronger attraction may be the cause of the slightly larger number of electrons, per platinum atom, calculated at the center of the gap of the flat surfaces with respect to the number found in the stepped system of Figure 4.2.b (Table 4.2). The average charge of the layers forming the gap was calculated and is shown in Table 4.2. The average charge is similar in both cases. However, a somewhat larger transference of charge is expected for molecules adsorbed in the flat gap based on the slightly larger number of electrons in the gap and charge of the platinum layers forming the gap.

A small surface reconstruction is observed on the step of the system in Figure 4.2.b for both separations, which results in a minor lattice strain of about 1.0% with respect to the one on the flat surface. The electronic DOS of these systems were also calculated; the d-band center of the metal is found to be -2.05 eV for the flat surface and -1.93 eV for the surface with the step, at both separations. A d-band center shifted up in energy was expected for the surface with the step because of the lower average number of metal neighbors in this surface. This would result in molecules adsorbing more strongly in the low coordinated sites of the substrate. However, in this case, the oxygen molecules are not adsorbed on the edges of the step but using the t-b-t configuration on metal atoms

with the same coordination number as in the flat surface (9 nearest neighbors). Therefore, the position of the d-band center of the clean substrate alone is not enough to predict the strength of adsorption energies on the t-b-t configuration of these confined metallic systems.

Table 4.2 Average gap separations in the two systems shown in Figure 4.2, average charge of the layers forming the gap and total number of electrons in the center of the gap for two initial separations: 5.0 and 5.5 Å

System	Initial metal-metal separation, H (Å)	Final metal-metal separation, H(Å)	Charge of layers forming the gap (e/Pt-atom)	Electrons in the center of the gap (e/Pt-atom)
Flat	5.5	5.2	-0.04	0.04
Flat	5.0	4.7	-0.04	0.02
Steps	5.5	5.5	-0.03	0.02
Steps	5.0	5.0	-0.03	0.01

4.4.2.2.Adsorption of an Oxygen Molecule

The adsorption energies, bond lengths and charges of the oxygen molecules adsorbed on the systems shown in Figure 4.2 are reported in Table 4.3 for final gap separations of 5.23 and 5.36 Å, for the flat surface and the surface with the step, respectively. There is a decrease in the initial separation of the gap formed by the steps due to the presence of the oxygen molecule, from 5.50 Å when the surface was clean to 5.36 Å when the molecule is adsorbed; however, the gap is still larger than the one formed on the flat

system (5.23 Å), which confirms the stronger interaction between the metal layers forming the gap in the latter.

The charge transferred to the adsorbed molecules and their bond lengths are similar in both systems, with the charge of the oxygen molecule being slightly larger in the case of the flat surface, as discussed in the previous section. However, the adsorption energy is stronger on the flat system by approximately 0.08 eV, with respect to the energy of the molecule adsorbed on the surface with the step. The electronic DOS of the molecules was calculated and they look almost identical, with the position of the p-band center corresponding to -8.2 eV in both cases. Therefore, the occupancy of the π* anti-bonding orbital is not the cause of the different adsorption strengths.

Table 4.3 Adsorption energies, charges and O-O bond lengths corresponding to the O_2 molecule adsorbed on Pt (111) surfaces of the systems shown in Figure 4.2

System	Final metal-metal separation, H (Å)	Adsorption Energy (eV)	O-O Bond Length (Å)	Charge O_2 molecule (e. u.)
Flat	5.23	-0.20	1.39	-0.59
Steps	5.36	-0.12	1.39	-0.58

As in section 4.4.1.2**,** variations in adsorption strengths may also be related to differences in the overlap between orbitals of the oxygen molecule and orbitals of the metallic system. The calculated electronic structure of the metal in the two systems reveals that the d-band centers are -2.36 eV for the flat surface and -2.44 eV for the surface with the step. These values suggest a slightly larger Pauli repulsion in the system with the step that results on weaker adsorption energy.

Additionally, even though the types of layer forming the gap are the same on both systems (A-A), the geometry of the system with the step causes the atoms forming the gap to buckle with respect to the plane of the surface and slightly move off their initial positions. This deformation, along with the slightly larger separation of the gap in this case, causes the distance from the oxygen atoms to the top layer of the gap to be larger compared to that on the flat system. The distances correspond to 3.3 Å in the flat system and 3.5 Å in the surface with the step. Therefore a slightly stronger electrostatic interaction between the molecular precursor and the platinum atoms is observed in the former, leading to additional stabilization of the adsorbate on the flat surface.

Comparisons for the initial separation H = 5 Å are not possible, because in this case the molecule undergoes spontaneous dissociation when adsorbed on the surface with the step. In both cases, flat surface and surface with steps, the final separation of the gap (after the molecule was adsorbed) corresponds to 4.7 Å. In the case of the flat surface, where the molecule did not spontaneously dissociate, the charge transferred to the oxygen molecule is larger than in the previous cases, and corresponds to -0.63 e.u. with an oxygen-oxygen bond length of 1.43 Å. The adsorption energy of the molecule is the same as in the case of H = 5.23 Å, corresponding to -0.20 eV.

4.4.2.3.Dissociation of an Oxygen Molecule

Figure 4.7 shows the energy pathway for dissociation of chemisorbed O_2 molecules in the gaps shown in Figure 4.2 at the metal-metal separations shown in Table 4.3; the images of the intermediate configurations are equivalent to those presented in Figure 4.5. The calculated activation energies for the separations 5.23 Å (flat surface) and 5.36 Å (surface with steps) are 0.61 and 0.46 eV, respectively. The charge and bond length of the molecular precursors show that the O-O bond strength at the beginning of the dissociation is similar in the two systems. Consequently, the easiness with which a molecule is dissociated will be given by the strength of its electrostatic interaction with

the top layer of the gap. As mentioned in the previous section, this interaction is stronger on the flat system, which makes more difficult the diffusion of the atoms on the surface, and results in higher barriers for dissociation than in the case where the surface has a step. It is clear in Figure 4.7 that, even though the initial state is very similar in both cases, the molecule reaches the transition state faster in the surface with the steps due to the easiness with which the atoms can diffuse and separate in this case.

The most stable configuration for the dissociated oxygen atoms on the stepped surface separated 5.36 Å consists of the oxygen atoms positioned on bridge sites, while in the other two cases shown in Figure 4.7 it consists of the two oxygen atoms adsorbed on fcc-hollow sites.

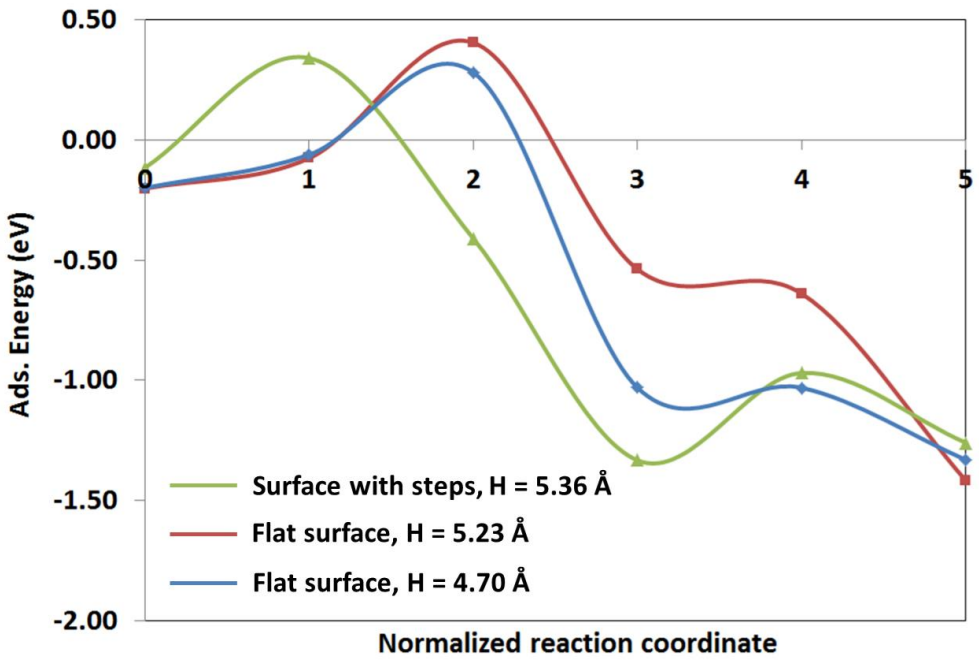

Figure 4.7 Energy pathway for dissociation of chemisorbed O_2 molecules on the Pt (111) surface of the metallic gaps shown in Figure 4.2

In the case of the flat surface with the 4.7 Å gap separation, the larger bond-length and charge of the molecule clearly reveal a weakened bond compared to the one for a gap separation of 5.23 Å. It is then expected a smaller barrier for the dissociation of the molecule regardless of the strength of its electrostatic interaction with the top layer of the gap. The latter contribution seems to only become important when comparing molecules with similar bond strength. The calculated barrier for dissociation was 0.48 eV, in agreement with the discussed weakening of the oxygen-oxygen bond. In the case of the stepped surface, for this smaller gap separation, the transference of charge to the molecular precursor at early stages of adsorption is similar to the one on the flat surface; however, as found in previous sections, the oxygen atoms can move more easily on this surface due to the weaker electrostatic interaction with the top layer of the gap, and in this case, they undergo spontaneous dissociation under the same bond length weakening.

4.5. Conclusions

In this study, we examined adsorption of an oxygen molecule on the t-b-t configuration and its dissociation in platinum gaps of separations between 5.36 and 4.70 Å. We compared the effect of the different gap geometries on the adsorption strength and barriers for dissociation.

Three surface-surface configurations were studied: A-A, A-B and A-C, named after the ABC structure of the fcc metals, and it was found that it affects adsorption and dissociation in two ways. First, the specific surface-surface configuration modifies the electronic structure of the surface where the molecule is adsorbed, modifying the width of its d-orbital and therefore the adsorption strength due to changes in the overlap of the molecular orbitals with the metal d-band. Second, the top layer may interact electrostatically with the adsorbate with more or less strength depending on their proximity: the stronger the electrostatic interaction, the larger the enhancement of the adsorption strength. However, this interaction may also make more difficult for the

molecule to move away and therefore dissociate, resulting in higher energy barriers for dissociation, when compared with molecules with similar bond-strength.

Possible effects of geometrical defects on confinement reactivity were assessed by adsorbing a molecule on the t-b-t configuration in a gap formed by steps of the (111) crystallographic face. Adsorption was followed by dissociation, and the results were compared to those obtained on a totally flat (111) surface with no defects. In general, the top layers forming the gap of the flat interacting surfaces attract each other with larger strengths, resulting in smaller gap separations after their optimizations. Also, the geometry of the steps causes the atoms forming the gap to buckle with respect to the plane of the surface and slightly move off their initial positions. The geometric differences result in different d-band centers of the systems and therefore, different adsorption strengths. Additionally, a larger electrostatic attraction is found between the oxygen molecule and the gap of the flat system, which helps to stabilize the adsorbed molecule but as remarked above, the atomic motion on the surface may become more difficult and result on larger barriers for dissociation.

These results show the importance of the geometry of the layers forming the metallic gap on reactivity. If a strong adsorption is desired, then a top layer strongly interacting with the adsorbate is convenient. This is possible, for example, using a gap like the type A-A studied in section 4.4.1. Whereas, if a small barrier for dissociation is preferred, then a weaker interaction between the molecular precursor and the top layer of the gap is more convenient; which can be achieved by using gaps formed by A-B or A-C layers or even having a surface with defects steps-like, such as the one discussed in section 4.4.2.

We note that our model considers pores subjected to adsorbate-induced surface relaxation, which we anticipate to be realistic on the basis of the well-known reconstruction phenomenon observed theoretically[129,130] and experimentally[131] on transition-metal surfaces. However, similar electronic migration behavior and

consequently chemical effects are expected inside of pores of fixed size, as shown recently.[25]

5. CHARACTERIZATION OF ELECTRONIC STATES INSIDE METALLIC NANOPORES [*]

5.1.Summary

Previous work has shown that unusual chemistry can be induced inside metallic slit nanopores. This phenomenon has been attributed to the presence of an enhanced electronic density within the pore. Here we use ab initio density functional theory and post-Hartree-Fock correlated methods to characterize the electronic density in the gap defined by two parallel metallic surfaces. In the first part of this work, the electronic density of states of several transition metal-nanopores is calculated for different pore sizes (i.e., surface-surface separations). Results show the existence of a critical surface-surface separation below which electronic states corresponding to the gap between surfaces become populated at energies below the Fermi level of the metal, leading to the presence of electrons in the pore. Further reduction in the nanopore size increases the number of states corresponding to the gap, which agrees with the increasingly higher electronic densities found in the gap for smaller surface-surface separations. In the second part of this work, the presence of electrons in the gap between two finite platinum layers (each layer composed by 4 to 13 atoms) is assessed using density functional theory and correlated ab-initio methods, to analyze the dependence of the electronic density observed in these nanopores on the computational method employed.

---

[*] Reprinted with permission from Julibeth M. Martinez de la Hoz, Gustavo E. Ramirez-Caballero, and Perla B. Balbuena. "Characterization of Electronic States inside Metallic Nanopores". The Journal of Physical Chemistry C 2013 117 (36), 18406-18413. Copyright (2013) American Chemical Society

5.2.Introduction

Chemical adsorption of molecules on surfaces is an important step involved in a variety of processes, among them heterogeneous catalysis. After adsorption there is an electronic coupling between catalyst and adsorbate which generates changes in their electronic structures, facilitating the breaking and/or formation of new chemical bonds. In the case of transition metal catalysts, the coupling of the adsorbate orbitals with the s- and d-band of the metal results in broadening of the molecular orbitals and the formation of bonding and antibonding states. The relative occupancy of these states depends on the Fermi energy of the metal. Additionally, the electronic overlap between molecular and metallic states creates the so called Pauli repulsion, which debilitates the interaction between adsorbate and substrate.[132] Therefore, upon adsorption, the strength with which an adsorbate is attached to the surface and the weakening of its molecular bond will be determined by the Fermi energy of the specific transition metal employed and by the overlap between its electronic states with those of the adsorbate.

In previous works we have shown that both adsorption energies and activation barriers for the dissociation of diatomic molecules can be modified by adsorbing the molecules on a metallic surface which is separated from another one at distances between 4-7 Å.[21,22,31] There are two new effects on molecules adsorbed on these metallic slit nanopores, compared to those adsorbed on single surfaces. First, there is a geometric effect given by the presence of the second surface. Interactions between the adsorbed molecule and this second surface enhance the strength of the adsorption. Also, the presence of the top surface may propitiate changes in the d-band width of the surface to which the molecules are attached, resulting in further variations of the adsorption strengths.[21] Additionally, the effect of the top surface on activation barriers for dissociation was found to be related to the strength of its interaction with the adsorbed molecule. Stronger interactions may hinder the ability of the molecule to diffuse on the surface and therefore dissociate.[21] The second effect found as a result of adsorbing molecules in nanopores is an electronic one. The strong interaction between the metal

surfaces close to each other at these small distances (4-7 Å) gives rise to the development of significantly high electronic density in the gap between the surfaces forming the pore.[21,22,25,27,31] The electron-rich environment helps increasing the charge transferred to adsorbed molecules compared to that transferred to the same molecules on single surfaces. A direct relationship exists between the additional charge transferred and the decrease found in activation barriers for dissociation.[22]

How may these confinement phenomena be realized in experiments? Recent related work has reported interesting interparticle coupling phenomena that have been widely observed when two metallic nanostructures are in close proximity.[24,29,133-135] When the particles are separated by sub nanometer distances, quantum effects become important. Specifically, the electron potential barrier between the nanoparticles decreases thus allowing tunneling of some of the conduction electrons.[25,28,136,137] Several experimental and theoretical works have reported the formation of a conductive channel in the interparticle region between two metallic nanostructures, as a result of migration of electrons to this gap.[24,25,28,29,133-137] This phenomenon is strongly dependent on the gap distance; small but finite electronic densities have been calculated for interparticle distances below 7 Å.[25,29] For even smaller separations, the electronic coupling becomes stronger allowing electron flow between the particles under local applied electric fields.[24,25,28,29,133-137] This electronic coupling between metallic particles has been suggested to be analogous to a bond formation process. As such, variations in the energy levels of the system are observed including the appearance of new electronic levels as the particles approach each other.[29] Given the importance of the electrons found in the gap between metallic surfaces on the reactivity of these metallic nanopores, a clear understanding of the electronic changes experienced by the system as the surfaces approach each other and their relation with the specific metal is necessary. Moreover, knowledge of the energetic states of electrons in different metallic pores may allow adequate coupling of these systems with electronic states of molecules of interest. Also,

the relationship between pore-size and electronic density may allow tuning the electronic properties of the pore for specific adsorption and/or dissociation processes.

Confinement effects on reactivity have also been investigated.[115-121] In the early 90's, Corma et al. had already described the phenomena in a series of studies associated with their observations of reactivity in zeolites;[123-125] a topic that has been revisited by several groups.[121,126-128] Other work focuses on reactions inside carbon nanotube systems,[116,120] where it is claimed that due to the curvature effect there is an electronic redistribution of the π electron density of the graphene layers. Both in zeolites and inside carbon nanotubes, the electronic density of the atoms constituting the "caged" environment and those of the reactants, intermediates, and products may experience significant changes which make their chemical behavior to differ from bulk. The described effects should be further enhanced if the participant atoms belong to transition metals, of well-known physico-chemical activity. In this work we evaluate the electronic density of states of several transition metal-nanopores for different pore sizes (i.e., surface-surface separations). These geometries have some similarity with Pt nanotubes recently reported.[138] In addition, we analyze the dependence of the electronic density observed in these nanopores on the computational method employed. For this, we assess the presence of electrons in the gap between two finite platinum layers (each layer composed of 4 to 13 atoms) using density functional theory (DFT) and ab-initio correlated methods.

5.3.Computational and System Details

5.3.1. Calculation of Electronic DOS of Metallic Nanopore Systems

Calculations were performed using the Vienna Ab Initio Simulation Package, VASP,[87-91] with the revised PBE functional (GGA-rPBE)[92] and the projector augmented wave (PAW) pseudopotentials provided in the VASP databases describing the electron-electron and electron-ion interactions.[93,94] The plane wave was expanded up to a cutoff energy of 400 eV. The convergence criteria for ionic relaxation loop and for electronic

self-consistent iteration were set to 10^{-3} and 10^{-4} eV respectively, and a Methfessel–Paxton smearing of 0.2 eV was employed. Spin polarization was included in every simulation with a 9x9x1 k-points Monkhorst–Pack[95] mesh sampling in the surface Brillouin zone.

The (111) crystallographic face of the face centered cubic crystal (FCC) of every transition metal was employed. The optimum bulk lattice constants of Ir, Rh, Ni, Co, Cu and Ag were determined as 3.88, 3.84, 3.53, 3.52, 3.64 and 4.16 Å, respectively, which compare well with the experimental values of 3.84, 3.80, 3.52, 3.54, 3.67 and 4.09 Å.[101] The metal slab consisted of 9 layers modeled using 2 x 2 supercells (Figure 5.1). Periodic boundary conditions were applied in the x, y, and z directions for all the systems studied, resulting in infinite slabs in the x and y directions; while the top (111) surface, is separated from the image of the bottom (111) surface in the z direction by a distance H.

H, the surface-surface separation or nanopore length, was chosen as a function of the layer-layer separation of the optimized slab (*l*, shown in Figure 5.1). Thus, an optimization of the slab at a large H (H = 15 Å) was first performed with the aim of determining the *l* value for each transition metal. Then, the layers of the slab were kept fixed in order to perform band decomposed charge density calculations at specific H values, corresponding to 1.5*l*, 2.25*l*, 3*l*, and 5*l*. All the calculations were performed between (E_{Fermi} − 10) eV and (E_{Fermi} + 20) eV. Subsequently, the charge density was integrated for both the whole system and the spatial region defined as the gap (Also shown in Figure 5.1**)**. This region was defined right in the middle between the two surfaces forming the gap, in the z-direction, and it is 1 Å thick.

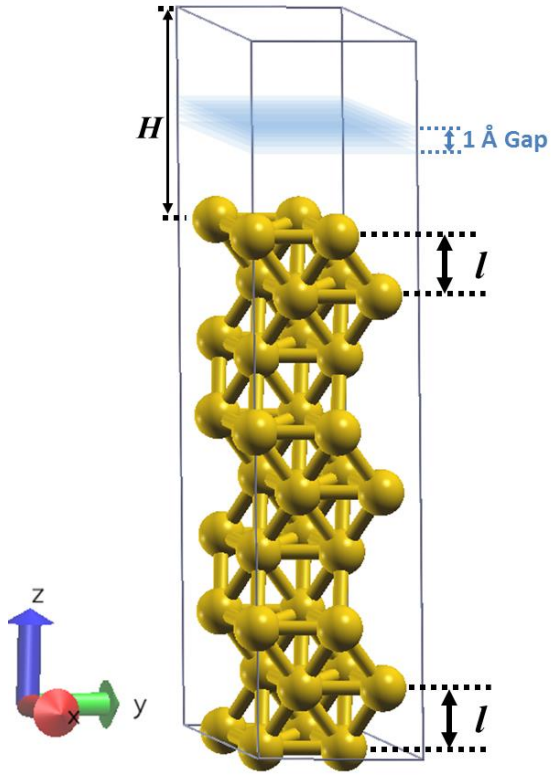

Figure 5.1 Unit cell of the metallic systems studied, consisting of 9 layers modeled using 2 x 2 supercells. Each system is separated from its periodic image in the z-direction by a distance H; l represents the layer-layer separation and the blue region represents the 1-Å spatial gap between the surfaces

5.3.2. Calculation of Electronic Density in the Gap Between Finite Platinum Layers

Calculations were performed using the Gaussian09 (G09) simulation software.[139] Three different systems were employed for the calculations, consisting of two layers of four platinum atoms each (Figure 5.2.a), two layers of thirteen platinum atoms each (Figure 5.2.b), and four layers of thirteen platinum atoms each (Figure 5.2.c). The geometry of the layers was chosen in such a way that comparisons with the slab geometry employed in our previous calculations were possible. Initially the layers are optimized separately

and then they are kept fixed at 5 Å to calculate the electronic density in the gap between them using single-point calculations. The self-consistent iteration convergence criterion employed was 10^{-8}, with the exception of the calculation using the CCSD (T) method were the criterion was 10^{-6} due to the high computational cost. The Merz-Singh-Kollman (MK) scheme was employed for charge calculations.[140] In this method, charges are distributed aiming to fit the electrostatic potential of the molecular system. Information about the electronic density distribution was extracted from the G09 checkpoint file by using the cubegen utility and integrating the charges over the desired region (1 Å gap between surfaces, equivalent to the one showed in Figure 5.1). Up to now, all of the electronic density calculations that we have reported for metallic nanopores have been based on periodic systems, employing plane-wave DFT calculations.[21,22,25,27,31] Therefore, this part of the work will allow us to understand the influence of the computational method employed on the calculated electronic properties of the nanopores.

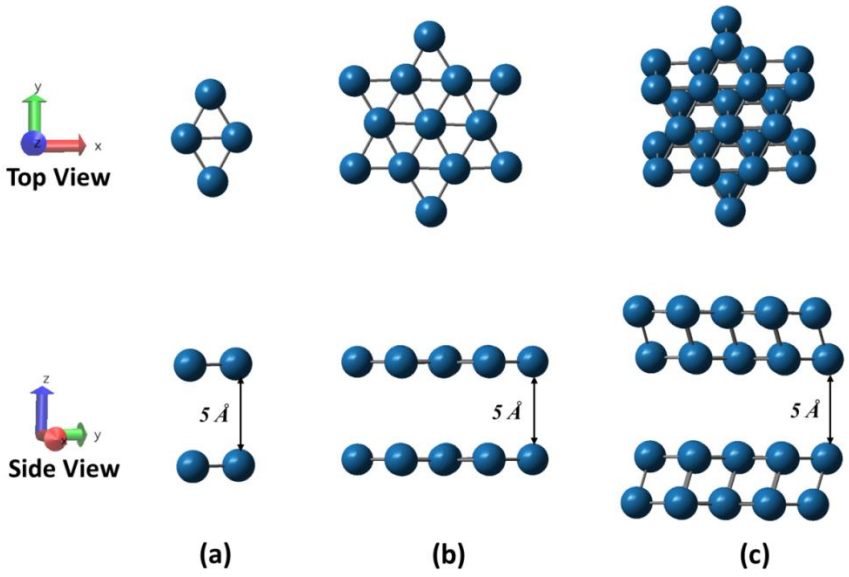

Figure 5.2 Systems employed for electronic density calculations (a) 2 layers of 4 platinum atoms (b) 2 layers of 13 platinum atoms (c) 4 layers of 13 platinum atoms

Two different types of calculation methods are used to evaluate the electronic density of the systems: hybrid-DFT (three-parameter Becke exchange functional in conjunction with the Perdew and Wang correlation functional, *B3PW91;* [47] and Minnesota 2005 hybrid meta functional by Zhao and Truhlar *MO5-2X* [141]), and correlated post-Hartree Fock methods (Second order Møller-Plesset perturbation theory *MP2* [142-147]; and Coupled-Cluster method with double, single excitations, and a quasi-perturbative treatment of triple excitations *CCSD(T)* [148]). The latter provides significant improvement over pure Hartree-Fock based methods since the d-orbitals of transition metals are very close in energy and correlation effects are found to be very important when the energies of occupied and unoccupied states approach each other.[36] Regarding the basis set, the LANL2DZ, [149] which is suitable for transition metals, was employed in most of the calculations. However, the effect of a slightly enlarged valence d-space was evaluated by using the LANL2TZ basis set; [150] since a more diffuse function allows a better description of the electronic density further away from the nucleus. [36]

For hybrid-DFT methods, spin multiplicities were chosen based on the final geometry of the optimized layer, i.e. the multiplicity yielding the planar structure with the lowest energy was the one employed. The multiplicities investigated for the Pt cluster are reported as Supplementary Information (Figure S6). This is because comparison with systems similar to the one shown in Figure 5.1 is desirable. Regarding post-HF methods, spin multiplicities were set to the value obtained for the M05-2X level of theory.

5.4.Results

5.4.1. Calculation of Electronic DOS of Metal-Nanopore Systems

Table 5.1 shows the calculated layer-layer separation *l* for the different metal-slabs and the number of electrons in the 1Å-gap for the surface-surface separations H, corresponding to 1.5*l*, 2.25*l*, 3*l*, and 5*l*. It is interesting to note that for every system, below a certain H corresponding to 3*l*, an electronic density appears in the gap between the surfaces, i.e. the number of electrons in the gap is larger than zero. Also, further

decreases in H result in a larger number of electrons in the gap as expected from narrower electron potential barriers between the surfaces.[25,28,136,137] Although the onset for migration of electrons to the gap is approximated to 3*l*, the exact onset is related to the work function of the material forming the pore.[25] As reported in a previous work, the amount of electrons migrating to the gap for a fixed metal-metal separation correlates fairly well with the position of the metal in the periodic table and its corresponding work function.[25] It was found that the amount of electrons in the gap increases as the atomic number decreases in a given period, for metals in the 4^{th}, 5^{th}, and 6^{th} row. This trend is agreement with that of the work function in the periodic table, which is found to decrease with decreasing atomic number.[151] The exception to this trend was found for transition metals in the 11^{th} group since their outermost d-orbital is full with ten electrons, making more difficult the migration of atoms from these surfaces. Additionally, increasing amount of electrons was found in the gap between surfaces as the period decreases, which also coincides with decreasing work functions in the periodic table.

After an onset for migration of electrons to the gap has been estimated for the different metallic systems (H = 3*l*), variations in the electronic structure are studied by analyzing the electronic DOS of the different systems. As an example, Figure 5.3 shows the one calculated for a Ag-nanopore at various surface-surface separations. The blue line corresponds to the DOS of the whole system, while the red line represents the partial DOS for the 1Å-gap region between the surfaces (defined in Figure 5.1). While the DOS of the system experiences no significant changes as the surface-surface separation decreases, the one of the spatial region defined as the gap undergoes substantial changes. For the largest separation, H corresponding to 5*l* (12.1 Å), the electronic levels corresponding to the gap, are all above the Fermi energy, and therefore there are no electrons in the gap; however, as H decreases below 3*l* (7.23 Å) some electronic levels appear below the Fermi energy. Consequently, these levels are occupied and an electronic density arises in the gap region between the metallic surfaces. This

phenomenon is in agreement with the formation of a *bond* between closely interacting metallic nanostructures, as reported for dimers of silver nanoclusters. [29] Similar results were obtained for all of the other metallic nanopores; DOS plots for all of the metallic systems are provided as Supporting Information (Figs. S1 to S5).

Table 5.1 Calculated layer-layer separation l, for the different metal-slabs, and number of electrons in the 1Å-gap for H equal to 1.5l, 2.25l, 3l, and 5l

System	**Calculated *l* (Å)**	**Number of electrons in the gap**			
		1.5*l*	**2.25*l***	**3*l***	**5*l***
Co	2.03	2.20	0.32	0.05	0.00
Rh	2.21	2.22	0.24	0.03	0.00
Ir	2.24	2.60	0.26	0.03	0.00
Ni	2.04	2.02	0.28	0.04	0.00
Cu	2.10	1.74	0.24	0.03	0.00
Ag	2.41	1.34	0.13	0.01	0.00

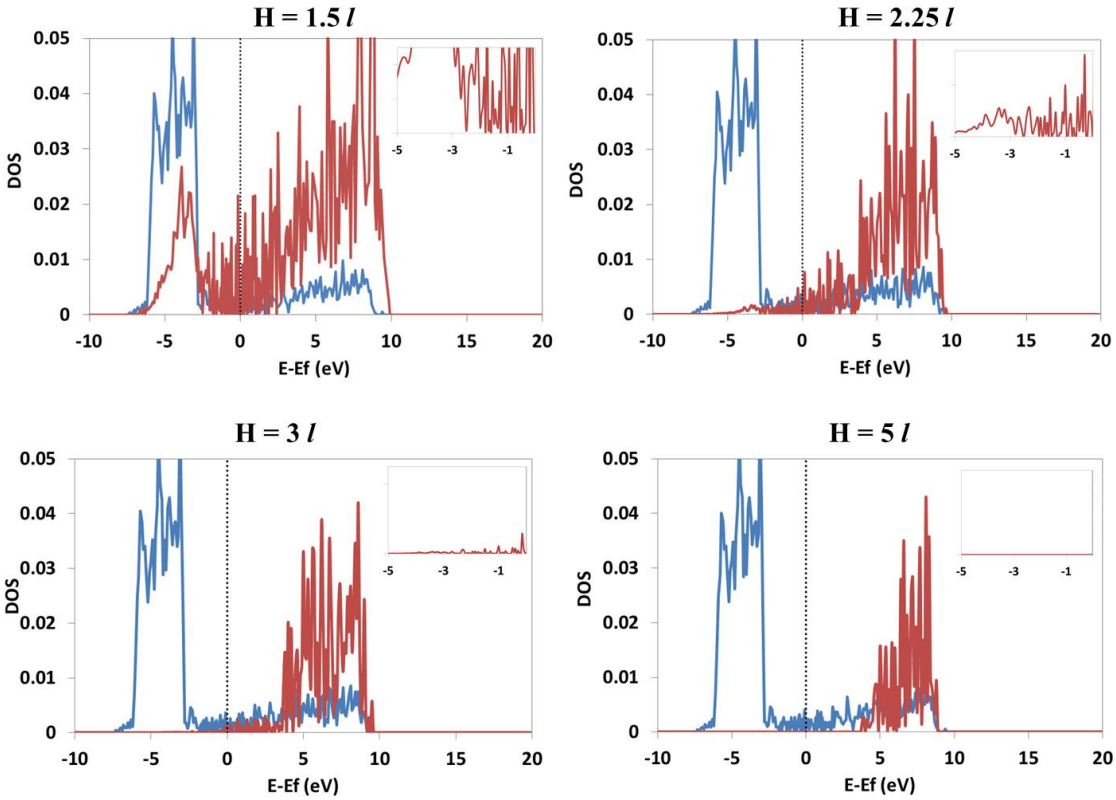

Figure 5.3 DOS of Ag-nanopore at various surface-surface separations, H. The blue line corresponds to the DOS of the whole system, while the red line represents the partial DOS for the 1Å-gap region between the surfaces. The insets correspond to a zoom-in of the red line for the x-axis range between 0 and -5 eV

The critical distance for the existence of electronic density between the surfaces, chosen as the one where electronic levels below the Fermi energy are first observed (Figure 5.3), agrees with the distance where the number of electrons calculated in the gap is larger than zero (onset for migration of electrons to the gap, corresponding to 3*l*). This value constitutes a good approximation to estimate the critical separation for other transition metal systems; *l* can be easily estimated since the layer-layer separation of the (111) face of fcc metals is related to their lattice constant. The critical separation is

extremely important to achieve the electronic effect reported for these small pores (size range of 4-7 Å). Electrons found in the gap between surfaces interacting at these small distances may interact with adsorbates present inside the pores inducing interesting chemical and physical effects. Some of them include changes in magnetization behavior,[26] induced polymerization of molecules,[27] and reduction in activation barriers for dissociation. [21,22]

Another important result that can be derived from the DOS plots is the energy of the electrons in the gap-region between the surfaces. For example in the case of Ag (Figure 5.3), the energy of these electrons for the separation 3*l* (H= 7.2 Å) is within 3 eV of the Fermi Energy; for 2.25*l* (H = 5.4 Å) it is approximately between E_f and E_f – 5 eV; and for the smallest separation 1.5*l* (H= 3.6 Å) their energies span the whole region occupied by the metallic surfaces starting from the Fermi energy. In general, this is the case for all of the systems studied (See Supporting Information Figs. S1 to S5). Thus, it is possible to estimate the specific energies of the electrons in that spatial region. The range of energies of such electrons varies with the separation, H. However, most practical nanopores would have surface-surface separations between 4-7 Å; thus the energy of the electrons in the gap region will generally be within 5 eV of the Fermi energy of the metallic system.

The results of this section are very important for the design of metallic nanopores as active catalysts for specific reactions. Firstly, they allow designing the nanopores with desired electronic densities between the metallic surfaces by changing the surface-surface separation (pore length). As reported in previous works this electronic density helps increasing the charge transferred to molecules adsorbed on the nanopores, which weakens the molecular bonds and reduces activation barriers for dissociations. [21,22,25,27,31] Additionally, it is possible to *choose* the energy of the electrons in the gap-region by choosing the metal forming the nanopore. Energy coupling between electrons and molecular orbitals is required for charge transfers to be effective. Therefore, knowing in

advance the energy of electrons in the gap region may allow more effective design of the catalysts for their interaction with specific molecules.

5.4.2. Calculation of Electronic Density in the Gap Between Finite Platinum Layers

The system composed of two layers of 13 platinum atoms (Figure 5.2.b**)**, was employed for the evaluation of the DFT-hybrid methods; even though, both B3PW91 and M05-2X are DFT-based they offer some advantages over pure DFT-GGA methods regarding electron correlation. The latter includes medium and long-range correlations in an approximate way on the exchange part of the functional, whereas hybrid-DFT mixes in with the Hartree-Fock exchange allowing an explicit description of the densities and their gradients through orbital dependent expressions. Additionally, the M05 hybrid-meta functional has been found to correctly predict weakly non-covalent interactions,[38] a situation somewhat similar to the one described in our interacting metallic surfaces.

Figure 5.4 (left and center) shows electronic density plots for a surface-surface separation of 5 Å and the number of electrons per platinum atom calculated in the 1Å-gap between the surfaces. The calculated number of electrons is practically the same in both cases, corresponding to 0.026 and 0.028 for the B3PW91 and M05-2X methods, respectively. In order to compare with our periodic DFT GGA-RPBE calculations, we calculated the number of electrons in the gap of a 2x2 Platinum (111) system, equivalent to the one depicted in Figure 5.1, using the VASP package**;** the surface-surface separation was also fixed at 5Å and the calculated number of electrons in the 1Å-gap was 0.026. Thus, results using the GGA-RPBE method are in agreement with the ones obtained from hybrid-DFT methods.

It is important to note that the model employed with the GGA-RPBE method has nine layers (Figure 5.1), while the one employed with the hybrid-DFT methods has only two (Figure 5.2.b). Therefore, in order to evaluate the effect of the number of layers on the

results obtained with hybrid-DFT methods, the model shown in Figure 5.2.c was also employed to evaluate the electronic density using the M05-2X method with the LANL2DZ basis set. The number of electrons calculated with the four-layer model was 0.026 per platinum atom (Shown in Figure 5.4.c). Thus, a larger number of layers induces a slight decrease in the number of electrons in the 1Å-gap; however, the reduction is only in the order of 6% and results obtained using a two-layer model (Figure 5.2.b) are still quantitatively accurate.

Another useful factor to evaluate is the size of the basis set; the LANL2TZ has a slightly larger valence d-space than the LANL2DZ, which is the one typically employed for transition metals. The system shown in Figure 5.4 (center) was also evaluated using the M05-2X method with the LANL2TZ basis set. Nevertheless, the calculated number of electrons in the 1Å-gap was practically the same as the one calculated using the LANL2DZ basis set (0.026 electrons/Pt atom); thus, no significant differences are found on the electronic density calculated in the 1Å-gap between metallic surfaces by changing the number of layers employed to model the system or by moderate increases in the basis set size.

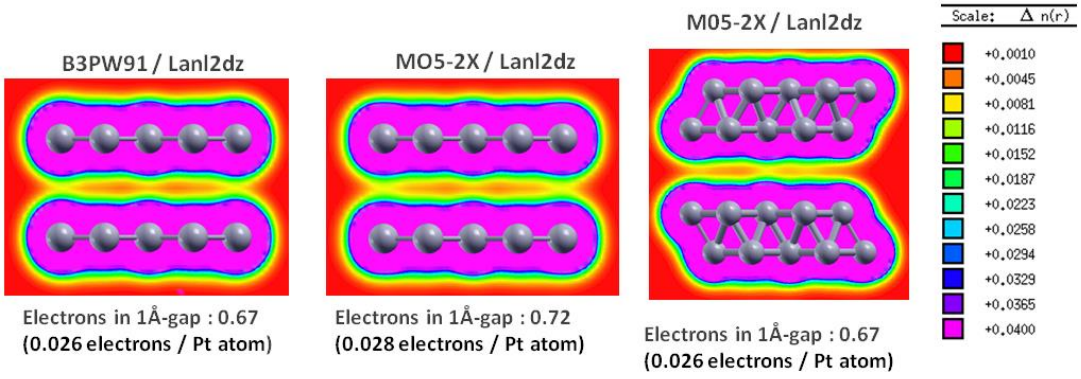

Figure 5.4 Electronic density plots of systems studied using DFT-hybrid methods, for a surface-surface separation of 5 Å. The multiplicity employed with the B3PW91 method was nine, while the one employed with the M05-2X method was five

The agreement between the DFT and hybrid-DFT methods is indicative that the electronic distribution found in the gap between surfaces is not a result of the approaches and approximations taken in pure DFT methods. However, to further confirm these results, the electronic densities were also calculated using post HF correlated methods. These results are especially important when comparing with our previous calculations because we are working with transition metals. This type of materials possesses nearly degenerated electronic distributions and DFT-based methods (both LSDA and GGA) may cause excessively delocalized electronic distributions.[38] Therefore, comparisons with HF correlated methods would eliminate the possibility of electronic densities in the gap between periodic surfaces being a result of unphysical artifacts of the method employed.

Figure 5.5 shows the plots of the electronic density distributions of the systems, calculated using the MP2 (with model shown in Figure 5.2.b) and CCSD(T) methods (with the model shown in Figure 5.2.a). The number of electrons per platinum atom found in the 1Å-gap between the surfaces using the MP2 method, is practically the same as the ones found using DFT-GGA plane-wave based methods and hybrid-DFT (0.026 electrons per platinum-atom), and interestingly, this number is slightly larger using the CCSD(T) method (0.029 electrons per platinum-atom). The latter method is considered as one of the best descriptors of medium and long-range electron correlations. Thus, we are confident that the presence of electrons in the gap between metallic surfaces separated at small distances (4-7 Å) is well described with DFT-GGA methods, and such density is not significantly influenced by the computational method/basis-set employed.

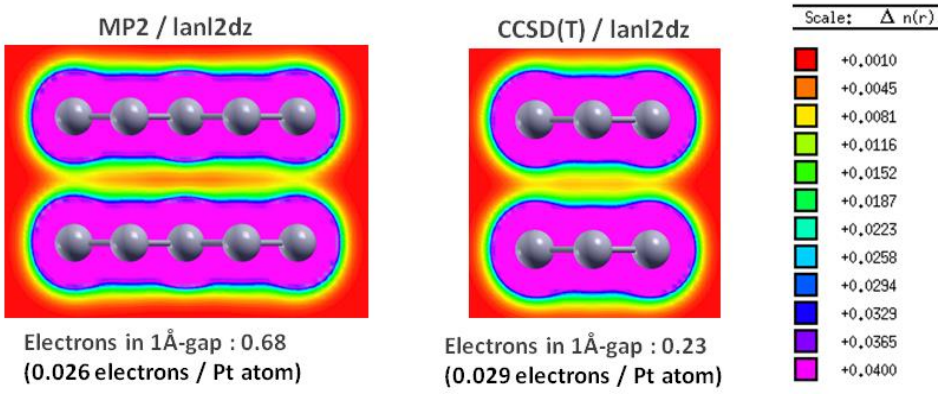

Figure 5.5 Electronic density plots of systems studied using correlated post-HF methods, for a surface-surface separation of 5Å. The multiplicity employed in both cases was five

The number of electrons in the gap of a silver model equivalent to the one of Figure 5.2.b was also calculated using MP2/LANL2DZ and a multiplicity of 2. The results indicate the presence of 0.027 electrons per silver atom in the gap of this system. This result is in agreement with previous calculations showing similar electronic densities inside nanopores formed by silver overlayers and those calculated for pure platinum at similar separations,[25] and also with the values reported in Table 5.1 Calculated layer-layer separation *l*, for the different metal-slabs, and number of electrons in the 1Å-gap for H equal to 1.5l, 2.25l, 3l, and 5l (0.016 electrons/Ag-atom for H=5.42 and 0.168 electrons/Ag-atom for H=3.62).

5.5.Conclusions

A significant presence of electrons is found in the gap between metallic surfaces when the surface-surface separation is between 4-7 Å; such electrons play an important role when interacting with molecules inside the pore formed by the surfaces. Some of these effects include changes in magnetization behavior, induced polymerization of molecules, and reduction in activation barriers for dissociation discussed in our previous reports. In the first part of this work, the energetic state of the electrons present in the gap between

metallic surfaces was studied by calculating the electronic DOS of different metal-nanopores; including iridium, rhodium, nickel, cobalt, copper, and gold. The calculations were performed at fixed surface-surface separations, corresponding to 1.5*l*, 2.25*l*, 3*l*, and 5*l*, where *l* represents the layer-layer separation for the fcc-(111) plane of each specific system. A critical surface-surface separation was found in every case, corresponding to 3*l*. Below this critical distance, electronic states in the gap region between the surfaces are below the Fermi energy of the system and therefore are occupied. Further decreases in the surface-surface separation result in the presence of higher populated electronic levels below the Fermi energy for the gap-region of the system; in agreement with higher electronic densities found for smaller surface-surface separations. Another interesting result derived from the calculated DOS is the specific energies of the electrons in the gap. In all the cases, for surface-surface separations between 4-7 Å, these energies are within 5 eV from the Fermi energy of the system.

Our results have important implications for the design of metallic nanopores as active catalysts for specific reactions. Firstly, they allow designing the nanopores with desired electronic densities between the metallic surfaces, by changing the surface-surface separation (pore length) and they also permit to *choose* the energy of the electrons in the gap-region by choosing the metal forming the nanopore. Energy coupling between electrons and molecular orbitals is required for charge transfers to be effective. Therefore, knowing in advance the energy of electrons in the gap region may allow more effective design of the catalysts for interaction with specific molecules.

In the second part of this work we studied the effect of the computational method on the calculated electronic density between metallic surfaces. Finite layers composed of 4 and 13 platinum atoms were employed. Results using the DFT-based, GGA-RPBE are compared with the ones obtained using DFT-hybrid: B3PW91 and M05-2X; and HF-correlated methods: MP2 and CCSD (T). It is found that the number of electrons calculated in the gap per platinum atom is very similar in all the cases. Hybrid-methods

offer some advantages over GGA-RPBE regarding electron correlation as they mix in with the Hartree-Fock exchange, allowing an explicit description of the densities and their gradients through orbital dependent expressions. However, transition metals possess nearly degenerated electronic distributions and DFT-based methods may cause excessively delocalized electronic distributions. Therefore, the agreement with HF-correlated methods reduces the possibility of electronic densities in the gap between periodic surfaces being a result of unphysical artifacts of the method employed. We are confident that the presence of electrons in the gap between metallic surfaces separated at small distances (4-7 Å) is well described with DFT-GGA methods, and we show that such density is not significantly influenced by the computational method/basis-set employed.

6. SMALL-MOLECULE ACTIVATION DRIVEN BY CONFINEMENT EFFECTS

6.1.Summary

Electron-rich enviroments, created by close interaction of metallic nanostructures at subnanometer separations, have been found to facilitate molecular dissociation of simple diatomic molecules. Electrons in these regions have energies close to the Fermi energy of the metallic structures forming the electron-rich environment, which can be used to tune their energy for specific interactions with the LUMO of molecules of interest. In this work, electron-rich regions are incorporated into a nanopillared-graphene (NPG) structure by decorating the material with Pt_{22} nanoparticles. Regions with finite electronic densities are created in the confined space between Pt and carbon nanotubes (CNTs). In the first part of this work, the reactivity of these regions is evaluated by comparing the bond strength of O_2, CO, and N_2 adsorbed on Pt_{22} in their presence, with that of the molecules adsorbed without neighboring electron-rich regions. Results show larger transferences of charges to the molecules adsorbed in the presence of these environments. Additional charges transferred to these molecules will go their LUMO anti-bonding orbitals, weakening their molecular bonds and facilitating their dissociation. In the second part of the work, the dissociation of O_2 and CH_4 molecules is investigated in the proposed Pt_{22}/NPG structure at different (T, P) conditions, and compared to that in a mesoporous Pt_{26}/Graphite system (no electron-rich regions are present in this system). It was found that electron-rich environments have a clear effect on the reactivity of the material. In the case of O_2, these regions either increase the range of charges being transferred to adsorbed O_2 molecules increasing bond-length oscillations that facilitate the molecular dissociation, or they may increase the amount of charges transferred to adsorbed molecules debilitating their molecular bond. In the case of methane the electron-rich regions does not interact with the molecular LUMO due to

the larger barrier between the Fermi energy of the system and the LUMO orbital of CH_4. However, the *confined* nature of the electron-rich environment in Pt_{22}/NPG may also increase the reactivity of the material due to a geometric effect related to good dispersion of Pt_{22} nanoparticles in NPG and an increased frequency of interaction between catalysts and molecules.

6.2.Introduction

Finite electronic densities can be found between two closely interacting metallic nanostructures, due to migration of some of the conduction electrons to the interparticle region.[21-30] The effect of this electron-rich environment on the catalytic activity of transition metals have been studied in previous works by using two metallic thin films separated at distances between 4-7 Å.[21-23] Results show that the dissociation of simple diatomic molecules is facilitated when taking place between the two metallic thin films, compared to those taking place on single surfaces. The main reason for this difference is the higher charge transferred to adsorbed molecules during their dissociation in the former case, which debilitates molecular bonds and facilitates bond-breaking processes. As a result, a direct relationship exists between the additional charge transferred to molecules and the decrease found in activation barriers.[22] Additionally, the energies of the electrons in the gap region are found to depend on the Fermi level (E_F) of the specific metal forming the pore, and they are expected to be within 5 eV of E_F.[23] Consequently, electronic coupling between electrons in the gap and the dissociating molecule may be tuned by changing the materials from which electrons are migrating.

Given the catalytic enhancement promoted by electron-rich environments, it is of special interest to use them as building blocks and incorporate them into suitable three-dimensional nanostructures. In this way, new catalytic materials with enhanced reactivity towards specific reactions may be obtained. The main requirements that a porous nanostructure may fulfill in order to be considered as a scaffold for the incorporation of these regions, are good stability, high surface area, and facile tailoring

of pore sizes. One interesting three-dimensional material satisfying all of these conditions is Nanopillared Graphene (NPG), a novel nanostructure composed of parallel graphene layers connected by vertically aligned carbon nanotubes (CNTs).[152] Graphene and CNTs have very similar crystal structures and are covalently bonded in this material, which gives NPG the required stability.[153,154] Also, experimental reports have measured high BET specific surface areas for these nanostructures (up to 2600 m^2/g),[153] comparable to the theoretical value for graphene and open-ended CNTs (2630 m^2/g).[155] Furthermore, the length of CNTs, and the inter-tube distances may be easily tuned by changing variables during the synthesis process. For chemical vapor deposition based synthesis, the precursor gas employed, deposition time, and catalyst nanoparticle diameter, influence the growth rate and spacing of CNTs on the material.[154,156,157] NPG structures have been mainly proposed for applications related to hydrogen storage,[152] supercapacitors,[157,158] and nanoelectronics.[159] N-doped NPG has been assessed as an electrocatalyst for the oxygen reduction reaction in fuel cells,[160,161] and NPG structures decorated with metallic nanoparticles have been proposed for magnetic drug delivery applications,[162] and as field emission devices.[163]

In this work, a Pt-decorated NPG structure exhibiting electron-rich regions is proposed as a nanostructured catalyst for the dissociation of molecules in gas phase. Electron-rich regions are present in confined spaces formed by two nanostructures interacting at separations between 4-7 Å.[21-30] Therefore, nanopores with sizes between 4-7 Å must be present in our proposed nanocatalyst. Other ordered carbon materials decorated with metallic nanoparticles have been proposed in the past as electrocatalysts in fuel cell reactions. For example, ordered mesoporous carbon decorated with Pt and Pt-Ru nanoparticles have been tested as electrocatalysts for methanol oxidation, showing enhanced electrochemical performance in comparison to commercial catalysts.[164-166] However, average pore sizes in those carbon-based catalysts are in the order of tens of nanometers. The novelty of our work is based in the incorporation of electron-rich regions into the metal/carbon nanostructure. Such confined regions guarantee the

presence of electrons in the gap, and as mentioned above, the interaction between these electrons and gas-phase adsorbates results in the weakening of molecular bonds and an enhancement of the reactivity of the material.

In the first part of this work, a suitable NPG structure decorated with Pt-nanoclusters and exhibiting electron-rich regions is proposed. Subsequently, enhancements given by electron rich environments to the Pt-decorated NPG structure are investigated by evaluating the effect of these confined regions on bond strengths of diatomic molecules. Finally, the dissociation of oxygen and methane molecules on Pt-decorated NPG is evaluated using AIMD simulations. In this way, enhancements on the reactivity, given by the presence of electron-rich regions, can be directly observed at different temperature/pressure conditions.

6.3.Computational and System Details

6.3.1. Metal-Decorated NPG Structure

The NPG structure was built following the procedure described by Dimitrakakis et al.[152] A 6x10 graphene sheet was employed along with a (6, 6) CNT that were subsequently allow to bond covalently during a DFT optimization (Figure 6.1). In order to decorate the resulting NPG structure with Pt nanoparticles, two different approaches were taken. In the first one, two Pt_{13} clusters were adsorbed onto the CNT, with an initial separation of 6.5 Å between their periodic images (Figure 6.2). In this way, the metallic clusters interacting with each other at distances between 4-7 Å, resemble the interacting thin films studied earlier. In the second approach, one Pt_{22} cluster was adsorbed onto the structure with an initial separation of 5.6 Å from the CNT periodic image (Figure 6.3). In this case, the electron-rich environment is expected to be formed through the interaction between metallic clusters and carbon nanotubes (CNTs), at distances between 4-7 Å.

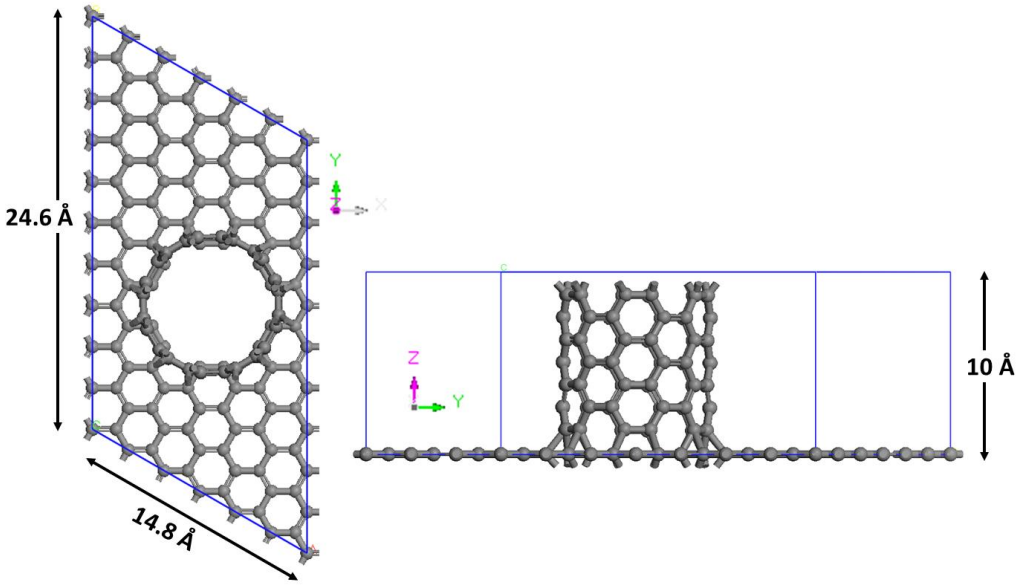

Figure 6.1 Unit cell of The NPG structure built following the procedure described by Dimitrakakis et al. Left: top view. Right: lateral view

CNTs are formed by rolling up graphene layers to form a tubular structure. Carbon atoms in graphene are covalently bonded to other carbons through sp^2 σ-bonds, for which each atom contributes with three electrons. The fourth electron is in the p_z orbital, which extends vertically above and below the plane forming the π bonding and the π* anti-bonding states. Electrons in these unbound states may be susceptible to migration to a gap formed by a metallic surface interacting with graphene at small distances (4-7 Å). Additionally, in the case of CNTs, the curvature of their walls generates a shifting of electrons from the π orbital to the convex outer surface of the tube, which may further facilitate the formation of an electron-rich region between a metallic cluster and the CNT.[167] The electronic density in this region is quantified by calculating the number of electrons in systems shown in Figure 6.7.

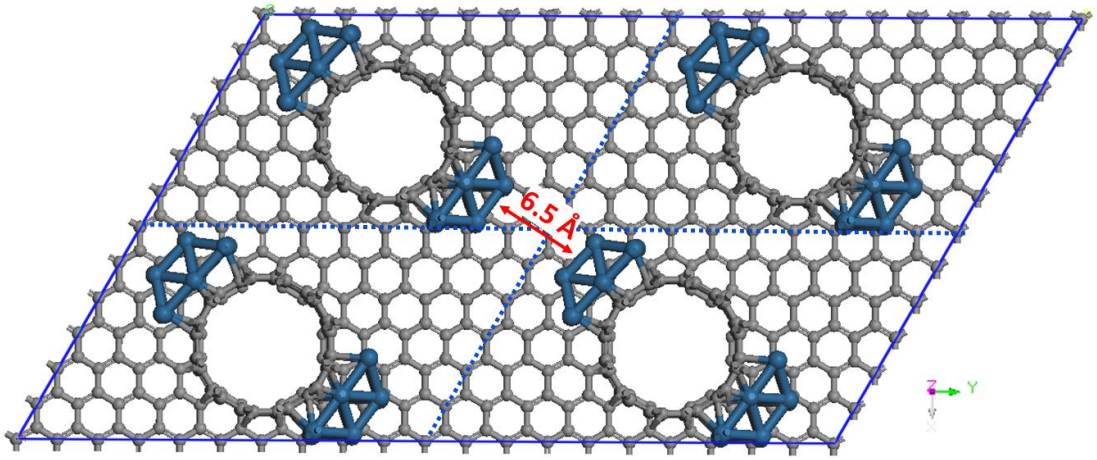

Figure 6.2 Top view of four unit cells of a proposed NPG structure decorated using two Pt_{13} clusters. Carbon atoms are grey and platinum atoms are blue

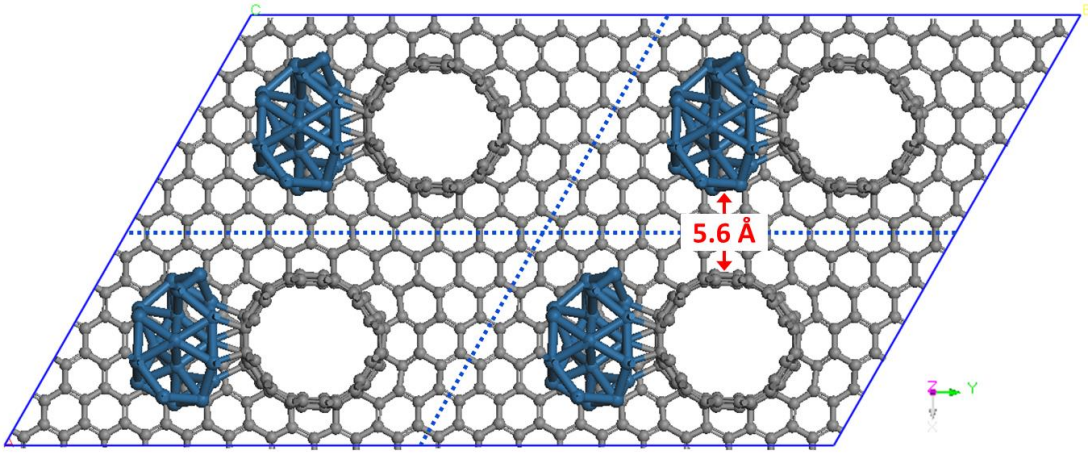

Figure 6.3 Top view of four unit cells of a proposed NPG structure decorated using one Pt_{22} cluster. Carbon atoms are grey and platinum atoms are blue

6.3.2. Evaluating Bond Strength of Diatomic Molecules on Electron-Rich Regions of Metal-Decorated NPG

In order to evaluate the effect that electron-rich regions may have on the reactivity of Pt-decorated NPG, the diatomic molecules O_2, N_2, and CO were adsorbed onto a Pt_{26}-cluster and their bond lengths and charges were evaluated for cases with and without the presence of electron-rich environments. These regions are formed by the interaction between Pt_{26} and graphene at H=4.9 Å and H=15 Å, respectively (Figure 6.4). The O_2 molecule was adsorbed horizontally on a bridge configuration, similar to the t-b-t stable configuration found for the molecule on Pt (111).[168] A similar configuration was adopted in the case of N_2. In the case of CO, the molecule was adsorbed vertically through the C atom on a bridge site of the nanocluster. This configuration was theoretically found as one of the most stables for CO adsorption on Pt (111).[169] The adsorption configuration for each molecule was exactly the same for both separations (H=4.9 Å and H=15 Å). Thus, differences in their bond strength reflect exclusively the effect of the electron-rich environment (present for H=4.9 Å).

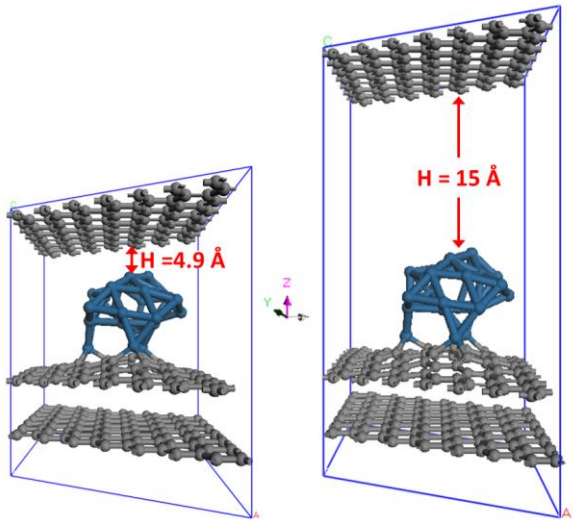

Figure 6.4 Unit cell of a Pt26 cluster interacting with graphene at H=4.9 Å (left) and H=15 Å (right). Carbon atoms are grey and platinum atoms are blue

6.3.3. AIMD Simulations of O_2 on Pt_{22}/NPG

In order to evaluate the influence of electron-rich regions on the dissociation of O_2 on Pt_{22}/NPG at different (T, P) conditions, simulations were performed at (200K, 10 atm.), (250K, 13 atm.), and (298K, 15 atm.). In all cases, the density (ρ) of O_2 in the systems was held constant at 19.5 Kg/m^3 and the resulting pressure was calculated using tables of thermodynamic properties of O_2 at the given (T, ρ) conditions.[170] One oxygen molecule was needed to reproduce this density on the Pt_{22}/NPG system shown in Figure 6.3. Simulations carried out on this system were then compared to those of three oxygen molecules (ρ =19.5 Kg/m^3) interacting with the Pt_{26}/Graphite system shown below (Figure 6.5) at the same (T, P) conditions.

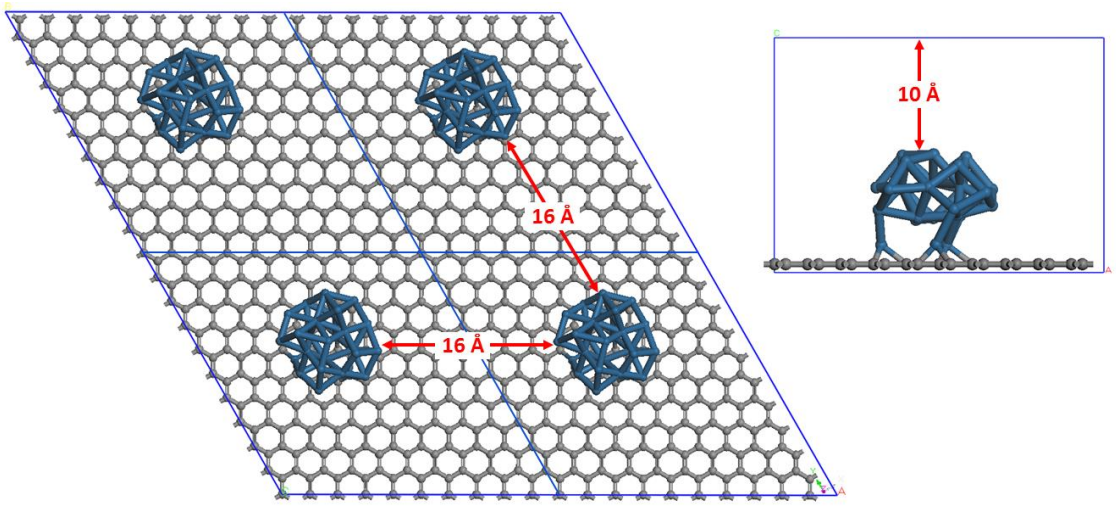

Figure 6.5 Pt26 cluster over a graphene sheet. Left: top view of four unit cells. Right: lateral view of the unit cell. Carbon atoms are grey and platinum atoms are blue

The system in Figure 6.5represents an ordered carbon-based material with larger pore sizes than those in NPG (~ 1nm vs. ~0.56 nm in NPG), and consequently, electron-rich regions are not present. Experimentally, ordered mesoporous carbon materials decorated with platinum nanoparticles (pore sizes between 2-50 nm) may be synthesized by using

mesoporous silicates such as SBA-15.[164-166] Results obtained in this section will enable elucidating the effect of electron-rich regions on the reactivity of platinum-decorated mesoporous carbon materials.

6.3.4. AIMD Simulations of CH_4 on Pt_{22}/NPG

In order to evaluate how electron-rich regions influence the dissociation of CH_4 on Pt_{22}/NPG at different (T, P) conditions, simulations were performed at (1000K, 300 atm.), (1100K, 329 atm.), (1200K, 359 atm.), and (1500K, 449 atm.). In all cases, the density (ρ) of CH_4 in the systems was held constant at 58.6 Kg/m^3 and the resulting pressure was calculated using the ideal gas equation for the given (T, ρ) conditions. Six methane molecules were needed to reproduce this density on the Pt_{22}/NPG system shown in Figure 6.3, while nineteen molecules were needed to reproduce this density on the Pt_{26}/Graphite system shown in Figure 6.5.

Methane is the main component of natural gas, and it is widely used in industry for obtaining hydrogen, higher hydrocarbons, and oxygenates such as alcohols and formaldehydes. However, methane is a highly stable molecule, requiring high energies to activate its C-H bond (104 kcal/mol).[171] Steam reforming is one of the most commonly used processes in industry to activate it obtaining syngas, but this process has to be performed at high temperatures (>1000K) and medium pressures (~30 atm.), which makes it significantly expensive.[172] Hence, it is very important to propose effective strategies to activate methane at milder conditions. Results in this section will help elucidate if methane dehydrogenation on Pt/NPG structures is facilitated, thus reducing (T, P) conditions at which the reaction takes place.

Dehydrogenation of molecules such as methyl-cyclohexane has been carried out successfully using Pt-nanoparticles confined on the pores on ordered SBA-15 templates, and higher catalytic activities were reported for this system compared to those of conventional Pt/SiO_2.[173] Reasons for this are mainly related to the more homogeneous

dispersion of Pt-nanoparticles on the ordered SBA-15 substrate and the restriction in the growth of Pt-nanoparticles inside the pore of SBA-15 (methyl-cyclohexane dehydrogenation is particle-size dependent). Consequently, ordered Pt/NPG catalysts may be good candidates for the dehydrogenation of methane at milder (T, P) conditions.

6.3.5. General Computational Details

Calculations were performed using the Vienna ab initio simulation package VASP,[87,89,90,174,175] with the revised Perdew-Burke-Ernzerhof functional (GGA-rPBE)[176] and the projector augmented wave (PAW) pseudopotentials provided in the VASP databases describing electron-ion interactions.[93,94] The plane wave was expanded up to a cutoff energy of 400 eV. The convergence criteria for ionic relaxation loop and for electronic self-consistent iteration were set to 10^{-3} and 10^{-4} eV respectively. A Gaussian smearing with a width of 0.2 eV was employed and a 4x4x1 k-points Monkhorst–Pack[95] mesh sampling was used in the surface Brillouin zone. AIMD simulations were carried out using the NVT ensemble with a time step of 1 femtosecond. The Nose thermostat was used to control the temperature oscillations during the simulation with a Nose-mass parameter of 0.5, which gives a frequency of oscillation corresponding to 176 time steps. A Γ-point Brillouin zone sampling was applied in this case with a plane wave energy cutoff of 400 eV. All of the systems were allowed to run at least 8 picoseconds. Bader charge analyses were used to perform charge calculations.[99,100] Within this method, the total electronic charge of an atom is approximated by the charge enclosed within the Bader volume defined by zero flux surfaces.

6.4.Results

6.4.1. Metal-Decorated NPG Structure

The Pt-decorated NPG structure proposed in Figure 6.2 is shown in Figure 6.6 after DFT optimization. The two Pt_{13} clusters separated by small distances (<7Å) strongly interact and end up merging during the geometry optimization. In contrast, the structure of the

Pt-decorated NPG proposed in Figure 6.3 is well maintained, and the final separation between the Pt_{22} cluster and the CNT slightly changes from 5.6 to 5.5 Å. Since the structure of the Pt-decorated NPG in Figure 6.3 is stable and small pores are formed between Pt and CNTs (Pore size: 5.5 Å), this nanostructure is chosen as the catalysts to be used in our reactivity studies.

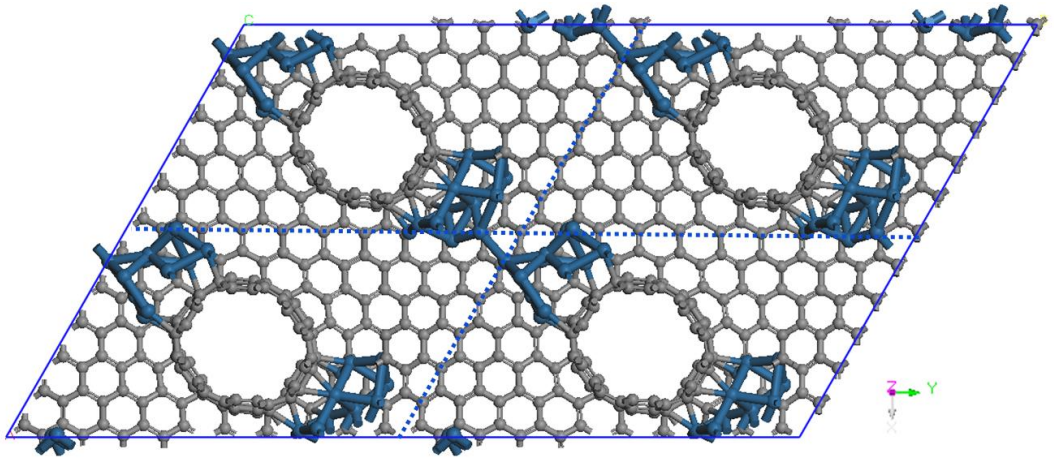

Figure 6.6 Top view of four unit cells of the Pt-decorated NPG structure proposed in Fig. 2 after DFT optimization. Carbon atoms are grey and platinum atoms are blue

In order to quantify the number of electrons in electron-rich regions formed by a Pt-cluster and a graphene sheet, DFT simulations were performed to calculate the number of electrons in a gap formed by a Pt_6 cluster and a graphene layer 5 Å apart (Figure 6.7, left). Additionally, this number was compared to that calculated using two Pt_6 clusters separated by 5 Å (Figure 6.7, center), and to the one calculated using only one Pt_6 cluster over a graphene sheet (Figure 6.7, right). The number of electrons was calculated in a 1Å subgap region (Figure 6.7) defined in the gap between the nanostructures. Figure 6.7 also shows the electronic density in each system after the DFT optimization. The calculated number of electrons in the gap formed by platinum and graphene is just 14% smaller than that in the gap formed by platinum clusters (0.25 vs. 0.29 electrons). Also,

it is interesting to note that the number of electrons in the same gap region for a platinum cluster over graphene (Figure 6.7, right) is very close to zero, confirming that the number of electrons in the gap calculated for systems in the left and center, are a result of tunneling of electrons due to close interaction between the nanostructures at small separations.

Calculations in this section demonstrate that Pt-decorated NPG structures, such as that shown in Figure 6.3, possess electron-rich regions in the small gaps formed by metal-clusters interacting with carbon nanotubes. The effect of electron-rich regions on the reactivity of Pt-decorated NPG structures will be evaluated in the next section.

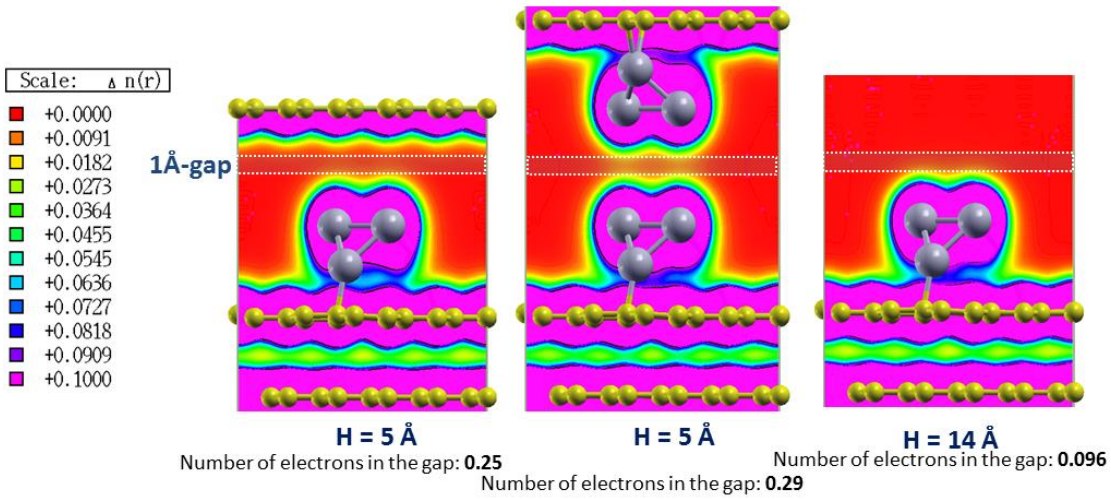

Figure 6.7 Electronic density in a gap formed by a Pt_6 cluster and a graphene layer 5 Å apart (left), two Pt_6 clusters 5 Å apart (center), and one Pt_6 cluster over a graphene sheet (right). Carbon atoms are yellow and platinum atoms are grey

6.4.2. Evaluating Bond Strength of Diatomic Molecules on Electron-Rich Regions of Metal-Decorated NPG

The final configurations of O_2, N_2, and CO molecules adsorbed onto the Pt_{26}/graphite systems in Figure 6.4 are shown in Figure 6.8**.** Bond lengths and charges of molecules in each system are also shown. Charges transferred to molecules in electron-rich regions (H=4.9Å) during adsorption are up to 35% larger compared to those of molecules adsorbed on the cluster with no electron-rich regions (H=15Å). Also, bond-lengths of adsorbed molecules are up to 0.84% longer in electron-rich regions. This reflects weaker molecular bonds resulting from the larger amount of charge transferred to molecules, and smaller barriers expected to be required for their dissociation in electron-rich regions. The lowest unoccupied molecular orbital (LUMO) of O_2, N_2, and CO is an anti-bonding orbital, and its additional filling weakens the molecular bond.[177] In fact, previous calculations on Pt (111) surfaces showed that O_2 molecules receiving 0.11 more electrons during their adsorption in electron-rich environments required 39% less energy to be dissociated than those adsorbed without the presence of electron-rich regions (Activation barrier 0.25 eV smaller). Analogously, CO molecules receiving 0.14 more electrons required 6.4% less energy to be dissociated (Activation barrier 0.27 eV smaller).[22]

In the cases studied in this chapter, O_2 and CO molecules adsorbed on Pt_{26}-clusters in the presence of electron-rich environments received 0.06 and 0.05 more electrons that their counterparts adsorbed on the cluster with no electron-rich environments. These increases in charge correspond to 54 and 36% of those calculated for O_2 and CO on electron-rich Pt (111). Therefore, noticeable reductions in activation barriers are also expected when such molecules are adsorbed on Pt-NPG in the presence of electron-rich regions compared to barriers on Pt-NPG structures with no electron-rich regions present.

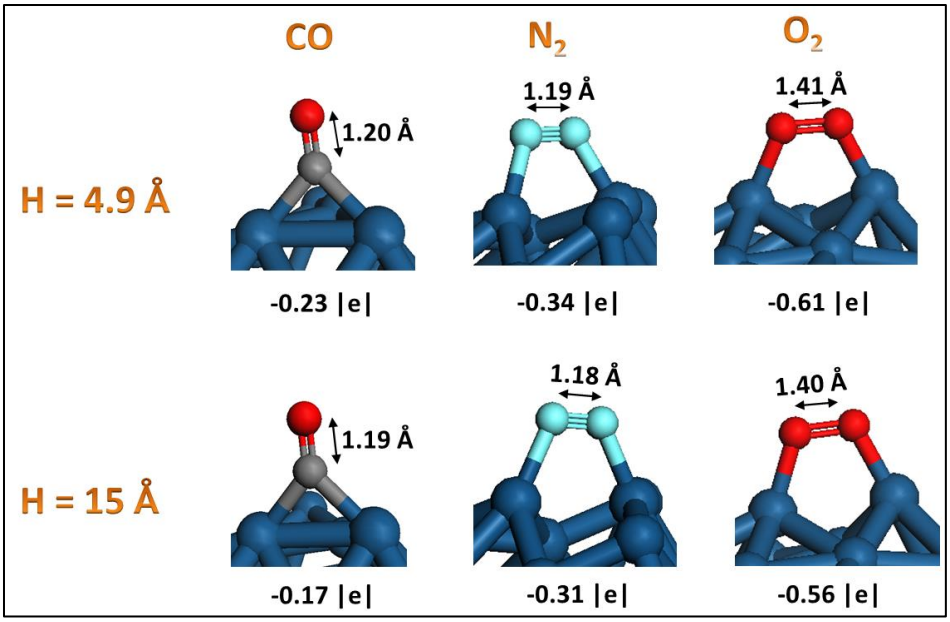

Figure 6.8 Final configurations of O_2, N_2, and CO molecules adsorbed onto the Pt_{26}/graphite systems in Fig. 4. Bond lengths and charges in each case are also shown. Platinum atoms are blue, carbon atoms are grey, nitrogen atoms are light blue, and oxygen atoms are red

It is interesting to note from the charges shown in Figure 6.8 that the amount of electrons transferred to each molecule is not the same. Given the importance of the charge transferred to the molecule during its adsorption on the weakening of its molecular bond and the facilitation of its dissociation, it is vital to understand the origin of such differences. In order to accomplish this, the Fermi level of the Pt_{26}/Graphite system in Figure 6.4 was calculated and compared to the LUMO of the three different molecules studied: O_2, N_2, and CO. Figure 6.9 (left) shows the calculated values, relative to the energy levels of vacuum. An effective coupling between Fermi energy and LUMO is expected to result in better electron transference. Specifically, the difference ($LUMO_{Molecule} - E_{Fermi\text{-}Pt26}$) provides the barrier required for charge transference to the molecule.

In the case of the O_2 molecule, the LUMO lies below the Fermi energy of Pt_{26}/Graphite, which allows for a spontaneous transference of charge from the cluster. In contrast, the LUMO of N_2 and CO is above the Fermi level of Pt_{26}/Graphite, which gives rise to barriers in charge transference corresponding to 2.1 and 2.2 eV, respectively. These results are consistent with the charges calculated for the different molecules adsorbed on Pt_{26}/Graphite at both separations, H=4.9 and H=15 Å (Figure 6.8). Largest amount of charges are transferred to O_2, which has no barrier for the transference of electrons to its LUMO, followed by N_2 (barrier: 2.1 eV), and CO (barrier: 2.2 eV). As mentioned above, the LUMO of these molecules correspond to an anti-bonding orbital, and the filling of such orbital facilitates their dissociation. Figure 6.9 (Right) shows the charges of O_2, N_2, and CO adsorbed on Pt_{26}/Graphite as a function of the barrier ($LUMO_{Molecule} - E_{Fermi\text{-}Pt26}$). It is clear from the graph that smaller ($LUMO_{Molecule} - E_{Fermi\text{-}Pt26}$) differences result is larger amount of charges transferred to adsorbed molecules (more negative molecular charges). The same trend is observed in systems with and without the presence of electron-rich regions (H=4.9 and H=15 Å, respectively). However, the effect of the electron-rich region is an increased amount of electrons being transferred to the molecule.

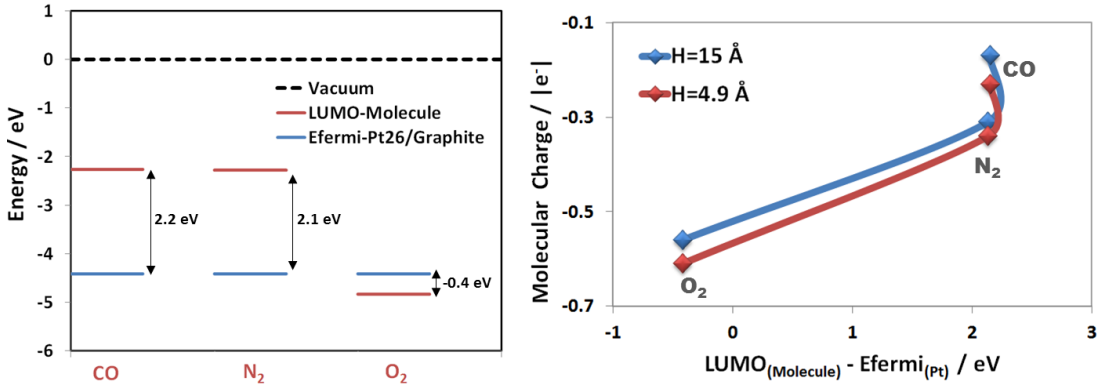

Figure 6.9 Left: Fermi level of the Pt_{26}/Graphite system in Fig. 6.4 compared to the LUMO of O_2, N_2, and CO. Right: charges of O2, N2, and CO molecules adsorbed on Pt_{26}/Graphite as a function of the barrier (LUMO Molecule – E Fermi-Pt26)

These results are important for the design of metal-decorated NPG catalysts with enhanced reactivity toward specific reactions. NPG systems can be decorated with metal clusters whose Fermi Energy effectively couples with the LUMO of molecules of interest (small or negative $LUMO_{Molecule} - E_{Fermi\text{-}Pt26}$ differences). In that way, larger amount of charges can be transferred to LUMO orbitals of molecules, facilitating their dissociation. Additionally, if electron-rich regions are present, the amount of charge being transferred to the molecule of interest is further increased, enhancing the reactivity of the nanostructured material.

6.4.3. AIMD Simulations of O_2 on Pt_{22}/NPG

Figure 6.10(a) shows the O-O bond-length as a function of time for the O_2 molecule interacting with Pt_{22}/NPG at (200K, 10 atm.), (250K, 13 atm.), and (298K, 15 atm.). Time zero represents the time at which the molecule is first adsorbed on the Pt_{22} nanoparticle. In all cases, the initial configuration corresponded to the O_2 molecule in the gap between the Pt_{22}-cluster and the CNT, at approximately 3 Å of the Pt-nanoparticle (Figure 6.10(b)). After adsorption, the O_2 molecule is on a *bridge* site interacting with two platinum atoms, as shown in Figure 6.10(c). As expected, Figure 6.10(a) shows that as the temperature increases the time required to observe dissociation of the adsorbed O_2 molecule decreases. This time corresponds to 710, 370, and 170 femtoseconds at 200, 250, and 298K, respectively.

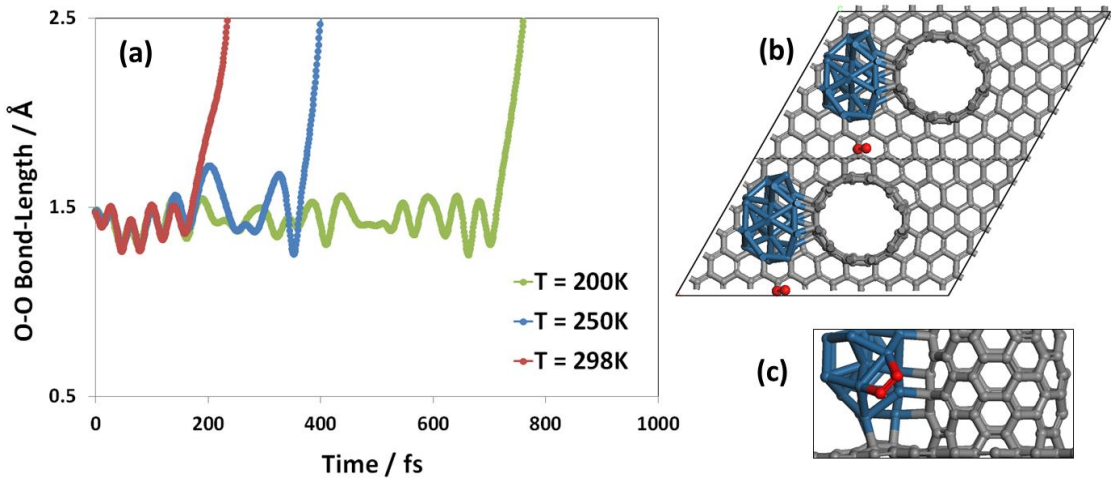

Figure 6.10 (a) O-O bond-length as a function of time for the O_2 molecule interacting with Pt_{22}/NPG at (200K, 10 atm.), (250K, 13 atm.), and (298K, 15 atm.). Time zero represents the time at which the molecule is first adsorbed on the Pt22 nanoparticle (b) Top view of two unit cells of the initial configuration of the O_2 molecule in the Pt_{22}/NPG system (c) bridge-site adsorption of O_2. Platinum atoms are blue, carbon atoms are grey, and oxygen atoms are red

Adsorption of O_2 molecules at the same (T, P) conditions were also studied on the Pt_{26}/Graphite system in Figure 6.5. After 8 picoseconds of AIMD simulations all of the oxygen molecules get adsorbed onto the Pt_{26} cluster. However, none of the molecules dissociated at any of the conditions studied. Figure 6.11 shows the final configuration of the systems at (200K, 10 atm.), (250K, 13 atm.), and (298K, 15 atm.).

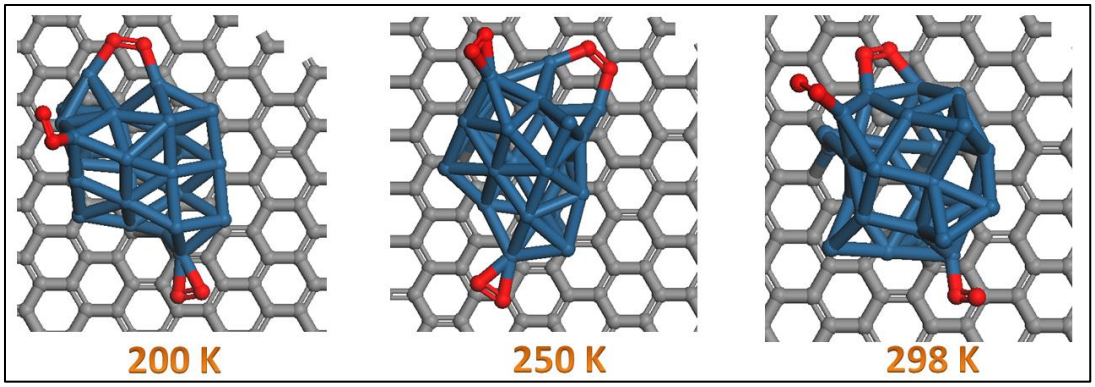

Figure 6.11 Final configuration of O_2 molecules on the Pt_{26}/Graphite systems at (200K, 10 atm.), (250K, 13 atm.), and (298K, 15 atm.). Platinum atoms are blue, carbon atoms are grey, and oxygen atoms are red

In order to understand differences in reactivity between Pt_{22}/NPG and Pt_{26}/Graphite, the O-O bond-lengths of the molecule adsorbed on Pt_{22}/NPG are compared at each (T, P) condition with those of the O_2 molecule adsorbed on the *bridge* configuration on Pt_{26}/Graphite, as a function of time (Figure 6.12). Again, time zero represents the time at which the molecule is first adsorbed on the Pt-nanoparticle (Pt_{22} or Pt_{26}). It is evident that for T=200K and T=250K, the bond-length of the molecule oscillates in a wider range of values when adsorbed on the Pt_{22}/NPG system (red-line). For example, the bond-length of the molecule adsorbed on Pt_{22}/NPG at 200K, and 250K varies between 1.25-1.56 Å and 1.25-1.72 Å, respectively, compared to 1.34-1.50 Å and 1.26-1.61 Å in the Pt_{26}/Graphite system. These longer O-O oscillations may have facilitated O_2 dissociation in Pt_{22}/NPG at 200K and 250K compared to Pt_{26}/Graphite. However, at 298K the O-O bond length oscillates in the same range, 1.26 and 1.80 Å, in both systems and dissociation is only observed on Pt_{22}/NPG. Given that electron-rich regions are present in the Pt_{22}/NPG system, electronic charges of O_2 molecules adsorbed on this system may be different to those adsorbed on Pt_{26}/Graphite (no electron-rich regions). As shown in the previous section, the presence of electron-rich regions may result in

larger charges being transferred to adsorbed molecules, which debilitates their molecular bond and facilitates their dissociation.

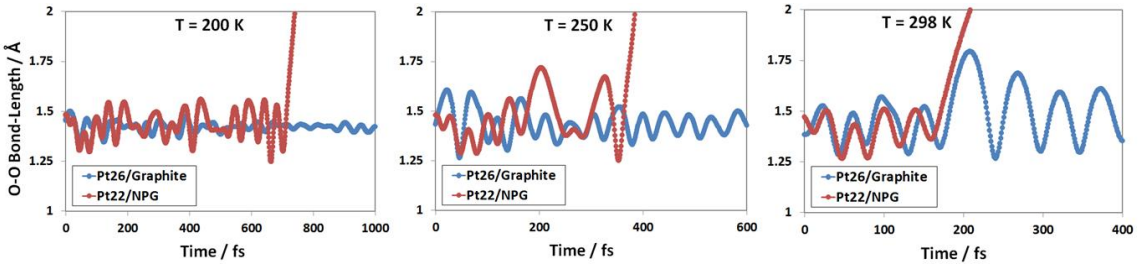

Figure 6.12 O-O bond-lengths of the O_2 molecule adsorbed on Pt_{22}/NPG at different (T, P) conditions. Time zero represents the time at which the molecule is first adsorbed on the Pt-nanoparticle

At 298K, no bond dissociation is observed after 8 picoseconds of simulation for the Pt_{26}/Graphite system. Charges were calculated, as a function of the molecular bond length, for O_2 in Pt_{22}/NPG and Pt_{26}/Graphite at the different (T, P) conditions (Fig. 13). A direct relationship is found between the molecular bond length and the molecular charge, the longer the O-O bond the more negative the molecular charge. In the case of T=200K, data for the O_2 molecule in Pt_{22}/NPG fall under the same *fitting line* than that for the O_2 molecule in Pt_{26}/Graphite (Figure 6.13, left). Thus, molecules with a given O-O bond length possess similar charges in both systems. This suggests that dissociation at 200K is only observed in Pt_{22}/NPG due to the *wider* range of charges being transferred to the adsorbed molecule in this system (-0.44|e^-| to -0.75|e^-|, compared to -0.53|e^-| to -0.69|e^-| in Pt_{26}/Graphite), which leads to longer O-O bond length oscillations that facilitate the breaking of the molecular bond. The range of charges being transferred in the Pt_{22}/NPG system may be wider due to the neighboring electron-rich region interacting with the adsorbed molecule. Electrons in such region are expected to have energies close to the Fermi energy of Pt_{22}/NPG,[3] and as showed in the previous section,

the LUMO of O_2 lies below the Fermi energy of a Pt/Graphite system, which allows for a spontaneous transference of charge from the electron-rich region to the molecule.

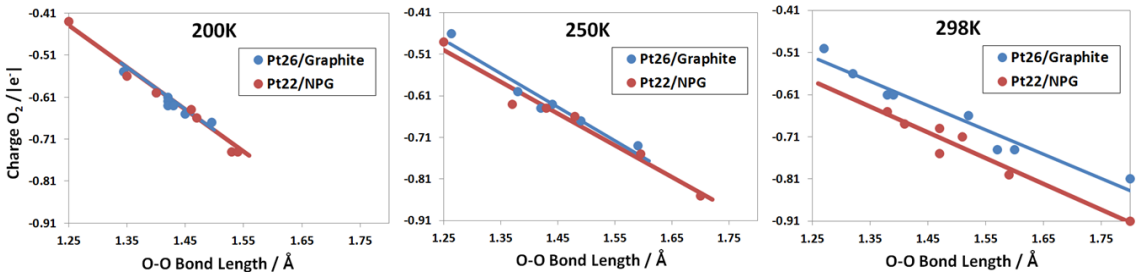

Figure 6.13 O_2 Charges as a function of the molecular bond length, for O_2 in Pt_{22}/NPG and Pt_{26}/Graphite at the different (T, P) conditions. The fitting line extends over the range in which bond lengths oscillates in each system

At T=250K, the range of charges being transferred to the adsorbed molecule in Pt_{22}/NPG is, again, slightly larger (-0.5|e| to -0.86|e|, compared to -0.48|e| to -0.78|e| in Pt_{26}/Graphite), causing longer O-O bond length oscillations. But additionally, the *fitting line* for data corresponding to O_2 in Pt_{22}/NPG (red line in Figure 6.13, center) is slightly lower than the *fitting line* for data corresponding to O_2 in Pt_{26}/Graphite (blue line in Figure 6.13, center). This means that, on average, O_2 molecules with a given O-O bond length are slightly more negative when adsorbed on Pt_{22}/NPG (about 0.02|e^-| more negative). The more negative charge is also believed to be related to the presence of electron-rich regions in the Pt_{22}/NPG system. As the temperature increases, migration of electrons to the confined region between the Pt-cluster and the CNT may be facilitated, which results in a larger electronic density interacting with the adsorbed O_2 molecule. Consequently, at this *intermediate* temperature (T=250K) the effect of electron-rich regions on the reactivity of Pt_{22}/NPG is twofold, first, there is a wider range of charges being transferred to the O_2 molecule that results in longer O-O bond length oscillations than those of the molecule adsorbed on Pt_{26}/Graphite. Second, the presence of electron-

rich regions in Pt_{22}/NPG helps transferring slightly larger amount of charges to adsorbed O_2 molecules for a given O-O bond length. The combination of these two factors results in an enhanced reactivity of Pt_{22}/NPG and dissociation of the O_2 molecule within a few hundred femtoseconds of adsorption. No dissociation is observed for molecules adsorbed on Pt_{26}/Graphite after eight picoseconds of AIMD simulations at the same (T, P) conditions.

Finally, at 298K the O-O oscillations are very similar in both systems, Pt_{22}/NPG and Pt_{26}/Graphite, as can be observed in Figure 6.12, right (~1.26 to 1.80Å). However, the O_2 molecule adsorbed on Pt_{22}/NPG is more negative, on average (about $0.07|e^-|$), than that adsorbed on Pt_{26}/Graphite, for the same O-O bond length (Figure 6.13, right). Therefore, in this particular case (T=298K), the presence of electron-rich regions in the system helps increasing the amount of charge transferred to adsorbed molecules compared to that transferred in the absence of these regions, which helps weakening the O-O bond and allows dissociating the O_2 molecule after about 180 femtoseconds of adsorption. Again, no dissociation is observed for molecules adsorbed on Pt_{26}/Graphite after eight picoseconds of AIMD simulations at the same (T, P) conditions.

In summary, there is a clear effect of electron-rich regions on the reactivity of platinum-decorated mesoporous carbon, towards the dissociation of O_2. When electron-rich regions are present at *low* and *intermediate* temperatures (200-250K), a wider range of charges is transferred to adsorbed molecules, which generates longer bond-length oscillations that facilitate the molecular dissociation. As the temperature increases (298K), the effect of bond-length oscillations is less important as this becomes similar to that observed in systems with no electron-rich regions (Figure 6.12). However, increasing temperatures may facilitate a larger migration of electrons to the confined region between the Pt-cluster and the CNT, which leads to larger electronic densities in the neighboring electron-rich region. As a result, adsorbed molecules interacting with it are, on average, more negative (Figure 6.13, center and right). As discussed in section

6.4.2, the LUMO of O_2 molecules is an anti-bonding orbital, and its filling facilitates the breaking of the O-O bond.

6.4.4. AIMD Simulations of CH_4 on Pt_{22}/NPG

Methane molecules interacting with Pt_{22}/NPG were found to adsorb on the Pt_{22} cluster after 14170 fs, 9533 fs, 0.44 fs, and 0.38 fs at (1000K, 300 atm.), (1100K, 329 atm.), (1200K, 359 atm.), and (1500K, 449 atm.), respectively. In all cases, the same initial configuration was used for the AIMD simulations, as shown in Figure 6.14, left. The first dehydrogenation takes place almost immediately upon adsorption of the molecule on the Pt-cluster. In every case, the dehydrogenation takes place through the formation of Pt-C and Pt-H bonds, which eventually leads to the breaking of a C-H bond in the methane molecule (Figure 6.14, right). Similar mechanisms have been previously proposed for the catalytic dehydrogenation of alkanes using transition metals.[178] The dehydrogenation reaction takes place through a *three-centered transition state* in which the metal atom (M) inserts itself into a C-H bond of the alkane, forming M-H and M-C bonds. The strength of the M-H and M-C bonds combined exceeds that of the C-H bond in the alkane, making the dehydrogenation process thermodynamically favorable.[178]

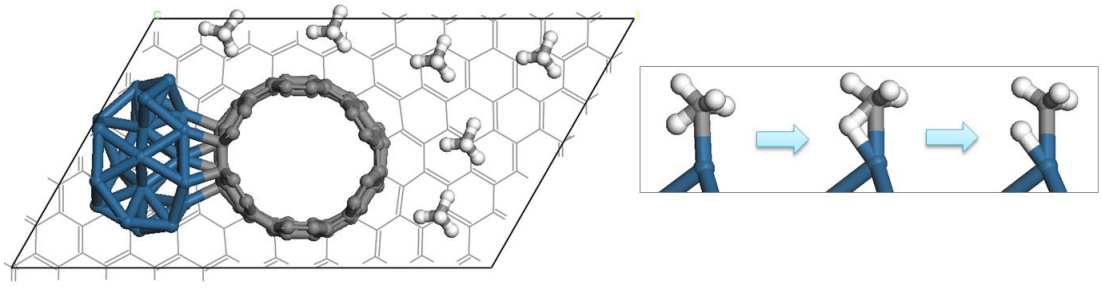

Figure 6.14 Left: top view of unit cell representing the initial configuration for the AIMD simulations of CH_4 on Pt_{22}/NPG. Right: dehydrogenation mechanism. Platinum atoms are blue, carbon atoms are grey, and hydrogen atoms are white

Methane molecules interacting with Pt_{26}/Graphite (Figure 6.5**)** at the same (T, P) conditions were also studied through AIMD simulations. The same initial configuration was used in every case as shown in Figure 6.15. No adsorption of CH_4 molecules on the Pt-cluster was observed after 14000 femtoseconds of simulation at (1200K, 359 atm.) and (1500K, 449 atm.). However, adsorption and dehydrogenation of one methane molecule was observed at (1100K, 329 atm.) after about 12500 femtoseconds. The dehydrogenation mechanism observed in this case was equivalent to that observed in the Pt_{22}/NPG system (Figure 6.14, right).

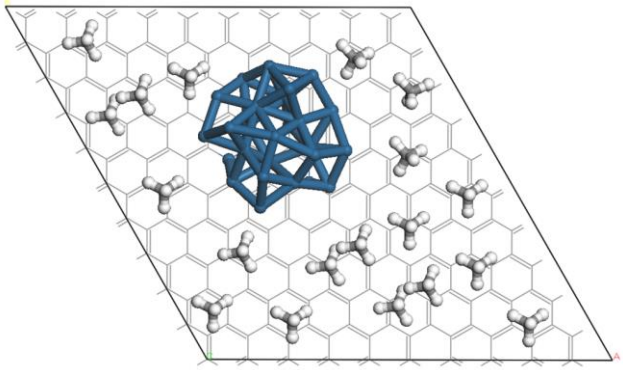

Figure 6.15 Top view of the unit cell representing the initial configuration for the AIMD simulations of CH_4 on Pt_{26}/Graphite

In order to investigate possible differences in the dehydrogenation process taking place on Pt_{22}/NPG vs. that taking place on Pt_{26}/Graphite, the C-H bond-length of the adsorbed molecule was plotted as a function of time for each system at 1100 K (Figure 6.16, left). Time zero represents the time at which the methane *adsorbs* on the Pt-cluster (Pt_{22} or Pt_{26}). In both cases, the C-H bond length at this time corresponds to 1.13 Å. The C-H bond length of the methane molecule adsorbed on Pt_{22}/NPG increases slightly more rapidly than that of the molecule adsorbed on Pt_{26}/Graphite between C-H = 1.13 Å and 1.30 Å (approximately length at which the C-H bond breaks). Data in Figure 6.16, left,

was fitted taking into account the time needed for the C-H bond to reach 1.30 Å after adsorption (5 femtoseconds in the case of Pt_{22}/NPG and 9 femtoseconds in the case of Pt_{26}/Graphite), and a slightly larger slope corresponding to 0.035 Å/fs, is found in the case of Pt_{22}/NPG. However, differences calculated in Figure 6.16 are not significant, as the difference between dissociation times after adsorption is only 4 femtoseconds among the two systems. Charges of the methane molecules during dissociation were also calculated for three different C-H bond lengths and are plotted in Figure 6.16, right. In both cases (Pt_{22}/NPG and Pt_{26}/Graphite), the charge of the adsorbed molecule is positive and around 0.1|e^-|. Thus, significant transference of charge from the Pt-cluster to the CH_4 molecule is not believed to happen during its dehydrogenation. The barrier ($LUMO_{Molecule} - E_{Fermi\text{-}Pt26}$) calculated for transference of charge to CH_4 corresponds to approximately 4.4 eV, which is a significantly high barrier that may explain the inability of the system to transfer electrons to the LUMO of methane molecules.

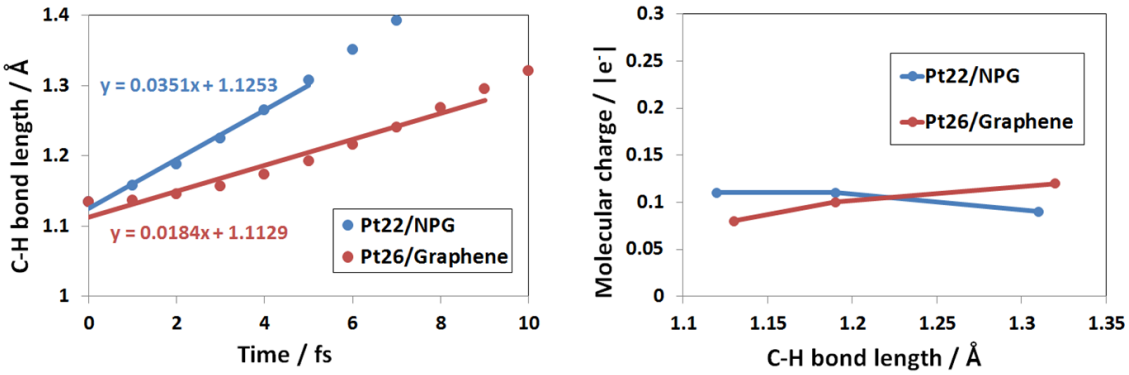

Figure 6.16 Left: C-H bond-length of the adsorbed CH4 molecule as a function of time for each system at 1100 K. The fitting line extends up to C-H = 1.3Å, and time zero represents the time at which the methane adsorbs on the Pt-cluster. Right: charge of the methane

Even though electron-rich regions do not significantly affect the charge density of molecules with substantial ($LUMO_{Molecule} - E_{Fermi}$) barriers, the *confined* nature of these

regions may have a geometric effect on the reactivity of the system. For example, comparison of times required to observe molecular adsorption on Pt_{22}/NPG and Pt_{26}/Graphite suggests that smaller times are required to observe molecular adsorption on Pt_{22}/NPG. As discussed above, CH_4 is found to adsorb on the Pt_{22}/NPG after 14170 fs, 9533 fs, 0.44 fs, and 0.38 fs at (1000K, 300 atm.), (1100K, 329 atm.), (1200K, 359 atm.), and (1500K, 449 atm.), respectively. Meanwhile, adsorption on Pt_{26}/Graphite at (1200K, 359 atm.), and (1500K, 449 atm.) has not been observed after 14000 femtoseconds of AIMD simulations, and that at (1100K, 329 atm.) was observed after approximately 12500 femtoseconds. Dehydrogenation of molecules such as methyl-cyclohexane has been carried out with higher catalytic activities than conventional Pt/SiO_2 when the Pt-nanoparticles are confined on the pores on ordered SBA-15 templates.[173] One of the reasons is the better dispersion of Pt-nanoparticles found inside the ordered SBA-15 template. Additionally, different authors have found that zeolites structure and pore-size influences reaction rates inside the zeolite.[128] Thus, NPG structures as the one proposed on this work may enhance the reactivity of the metal clusters decorating the structure, even when the electron-rich regions do not interact with the molecules of interest, due to the good dispersion of Pt-clusters on the material and to small pore sizes that may increase the frequency of interaction between catalyst and molecules.

6.5.Conclusions

A Pt/NPG structure exhibiting electron-rich regions was proposed as a nanostructured catalyst for the dissociation of molecules in gas phase. Electron-rich regions are formed in this system through close interaction between the Pt-cluster and CNTs (separation ~ 5.5Å). In the first part of this work, O_2, CO, and N_2 molecules were adsorbed on a Pt_{26} cluster with and without the presence of electron-rich regions. Charges transferred to molecules in electron-rich regions during adsorption are up to 35% larger compared to those of molecules adsorbed on the cluster with no presence of electron-rich regions.

Also, bond-lengths of adsorbed molecules are up to 0.84% longer. Therefore, molecules in electron-rich regions exhibit weaker molecular bonds, and smaller barriers are expected to be required for their dissociation. It was also found that the difference ($LUMO_{Molecule} - E_{Fermi\text{-}Catalyst}$) provides the barrier required for charge transference to the molecule. Consequently, it is possible to selectively enhance catalytic reactions by efficiently coupling the Fermi energy of the catalyst (by changing the metal particle decorating the NPG) with the LUMO orbital of the molecule of interest. In that way, larger amount of charges can be transferred to LUMO antibonding orbitals of molecules, weakening their molecular bonds.

In the second part of this work, AIMD simulations of O_2 molecules interacting with the proposed Pt/NPG catalysts were performed. These simulations were compared to those of O_2 molecules interacting with a Pt_{26}/Graphite system at the same (T, P) conditions. Pt_{26}/Graphite represents an ordered carbon-based material with larger pore sizes than those in NPG (~ 1nm vs. ~0.56 nm in NPG), and consequently, it does not possess electron-rich regions. A clear effect of electron-rich regions on the reactivity of platinum-decorated mesoporous carbon was observed. First, it may help by allowing a wider range of electrons being transferred to adsorbed molecules, which generates longer bond-length oscillations that facilitate the molecular dissociation. Additionally, at higher temperatures, larger migration of electrons to the confined region between the Pt-cluster and the CNT may be possible, which results in adsorbed molecules with more negative charges. The additional charge goes to the antibonding LUMO of the O_2 molecule, facilitating the breaking of its O-O bond.

Finally, the dehydrogenation of methane was also studied on the proposed Pt/NPG system using AIMD simulations. In this case, the calculated ($LUMO_{Molecule} - E_{Fermi\text{-}Catalyst}$) barrier is significantly high, corresponding to 4.4 eV. As a result, electron-rich regions do not significantly affect the charge density of methane molecules. However, smaller times are required to observe molecular adsorption on Pt_{22}/NPG than on Pt_{26}/Graphite, which may be related to the *confined* nature of the electron-rich regions in

NPG. Ordered Pt/NPG structures as the one proposed on this work may display enhanced reactivity, even when electron-rich regions do not interact with the molecules of interest, due to the good dispersion of Pt-clusters on the material and to small pore sizes that may increase the frequency of interaction between catalysts and molecules.

Therefore, the Pt/NPG catalyst proposed in this work is a good candidate for the efficient dissociation of molecules in gas phase. Its reactivity may be tailored by effectively coupling the energy of electrons in electron-rich regions with that of antibonding orbitals of molecules of interest. Such coupling allows additional transference of electrons to adsorbed molecules, weakening molecular bonds and facilitating molecular dissociations. Additionally, the ordered nature of the catalyst and its small pore size may also have a geometric effect on reactivity even in cases when electron-rich regions do not effectively interact with the LUMO of molecules.

7. CONCLUSIONS AND FUTURE WORK

The present study set out an analysis to explore the influence of electron-rich regions on the reactivity of nanostructured materials. Novel nanostructures displaying enhanced reactivities may help alleviate energy costs associated with important industrial processes; a very important task given that 20% of the worldwide economy depends on catalysis. Recent progress in nanotechnology has allowed for the efficient customization of the shape, structure, and composition of catalysts. Nonetheless, novel approaches further improving the reactivity of materials towards specific reactions are still needed.

The *hypothesis* of this work is that reactions taking place in electron-rich environments require lower energy barriers, thus enhancing the reactivity of materials in which they are present. This claim was based on previous findings by different authors who showed that interaction of molecules with electron-rich regions gives rise to interesting phenomena such as conversion of the molecules to radical anions,[27] or pre-activation of molecules helping molecular bond breaking.[32] Chapter three, "Geometric and Electronic Confinement Effects on Catalysis," describes in detail the systematic way in which the hypothesis is proved. Electron-rich regions are built using metallic slit-pores, formed by bringing together two metallic surfaces separated from one another 4.9 Å. Different metallic surfaces are used to build the slit-pores, including Pt, Ir, Rh, Pd, and Ni. Activation barriers for the dissociation of the diatomic molecules CO, NO, N_2, and O_2 are calculated inside the pores (i.e., interacting with the electron-rich region), and on a single surface made of the same transition metal. The interaction of adsorbed molecules with electron-rich regions is found to influence significantly the activation barriers required for their dissociation. The calculated activation energies are up to 39% smaller for molecules inside the pores. This change is related to larger amount of charges transferred to those molecules compared to the ones adsorbed on single surfaces (up to

78% larger). Since the lowest unoccupied molecular orbitals (LUMO) of CO, NO, N_2, and O_2 are anti-bonding orbitals, their additional filling weakens the molecular bond and facilitates molecular dissociations. Therefore, this systematic study shows that electron-rich environments have the potential to enhance the reactivity of a given material.

Other interesting conclusions gathered from this chapter are that the degree of facilitation given by the electron-rich region (% of reduction of activation energy compared to that calculated on a single surface of the same metal) depends directly on the amount of additional charge transferred to molecules inside the metallic pores, and also on the degree of interaction between the molecule and the top metallic surface forming the slit-pore. The chapter highlighted the importance of understanding these geometric and electronic effects in order to use these regions effectively in a real nanostructured material. Specifically, two questions were defined: (i) how does the local geometry of the slit-pore influence the adsorption energy of molecules inside the pore and their barriers for dissociation? And also, (ii) what is the energy of the electrons found inside the metallic pores i.e., the energy of the electrons in the electron-rich region? Chapter four, "Local surface structure effect on reactivity of molecules confined between metallic surfaces," provides the answer to question (i). In this study, Pt slit pores are used to study the adsorption and dissociation of O_2. One type of pore is built using different stacking planes of defect-free Pt (111) as the top/bottom surfaces forming the slit pore. Other types of Pt pores are built by bringing together two Pt (111) surfaces with step-like defects. It is found that specific surface–surface configurations in the pore (different stacking planes) influence the electronic structure of the surface where the molecule is adsorbed, modifying adsorption strengths inside the pore. In addition, the top layer of the metallic pore may interact electrostatically with the adsorbate with more or less strength depending on their proximity; the stronger the electrostatic interaction, the larger the enhancement of the adsorption strength. However, this interaction may also makes it more difficult for the molecule to move away and therefore dissociate, resulting in higher energy barriers for dissociation. Stronger electrostatic interactions between O_2

and the top Pt-surface were shown to be present in the case of Pt (111) defect free surfaces in which the pore is made of the same stacking plane (top and bottom surfaces). These results show the importance of the geometry of the slit-pore on its reactivity. If a strong molecular adsorption is desired, then a top layer strongly interacting with the adsorbate is convenient. This is made possible, for example, by building the pore using two defect- free Pt (111) surfaces, whereas, if a small barrier for dissociation is preferred, then a weaker interaction between the molecular precursor and the top layer of the gap is more convenient. This can be achieved by using surfaces with step-like defects.

Question (ii) is investigated in chapter five, "Characterization of Electronic States inside Metallic Nanopores". In this chapter, the electronic density of states of several transition metal nanopores are calculated for different pore sizes (i.e., surface−surface separations). Results show the existence of a critical surface−surface separation below which electronic states inside the pore become populated at energies below the Fermi level of the metal, leading to the presence of electrons in the gap between the metallic surfaces. Further reduction in the nanopore size increases the number of states corresponding to the gap, which agrees with the increasingly higher electronic densities found in the gap for smaller surface−surface separations. Additionally, the energy of the electrons in the gap region will generally be within 5 eV of the Fermi energy of the metallic system. The results of this section are very important for the design of electron-rich regions as active sites for specific reactions. First, they allow tuning electronic densities inside the nanopore by changing the surface−surface separation (pore length). Additionally, it is possible to *choose* the energy of the electrons in the gap region by choosing the metal forming the nanopore. Energy coupling between the electron-rich region and LUMO molecular orbitals is required for charge transfer to be effective. Therefore, knowing in advance the energy of electrons in the gap region may allow more effective design of the catalysts for their interaction with specific molecules.

Lastly, after elucidating geometric and electronic effects arising inside metallic nanopores and their influence on the reactivity of electron-rich regions, the work focused on the incorporation of electron-rich regions as building blocks in a three-dimensional nanostructured material. In chapter six, "Small-molecule activation driven by confinement effects", a nanostructured material featuring electron-rich region is presented, and its reactivity is evaluated. The material consists of NPG decorated with Pt-nanoparticles. Electron-rich regions are formed in this system through close interaction between the Pt-cluster and carbon nanotubes in the NPG (separation ~ 5.5Å). In the first part, O_2, CO, and N_2 molecules are adsorbed on a Pt_{26} cluster with and without the presence of electron-rich regions. Charges transferred to molecules in electron-rich regions during adsorption are up to 35% larger compared to those of molecules adsorbed on the cluster with no presence of electron-rich regions. Also, bond-lengths of adsorbed molecules are up to 0.84% longer. Therefore, molecules in electron-rich regions exhibit weaker molecular bonds, and smaller barriers are expected to be required for their dissociation.

Subsequently, AIMD simulations of O_2 molecules interacting with the proposed Pt/NPG catalysts are performed. These simulations are compared to those of O_2 molecules interacting with a Pt_{26}/Graphite system at the same (T, P) conditions. Pt_{26}/Graphite represents an ordered carbon-based material with larger pore sizes than those in NPG (~ 1nm vs. ~0.56 nm in NPG), and consequently, it does not possess electron-rich regions. A clear effect of electron-rich regions on the reactivity of platinum-decorated mesoporous carbon is observed. Firstly, it may help by allowing a wider range of electrons being transferred to adsorbed molecules, which generates longer bond-length oscillations that facilitate the molecular dissociation. Additionally, at higher temperatures, larger migration of electrons to the confined region between the Pt-cluster and the CNT may be possible, which results in adsorbed molecules with more negative charges. The additional charge goes to the antibonding LUMO of the O_2 molecule, facilitating the breaking of its O-O bond.

Finally, the dehydrogenation of methane is also studied on the proposed Pt/NPG system using AIMD simulations. In this case, the calculated ($LUMO_{Molecule} - E_{Fermi\text{-}Catalyst}$) barrier is significantly high, corresponding to 4.4 eV. As a result, electron-rich regions do not significantly affect the charge density of methane molecules. However, smaller times are required to observe molecular adsorption on Pt_{22}/NPG than on Pt_{26}/Graphite, which may be related to the *confined* nature of the electron-rich regions in NPG. Ordered Pt/NPG structures, such as the one proposed on this work, may display enhanced reactivity, even when electron-rich regions do not interact with the molecules of interest due to the good dispersion of Pt-clusters on the material and to small pore sizes that may increase the frequency of interaction between catalysts and molecules.

In summary, the main hypothesis of this work –reactions taking place in electron-rich environments require lower energy barriers- is proved in chapter three, electronic and geometric effects arising in electron-rich regions are investigated in chapters four and five, and lastly, a novel nanostructured material exhibiting electron-rich regions is proposed and tested towards the reaction of gas-phase molecules in chapter six. The Pt/NPG catalyst proposed in this work is a good candidate for the efficient dissociation of molecules in gas phase. Its reactivity may be tailored by effectively coupling the energy of electrons in electron-rich regions with that of antibonding orbitals of molecules of interest. Additionally, the ordered nature of the catalyst and its small pore size may also have a geometric effect on reactivity even in cases when electron-rich regions do not effectively interact with the LUMO of molecules.

Future work can focus on evaluating the effect of nanoparticle size and/or crystallographic phases on the reactivity of metal-decorated NPG. As found in chapter four, the local geometry of electron-rich regions has an effect on adsorption energies of adsorbates and activation barriers for their dissociation. Furthermore, the incorporation of electron-rich regions into different ordered porous structures can be investigated. In that way, the effect of the morphology of the support material can be also taken into account. Also, reaction rates and frequency factors of specific reactions can be

calculated in materials featuring electron-rich regions. In this way, their effect can be quantified by comparing with values in other ordered mesoporous materials. Finally, diffusion of gas-phase reactants and products may be evaluated in the proposed nanocatalysts; this would allow proposing structural modifications on the material to minimize mass transport limitations.

This work was developed in its entirety using computational quantum-based simulations. Current computational packages allow studying molecular processes in detail, and are able to use a small number of suitable descriptors to describe relevant processes (e.g., total energies, activations barriers for reactions, reaction rates, etc.). However, quantum-based methods use a number of approximations and do not solve exactly the *Schrödinger* equation. Consequently, errors related to this uncertainty are expected. Fortunately, knowing the limitations of each specific method (Hartree-based methods, DFT, AIMD) and choosing suitable simulation parameters for the system under consideration (specific functionals, basis sets, etc.), generally results in good accuracies for the prediction of physical properties of materials.[37] Combined experimental and theoretical approaches hold the key to accelerated advancements in different scientific areas, including that of catalysis.

REFERENCES

1 Polshettiwar, V. Nanomaterials in catalysis . Edited by Philippe Serp and Karine Philippot. *Angewandte Chemie International Edition* **52**, 11199-11199, (2013).

2 Shiju, N. R. & Guliants, V. V. Recent developments in catalysis using nanostructured materials. *Applied Catalysis A: General* **356**, 1-17, (2009).

3 Zhao, H., Liu, X. & Tse, S. Control of nanoparticle size and agglomeration through electric-field-enhanced flame synthesis. *J Nanopart Res* **10**, 907-923, (2008).

4 Kida, S., Ichiji, M., Watanabe, J. & Hirasawa, I. Particle size distribution and shape control of Au nanoparticles used for particle gun. *Front. Chem. Sci. Eng.* **7**, 60-64, (2013).

5 Sahu, P. & Prasad, B. L. V. Fine control of nanoparticle sizes and size distributions: temperature and ligand effects on the digestive ripening process. *Nanoscale* **5**, 1768-1771, (2013).

6 Corma, A., Diaz-Cabanas, M. J., Jorda, J. L., Martinez, C. & Moliner, M. High-throughput synthesis and catalytic properties of a molecular sieve with 18- and 10-member rings. *Nature* **443**, 842-845, (2006).

7 Xiao, F.-S., Wang, L., Yin, C., Lin, K., Di, Y., Li, J., Xu, R., Su, D. S., Schlögl, R., Yokoi, T. & Tatsumi, T. Catalytic properties of hierarchical mesoporous zeolites templated with a mixture of small organic ammonium salts and mesoscale cationic polymers. *Angewandte Chemie International Edition* **45**, 3090-3093, (2006).

8 Jacobsen, C. J. H., Madsen, C., Houzvicka, J., Schmidt, I. & Carlsson, A. Mesoporous zeolite single crystals. *Journal of the American Chemical Society* **122**, 7116-7117, (2000).

9 Corma, A. State of the art and future challenges of zeolites as catalysts. *Journal of Catalysis* **216**, 298-312, (2003).

10 Schoeman, B. J., Sterte, J. & Otterstedt, J. E. Colloidal zeolite suspensions. *Zeolites* **14**, 110-116, (1994).

11 Zhen, M. & Sheng, D. ChemInform Abstract: Development of novel supported gold catalysts: a materials perspective. *ChemInform* **42**, (2011).

12 Flytzani-Stephanopoulos, M. & Gates, B. C. Atomically dispersed supported metal catalysts. *Annual Review of Chemical and Biomolecular Engineering* **3**, 545-574, (2012).

13 Veerakumar, P., Velayudham, M., Lu, K.-L. & Rajagopal, S. Highly dispersed silica-supported nanocopper as an efficient heterogeneous catalyst: application in the synthesis of 1,2,3-triazoles and thioethers. *Catalysis Science & Technology* **1**, 1512-1525, (2011).

14 Yu, K. M. K., Steele, A. M., Zhu, J., Fu, Q. & Tsang, S. C. Synthesis of well-dispersed nanoparticles within porous solid structures using surface-tethered surfactants in supercritical CO2. *Journal of Materials Chemistry* **13**, 130-134, (2003).

15 Li, J., Shen, B., Hong, Z., Lin, B., Gao, B. & Chen, Y. A facile approach to synthesize novel oxygen-doped g-C3N4 with superior visible-light photoreactivity. *Chemical Communications* **48**, 12017-12019, (2012).

16 Gokhale, R., Unni, S. M., Puthusseri, D., Kurungot, S. & Ogale, S. Synthesis of an efficient heteroatom-doped carbon electro-catalyst for oxygen reduction reaction by pyrolysis of protein-rich pulse flour cooked with SiO2 nanoparticles. *Physical Chemistry Chemical Physics* **16**, 4251-4259, (2014).

17 Wang, L., Ambrosi, A. & Pumera, M. "Metal-free" catalytic oxygen reduction reaction on heteroatom-doped graphene is caused by trace metal impurities. *Angewandte Chemie International Edition* **52**, 13818-13821, (2013).

18 Peng, H., Mo, Z., Liao, S., Liang, H., Yang, L., Luo, F., Song, H., Zhong, Y. & Zhang, B. High performance Fe- and N- doped carbon catalyst with graphene structure for oxygen reduction. *Sci. Rep.* **3**, (2013).

19 Gong, K., Du, F., Xia, Z., Durstock, M. & Dai, L. Nitrogen-doped carbon nanotube arrays with high electrocatalytic activity for oxygen reduction. *Science* **323**, 760-764, (2009).

20 Tylianakis, E., Psofogiannakis, G. M. & Froudakis, G. E. Li-doped pillared graphene oxide: a graphene-based nanostructured material for hydrogen storage. *The Journal of Physical Chemistry Letters* **1**, 2459-2464, (2010).

21 Martinez de la Hoz, J. M. & Balbuena, P. B. Local surface structure effect on reactivity of molecules confined between metallic surfaces. *Physical Chemistry Chemical Physics* (2013).

22 Martínez de la Hoz, J. M. & Balbuena, P. B. Geometric and electronic confinement effects on catalysis. *The Journal of Physical Chemistry C* **115**, 21324-21333, (2011).

23 Martinez de la Hoz, J. M., Ramirez-Caballero, G. E. & Balbuena, P. B. Characterization of electronic states inside metallic nanopores. *The Journal of Physical Chemistry C* **117**, 18406-18413, (2013).

24 Pérez-González, O., Zabala, N. & Aizpurua, J. Optical characterization of charge transfer and bonding dimer plasmons in linked interparticle gaps. *New Journal of Physics* **13**, 083013 (2011).

25 Ramírez-Caballero, G., Martínez de la Hoz, J. M. & Balbuena, P. B. p–n junction at the interface between metallic systems. *The Journal of Physical Chemistry Letters* **3**, 818-825, (2012).

26 Ramírez-Caballero, G. E. & Balbuena, P. B. Confinement-induced changes in magnetic behavior of a Ti monolayer on Pt. *Chemical Physics Letters* **507**, 117-121, (2011).

27 Ramirez-Caballero, G. E., Mathkari, A. & Balbuena, P. B. Confinement-induced polymerization of ethylene. *The Journal of Physical Chemistry C* **115**, 2134-2139, (2011).

28 Wu, L., Duan, H., Bai, P., Bosman, M., Yang, J. K. W. & Li, E. Fowler–Nordheim tunneling induced charge transfer plasmons between nearly touching nanoparticles. *ACS Nano* **7**, 707-716, (2012).

29 Zhao, K., Troparevsky, M. C., Xiao, D., Eguiluz, A. G. & Zhang, Z. Electronic coupling and optimal gap size between two metal nanoparticles. *Physical Review Letters* **102**, 186804 (2009).

30 Zuloaga, J., Prodan, E. & Nordlander, P. Quantum description of the plasmon resonances of a nanoparticle dimer. *Nano Letters* **9**, 887-891, (2009).

31 Ramirez-Caballero, G. E. & Balbuena, P. B. Confinement effects on alloy reactivity. *Physical Chemistry Chemical Physics* **12**, 12466-12471, (2010).

32 Zicovich-Wilson, C. M., Corma, A. & Viruela, P. Electronic confinement of molecules in microscopic pores. A new concept which contributes to the explanation of the catalytic activity of zeolites. *The Journal of Physical Chemistry* **98**, 10863-10870, (1994).

33 Deutschmann, O. Modeling and simulation of heterogeneous catalytic reactions: from the molecular process to the technical system. (Wiley-VCH, 2011).

34 Sprinborg, M. Methods of electronic structure calculation: from molecules to solids. (John Wiley & Sons, Ltd, 2000).

35 Grob, A. Theoretical surface science: a microscopic perspective. (Springer, 2003).

36 Rode, B. M., Hofer, T. S. & Kugler, M. D. The basics of theoretical and computational chemistry. (WILEY-VCH Verlag GmbH & Co., 2007).

37 Sholl, D. & Steckel, J. A. Density functional theory: a practical introduction. (John Wiley & Sons, Inc, 2009).

38 Cramer, C. J. & Truhlar, D. G. Density functional theory for transition metals and transition metal chemistry. *Physical Chemistry Chemical Physics* **11**, 10757-10816, (2009).

39 Santen, R. A. v. & Sautet, P. Computational methods in catalysis and materials science. (Wiley-VCH, 2009).

40 Hohenberg, P. & Kohn, W. Inhomogeneous electron gas. *Physical Review* **136**, B864-B871 (1964).

41 Becke, A. D. Density-functional exchange-energy approximation with correct asymptotic behavior. *Physical Review A* **38**, 3098-3100 (1988).

42 Perdew, J. P. Density-functional approximation for the correlation energy of the inhomogeneous electron gas. *Physical Review B* **33**, 8822-8824 (1986).

43 Lee, C., Yang, W. & Parr, R. G. Development of the Colle-Salvetti correlation-energy formula into a functional of the electron density. *Physical Review B* **37**, 785-789 (1988).

44 Perdew, J. P., Chevary, J. A., Vosko, S. H., Jackson, K. A., Pederson, M. R., Singh, D. J. & Fiolhais, C. Atoms, molecules, solids, and surfaces: applications of the generalized gradient approximation for exchange and correlation. *Physical Review B* **46**, 6671-6687 (1992).

45 Perdew, J. P., Burke, K. & Ernzerhof, M. Generalized gradient approximation made simple. *Physical Review Letters* **77**, 3865-3868 (1996).

46 Kohn, W., Becke, A. D. & Parr, R. G. Density functional theory of electronic structure. *The Journal of Physical Chemistry* **100**, 12974-12980, (1996).

47 Becke, A. D. Density-functional thermochemistry. III. The role of exact exchange. *The Journal of Chemical Physics* **98**, 5648-5652, (1993).

48 Stephens, P. J., Devlin, F. J., Chabalowski, C. F. & Frisch, M. J. Ab initio calculation of vibrational absorption and circular dichroism spectra using density functional force fields. *The Journal of Physical Chemistry* **98**, 11623-11627, (1994).

49 Adamo, C. & Barone, V. Toward reliable adiabatic connection models free from adjustable parameters. *Chemical Physics Letters* **274**, 242-250, (1997).

50 Ernzerhof, M. & Scuseria, G. E. Assessment of the Perdew–Burke–Ernzerhof exchange-correlation functional. *The Journal of Chemical Physics* **110**, 5029-5036, (1999).

51 Nilsson, A., Lars, G. M. P. & Nørskov, J. Chemical bonding at surfaces and interfaces. (Elsevier, 2008).

52 Ramirez-Caballero, G. E. & Balbuena, P. B. Effects of confinement on oxygen adsorbed between Pt(111) surfaces. *The Journal of Physical Chemistry C* **113**, 7851-7856, (2009).

53 Ramírez-Caballero, G. E. & Balbuena, P. B. Confinement-induced changes in magnetic behavior of a Ti monolayer on Pt. *Chemical Physics Letters* **507**, 117-121.

54 Mahmoud, M. A., Saira, F. & El-Sayed, M. A. Experimental evidence for the nanocage effect in catalysis with hollow nanoparticles. *Nano Letters* **10**, 3764-3769, (2010).

55 Okawa, Y., Mandal, S. K., Hu, C., Tateyama, Y., Goedecker, S., Tsukamoto, S., Hasegawa, T., Gimzewski, J. K. & Aono, M. Chemical wiring and soldering toward all-molecule electronic circuitry. *J. Am. Chem. Soc.* **133**, 8227-8233 (2011).

56 Mandal, S. K., Okawa, Y., Hasegawa, T. & Aono, M. Rate-determining factors in the chain polymerization of molecules initiated by local single-molecule excitation. *ACS Nano* **5**, 2779-2786 (2011).

57 Aballe, L., Barinov, A., Locatelli, A., Heun, S. & Kiskinova, M. Tuning surface reactivity via electron quantum confinement. *Physical Review Letters* **93**, 196103 (2004).

58 Hammer, B. & Nørskov, J. K. *Catalysis*. Vol. 45 71-129 (2000).

59 Greeley, J., Nørskov, J. K. & Mavrikakis, M. Electronic structure and catalysis on metal surfaces. *Annual Review Of Physical Chemistry* **53**, 319-348 (2002).

60 Stipe, B. C., Rezaei, M. A., Ho, W., Gao, S., Persson, M. & Lundqvist, B. I. Single-molecule dissociation by tunneling electrons. *Physical Review Letters* **78**, 4410-4413 (1997).

61 Eichler, A. & Hafner, J. Molecular precursors in the dissociative adsorption of O2 on Pt(111). *Physical Review Letters* **79**, 4481 (1997).

62 Hellman, A., Panas, I. & Gronbeck, H. NO_2 dissociation on Ag(111) revisited by theory. *The Journal of Chemical Physics* **128**, 104704-104706 (2008).

63 Schmatloch, V. & Kruse, N. Adsorption and reaction of CO, NO and mixtures of CO/NO on Rh(110). *Surface Science* **269-270**, 488-494 (1992).

64 Dahlgren, D. & Hemminger, J. C. Decomposition of NO_2 to NO and O on Pt(111). *Surface Science* **123**, L739-L742 (1982).

65 Bartram, M. E., Windham, R. G. & Koel, B. E. The molecular adsorption of nitrogen dioxide on Pt(111) studied by temperature programmed desorption and vibrational spectroscopy. *Surface Science* **184**, 57-74 (1987).

66 Schwalke, U., Parmeter, J. E. & Weinberg, W. H. Vibrational spectra of chemisorbed NO_2 and condensed N_2O_4 on the Ru(001) surface. *The Journal of Chemical Physics* **84**, 4036-4042 (1986).

67 Jirsak, T., Dvorak, J. & Rodriguez, J. A. Adsorption of NO_2 on Rh(111) and Pd/Rh(111): photoemission studies. *Surface Science* **436**, L683-L690 (1999).

68 Bare, S. R., Griffiths, K., Lennard, W. N. & Tang, H. T. Generation of atomic oxygen on Ag(111) and Ag(110) using NO_2: a TPD, LEED, HREELS, XPS and NRA study. *Surface Science* **342**, 185-198 (1995).

69 Polzonetti, G., Alnot, P. & Brundle, C. R. The adsorption and reactions of NO_2 on the Ag(111) surface: I. XPS/UPS and annealing studies between 90 and 300 K. *Surface Science* **238**, 226-236 (1990).

70 Brown, W. A., Gardner, P. & King, D. A. The adsorption of NO_2 on Ag(111) : a low temperature RAIRS study. *Surface Science* **330**, 41-47 (1995).

71 Chen, H.-L., Wu, S.-Y., Chen, H.-T., Chang, J.-G., Ju, S.-P., Tsai, C. & Hsu, L.-C. Theoretical study on adsorption and dissociation of NO_2 molecule on Fe(111) surface. *Langmuir* **26**, 7157-7164, (2010).

72 Bronsted, J. N. Acid and basic catalysis. *Chemical Reviews* **5**, 231-338, (1928).

73 Evans, M. G. & Polanyi, M. Inertia and driving force of chemical reactions. *Transactions of the Faraday Society* **34**, 11-24 (1938).

74 Nørskov, J. K., Bligaard, T., Logadottir, A., Bahn, S., Hansen, L. B., Bollinger, M., Bengaard, H., Hammer, B., Sljivancanin, Z., Mavrikakis, M., Xu, Y., Dahl, S. & Jacobsen, C. J. H. Universality in heterogeneous catalysis. *Journal of Catalysis* **209**, 275-278 (2002).

75 Pallassana, V. & Neurock, M. Electronic factors governing ethylene hydrogenation and dehydrogenation activity of pseudomorphic PdML/Re(0001), PdML/Ru(0001), Pd(111), and PdML/Au(111) surfaces. *Journal of Catalysis* **191**, 301-317 (2000).

76 Liu, Z. P. & Hu, P. General trends in CO dissociation on transition metal surfaces. *Journal of Chemical Physics* **114**, 8244-8247 (2001).

77 Logadottir, A., Rod, T. H., Nørskov, J. K., Hammer, B., Dahl, S. & Jacobsen, C. J. H. The Brønsted-Evans-Polanyi relation and the volcano plot for ammonia synthesis over transition metal catalysts. *Journal of Catalysis* **197**, 229-231 (2001).

78 Wang, S., Temel, B., Shen, J., Jones, G., Grabow, L., Studt, F., Bligaard, T., Abild-Pedersen, F., Christensen, C. & Nørskov, J. Universal Brønsted-Evans-Polanyi relations for C–C, C–O, C–N, N–O, N–N, and O–O dissociation reactions. *Catalysis Letters* **141**, 370-373, (2011).

79 Michaelides, A., Liu, Z. P., Zhang, C. J., Alavi, A., King, D. A. & Hu, P. Identification of general linear relationships between activation energies and enthalpy changes for dissociation reactions at surfaces. *Journal of the American Chemical Society* **125**, 3704-3705, (2003).

80 Chen, S., Gasteiger, H. A., Hayakawa, K., Tada, T. & Shao-Horn, Y. Platinum-alloy cathode catalyst degradation in proton exchange membrane fuel cells: nanometer-scale compositional and morphological changes. *J. Electrochem. Soc.* **157**, A82-A97, (2010).

81 Mani, P., Srivastava, R. & Strasser, P. Dealloyed binary PtM3 (M = Cu, Co, Ni) and ternary PtNi3M (M = Cu, Co, Fe, Cr) electrocatalysts for the oxygen

reduction reaction: Performance in polymer electrolyte membrane fuel cells. *J. Power Sources* **196**, 666-673, (2011).

82 Shao, M. H., Shoemaker, K., Peles, A., Kaneko, K. & Protsailo, L. Pt Mono layer on porous Pd-Cu alloys as oxygen reduction electrocatalysts. *Journal of the American Chemical Society* **132**, 9253-9255, (2010).

83 Principi, E., Witkowska, A., Dsoke, S., Marassi, R. & Di Cicco, A. An XAS experimental approach to study low Pt content electrocatalysts operating in PEM fuel cells. *Physical Chemistry Chemical Physics* **11**, 9987-9995, (2009).

84 Erlebacher, J., Aziz, M. J., Karma, A., Dimitrov, N. & Sieradzki, K. Evolution of nanoporosity in dealloying. *Nature* **410**, 450-453 (2001).

85 Policastro, S. A., Carnahan, J. C., Zangari, G., Bart-Smith, H., Seker, E., Begley, M. R., Reed, M. L., Reynolds, P. F. & Kelly, R. G. Surface diffusion and dissolution kinetics in the electrolyte-metal interface. *J. Electrochem. Soc.* **157**, C328-C337, (2010).

86 Liu, Y., Bliznakov, S. & Dimitrov, N. Factors controlling the less noble metal retention in nanoporous structures processed by electrochemical dealloying. *J. Electrochem. Soc.* **157**, K168-K176, (2010).

87 Kresse, G. & Furthmüller, J. Efficient iterative schemes for ab initio total-energy calculations using a plane-wave basis set. *Physical Review B* **54**, 11169 (1996).

88 Kresse, G. & Furthmuller, J. Efficiency of ab-initio total energy calculations for metals and semiconductors using a plane-wave basis set. *Computational Materials Science* **6**, 15-50 (1996).

89 Kresse, G. & Hafner, J. Ab initio molecular dynamics for open-shell transition metals. *Physical Review B* **48**, 13115 (1993).

90 Kresse, G. & Hafner, J. Ab initio molecular dynamics for liquid metals. *Physical Review B* **47**, 558 (1993).

91 Kresse, G. & Hafner, J. Ab initio molecular-dynamics simulation of the liquid-metal; amorphous-semiconductor transition in germanium. *Physical Review B* **49**, 14251 (1994).

92 Hammer, B., Hansen, L. & Nørskov, J. K. Improved adsorption energetics within density-functional theory using revised Perdew-Burke-Ernzerhof functionals. *Physical Review B* **59**, 7413-7421.

93 Blöchl, P. E. Projector augmented-wave method. *Physical Review B* **50**, 17953 (1994).

94 Kresse, G. & Joubert, D. From ultrasoft pseudopotentials to the projector augmented-wave method. *Physical Review B* **59**, 1758 (1999).

95 Monkhorst, H. J. & Pack, J. D. Special points for Brillouin-zone integrations. *Physical Review B* **13**, 5188 (1976).

96 Henkelman, G. & Jonsson, H. Improved tangent estimate in the nudged elastic band method for finding minimum energy paths and saddle points. *The Journal of Chemical Physics* **113**, 9978-9985 (2000).

97 Henkelman, G., Uberuaga, B. P. & Jonsson, H. A climbing image nudged elastic band method for finding saddle points and minimum energy paths. *The Journal of Chemical Physics* **113**, 9901-9904 (2000).

98 Sheppard, D., Terrell, R. & Henkelman, G. Optimization methods for finding minimum energy paths. *The Journal of Chemical Physics* **128**, 134106-134110 (2008).

99 Henkelman, G., Arnaldsson, A. & Jónsson, H. A fast and robust algorithm for Bader decomposition of charge density. *Computational Materials Science* **36**, 354-360 (2006).

100 Sanville, E., Kenny, S. D., Smith, R. & Henkelman, G. Improved grid-based algorithm for Bader charge allocation. *Journal of Computational Chemistry* **28**, 899-908 (2007).

101 Kittel, C. Introduction to solid state physics. 4th. edn, (Wiley, 1986).

102 Marek, G. & et al. Ab initio density-functional study of NO on close-packed transition and noble metal surfaces: I. Molecular adsorption. *Journal of Physics: Condensed Matter* **18**, 13 (2006).

103 Marek, G. & et al. CO adsorption on close-packed transition and noble metal surfaces: trends from ab initio calculations. *Journal of Physics: Condensed Matter* **16**, 1141 (2004).

104 Eichler, A., Mittendorfer, F. & Hafner, J. Precursor-mediated adsorption of oxygen on the (111) surfaces of platinum-group metals. *Physical Review B* **62**, 4744 (2000).

105 Gland, J. L., Sexton, B. A. & Fisher, G. B. Oxygen interactions with the Pt(111) surface. *Surface Science* **95**, 587-602 (1980).

106 Lehwald, S., Ibach, H. & Steininger, H. Overtones and multiphonon processes in vibration spectra of adsorbed molecules. *Surface Science* **117**, 342-351 (1982).

107 Ou, L., Yang, F., Liu, Y. & Chen, S. First-principle study of the adsorption and dissociation of O2 on Pt(111) in acidic media. *The Journal of Physical Chemistry C* **113**, 20657-20665, (2009).

108 Li, T. & Balbuena, P. B. Computational studies of the interactions of oxygen with platinum clusters. *J. Phys. Chem. B* **105**, 9943-9952 (2001).

109 Panas, I. & Siegbahn, P. A Theoretical study of peroxo and superoxo forms of molecular oxygen on metal surfaces. *Chem. Phys. Lett.* **153**, 458 (1988).

110 Hammer, B., Hansen, L. B. & Norskov, J. K. Improved adsorption energetics within density-functional theory using revised Perdew-Burke-Ernzerhof functionals. *Physical Review B* **59**, 7413 (1999).

111 Balbuena, P. B., Altomare, D., Agapito, L. A. & Seminario, J. M. Adsorption of oxygen on Pt-based clusters alloyed with Co, Ni, and Cr. *J. Phys. Chem. B* **107**, 13671-13680 (2003).

112 Ramirez-Caballero, G. E. & Balbuena, P. B. Confinement effects on alloy reactivity. *Phys. Chem. Chem. Phys.* **12**, 12466-12471 (2010).

113 Ramirez-Caballero, G. E. & Balbuena, P. B. Effect of confinement on oxygen adsorbed between Pt(111) surfaces. *J. Phys. Chem. C* **113**, 7851-7856 (2009).

114 Stirling, A. Oxygen-transfer reactions between 3d transition metals and N_2O and NO_2. *J. Am. Chem. Soc.* **124**, 4058-4067 (2002).

115 El-Sayed, M. Some interesting properties of metals confined in time and nanometer space of different shapes. *Acc. Chem. Res.* **34**, 257-264 (2001).

116 Pan, X. L. & Bao, X. H. The effects of confinement inside carbon nanotubes on catalysis. *Accounts Chem. Res.* **44**, 553-562, (2011).

117 Centi, G. & Perathoner, S. Creating and mastering nano-objects to design advanced catalytic materials. *Coord. Chem. Rev.* **255**, 1480-1498, (2011).

118 Kidder, M. K., Chaffee, A. L., Nguyen, M. H. T. & Buchanan, A. C. Pyrolysis of phenethyl phenyl ether tethered in mesoporous silica. Effects of confinement and surface spacer molecules on product selectivity. *J. Org. Chem.* **76**, 6014-6023, (2011).

119 Linic, S., Christopher, P. & Ingram, D. B. Plasmonic-metal nanostructures for efficient conversion of solar to chemical energy. *Nat. Mater.* **10**, 911-921, (2011).

120 Khlobystov, A. N. Carbon nanotubes: from nano test tube to nano-reactor. *Acs Nano* **5**, 9306-9312, (2011).

121 Cejka, J., Centi, G., Perez-Pariente, J. & Roth, W. J. Zeolite-based materials for novel catalytic applications: Opportunities, perspectives and open problems. *Catal. Today* **179**, 2-15, (2012).

122 Santiso, E. E., George, A. M., Turner, C. H., Kostov, M. K., Gubbins, K. E., Buongiorno-Nardelli, M. & Sliwinska-Bartkowiak, M. Adsorption and catalysis: The effect of confinement on chemical reactions. *Appl. Surf. Sci.* **252**, 766-777, (2005).

123 Marquez, F., Garcia, H., Palomares, E., Fernandez, L. & Corma, A. Spectroscopic evidence in support of the molecular orbital confinement concept: case of anthracene incorporated in zeolites. *J. Am. Chem. Soc.* **122**, 6520-6521 (2000).

124 Planelles, J., ZicovichWilson, C., Jaskolski, W. & Corma, A. Semiempirical hamiltonians for spatially confined pi-electron systems. *Int. J. Quantum Chem.* **60**, 971-981 (1996).

125 Zicovich-Wilson, C. M. & Corma, A. Electronic confinement of molecules in microscopic pores. A new concept which contributes to explain the catalytic activity of zeolites. *J. Phys. Chem.* **98**, 10863-10870 (1994).

126 Chiang, H. & Bhan, A. Catalytic consequences of hydroxyl group location on the kinetics of n-hexane hydroisomerization over acidic zeolites. *Journal of Catalysis* **283**, 98-107, (2011).

127 Carr, R. T., Neurock, M. & Iglesia, E. Catalytic consequences of acid strength in the conversion of methanol to dimethyl ether. *Journal of Catalysis* **278**, 78-93, (2011).

128 Bhan, A., Gounder, R., Macht, J. & Iglesia, E. Entropy considerations in monomolecular cracking of alkanes on acidic zeolites. *Journal of Catalysis* **253**, 221-224, (2008).

129 Gu, Z. & Balbuena, P. B. Absorption of atomic oxygen into subsurfaces of Pt(100) and Pt(111): Density functional theory study. *J. Phys. Chem. C* **111**, 9877-9883 (2007).

130 Gu, Z. & Balbuena, P. B. Chemical environment effects on the atomic oxygen absorption into Pt(111) subsurfaces. *J. Phys. Chem. C* **111**, 17388-17396 (2007).

131 Kuzume, A., Herrero, E. & Feliu, J. M. Oxygen reduction on stepped platinum surfaces in acidic media. *J. Electroanal. Chem.* **599**, 333-343, (2007).

132 Bligaard, T. & Nørskov, J. K. in Chemical bonding at surfaces and interfaces 255-321 (Elsevier, 2008).

133 Danckwerts, M. & Novotny, L. Optical frequency mixing at coupled gold nanoparticles. *Physical Review Letters* **98**, 026104 (2007).

134 Marinica, D. C., Kazansky, A. K., Nordlander, P., Aizpurua, J. & Borisov, A. G. Quantum plasmonics: nonlinear effects in the field enhancement of a plasmonic nanoparticle dimer. *Nano Letters* **12**, 1333-1339, (2012).

135 Romero, I., Aizpurua, J., Bryant, G. W. & García De Abajo, F. J. Plasmons in nearly touching metallic nanoparticles: singular response in the limit of touching dimers. *Opt. Express* **14**, 9988-9999 (2006).

136 Esteban, R., Borisov, A., Nordlander, P. & Aizpurua, J. Bridging quantum and classical plasmonics with a quantum-corrected model. *Nature Communications* **3**, 825, (2012).

137 Savage, K., Hawkeye, M., Esteban, R., Borisov, A., Aizpurua, J. & Baumberg, J. Revealing the quantum regime in tunnelling plasmonics. *Nature* **491**, 574-577, (2012).

138 Liu, L., Yoo, S. H. & Park, S. Synthesis of vertically aligned hollow platinum nanotubes with single crystalline nanoflakes. *Chemistry of Materials* **22**, 2681-2684, (2010).

139 Frisch, M. J., Trucks, G. W., Schlegel, H. B., Scuseria, G. E., Robb, M. A., Cheeseman, J. R., Scalmani, G., Barone, V., Mennucci, B., Petersson, G. A., Nakatsuji, H., Caricato, M., Li, X., Hratchian, H. P., Izmaylov, A. F., Bloino, J., Zheng, G., Sonnenberg, J. L., Hada, M., Ehara, M., Toyota, K., Fukuda, R., Hasegawa, J., Ishida, M., Nakajima, T., Honda, Y., Kitao, O., Nakai, H., Vreven, T., Montgomery, J., J. A.;, Peralta, J. E., Ogliaro, F., Bearpark, M., Heyd, J. J., Brothers, E., Kudin, K. N., Staroverov, V. N., Kobayashi, R., Normand, J., Raghavachari, K., Rendell, A., Burant, J. C., Iyengar, S. S., Tomasi, J., Cossi, M., Rega, N., Millam, J. M., Klene, M., Knox, J. E., Cross, J. B., Bakken, V., Adamo, C., Jaramillo, J., Gomperts, R., Stratmann, R. E., Yazyev, O., Austin, A. J., Cammi, R., Pomelli, C., Ochterski, J. W., Martin, R. L., Morokuma, K., Zakrzewski, V. G., Voth, G. A., Salvador, P., Dannenberg, J. J., Dapprich, S., Daniels, A. D., Farkas, Ö., Foresman, J. B., Ortiz, J. V., Cioslowski, J. & Fox, D. J. Gaussian 09. Revision A.1. *Wallingford CT* (2009).

140 Singh, U. C. & Kollman, P. A. An approach to computing electrostatic charges for molecules. *Journal of Computational Chemistry* **5**, 129-145, (1984).

141 Zhao, Y., Schultz, N. E. & Truhlar, D. G. Design of density functionals by combining the method of constraint satisfaction with parametrization for thermochemistry, thermochemical kinetics, and noncovalent interactions. *Journal of Chemical Theory and Computation* **2**, 364-382, (2006).

142 Head-Gordon, M. & Head-Gordon, T. Analytic MP2 frequencies without fifth-order storage. Theory and application to bifurcated hydrogen bonds in the water hexamer. *Chemical Physics Letters* **220**, 122-128, (1994).

143 Frisch, M. J., Head-Gordon, M. & Pople, J. A. Semi-direct algorithms for the MP2 energy and gradient. *Chemical Physics Letters* **166**, 281-289, (1990).

144 Frisch, M. J., Head-Gordon, M. & Pople, J. A. A direct MP2 gradient method. *Chemical Physics Letters* **166**, 275-280, (1990).

145 Sæbø, S. & Almlöf, J. Avoiding the integral storage bottleneck in LCAO calculations of electron correlation. *Chemical Physics Letters* **154**, 83-89, (1989).

146 Head-Gordon, M., Pople, J. A. & Frisch, M. J. MP2 energy evaluation by direct methods. *Chemical Physics Letters* **153**, 503-506, (1988).

147 Møller, C. & Plesset, M. S. Note on an approximation treatment for many-electron systems. *Physical Review* **46**, 618-622 (1934).

148 Pople, J. A., Head-Gordon, M. & Raghavachari, K. Quadratic configuration interaction. A general technique for determining electron correlation energies. *The Journal of Chemical Physics* **87**, 5968-5975 (1987).

149 Hay, P. J. & Wadt, W. R. Ab initio effective core potentials for molecular calculations. Potentials for the transition metal atoms Sc to Hg. *The Journal of Chemical Physics* **82**, 270-283 (1985).

150 Roy, L. E., Hay, P. J. & Martin, R. L. Revised basis sets for the LANL effective core potentials. *Journal of Chemical Theory and Computation* **4**, 1029-1031, (2008).

151 Michaelson, H. B. The work function of the elements and its periodicity. *Journal of Applied Physics* **48**, 4729-4733 (1977).

152 Dimitrakakis, G. K., Tylianakis, E. & Froudakis, G. E. Pillared graphene: a new 3-D network nanostructure for enhanced hydrogen storage. *Nano Letters* **8**, 3166-3170, (2008).

153 Zhu, Y., Li, L., Zhang, C., Casillas, G., Sun, Z., Yan, Z., Ruan, G., Peng, Z., Raji, A.-R. O., Kittrell, C., Hauge, R. H. & Tour, J. M. A seamless three-

dimensional carbon nanotube graphene hybrid material. *Nat Commun* **3**, 1225, (2012).

154 Paul, R. K., Ghazinejad, M., Penchev, M., Lin, J., Ozkan, M. & Ozkan, C. S. Synthesis of a pillared graphene nanostructure: a counterpart of three-dimensional carbon architectures. *Small* **6**, 2309-2313, (2010).

155 Chorkendorff, I. & Niemantsverdriet, J. W. Concepts of modern catalysis and kinetics. (Wiley-VCH, 2007).

156 Du, F., Yu, D., Dai, L., Ganguli, S., Varshney, V. & Roy, A. K. Preparation of tunable 3D pillared carbon nanotube–graphene networks for high-performance capacitance. *Chemistry of Materials* **23**, 4810-4816, (2011).

157 Fan, Z., Yan, J., Zhi, L., Zhang, Q., Wei, T., Feng, J., Zhang, M., Qian, W. & Wei, F. A three-dimensional carbon nanotube/graphene sandwich and its application as electrode in supercapacitors. *Advanced Materials* **22**, 3723-3728, (2010).

158 Lin, J., Zhong, J., Bao, D., Reiber-Kyle, J. & Wang, W. Supercapacitors based on pillared graphene nanostructures. *Journal of Nanoscience and Nanotechnology* **12**, 1770-1775, (2012).

159 Lee, J. M., Choung, J. W., Yi, J., Lee, D. H., Samal, M., Yi, D. K., Lee, C.-H., Yi, G.-C., Paik, U., Rogers, J. A. & Park, W. I. Vertical pillar-superlattice array and graphene hybrid light emitting diodes. *Nano Letters* **10**, 2783-2788, (2010).

160 Ma, Y., Sun, L., Huang, W., Zhang, L., Zhao, J., Fan, Q. & Huang, W. Three-dimensional nitrogen-doped carbon nanotubes/graphene structure used as a metal-free electrocatalyst for the oxygen reduction reaction. *The Journal of Physical Chemistry C* **115**, 24592-24597, (2011).

161 Li, Y., Zhou, W., Wang, H., Xie, L., Liang, Y., Wei, F., Idrobo, J.-C., Pennycook, S. J. & Dai, H. An oxygen reduction electrocatalyst based on carbon nanotube-graphene complexes. *Nat Nano* **7**, 394-400, (2012).

162 Zhu, X., Ning, G., Fan, Z., Gao, J., Xu, C., Qian, W. & Wei, F. One-step synthesis of a graphene-carbon nanotube hybrid decorated by magnetic nanoparticles. *Carbon* **50**, 2764-2771, (2012).

163 Lee, D. H., Lee, J. A., Lee, W. J., Choi, D. S., Lee, W. J. & Kim, S. O. Facile fabrication and field emission of metal-particle-decorated vertical N-doped carbon nanotube/graphene hybrid films. *The Journal of Physical Chemistry C* **114**, 21184-21189, (2010).

164 Gálvez, M., Calvillo, L., Alegre, C., Sebastián, D., Suelves, I., Pérez-Rodríguez, S., Celorrio, V., Pastor, E., Pardo, J., Moliner, R. & Lázaro, M. Nanostructured carbon materials as supports in the preparation of direct methanol fuel cell electrocatalysts. *Catalysts* **3**, 671-682 (2013).

165 Ding, J., Chan, K.-Y., Ren, J. & Xiao, F.-s. Platinum and platinum–ruthenium nanoparticles supported on ordered mesoporous carbon and their electrocatalytic performance for fuel cell reactions. *Electrochimica Acta* **50**, 3131-3141, (2005).

166 Kong, L.-B., Li, H., Zhang, J., Luo, Y.-C. & Kang, L. Platinum catalyst on ordered mesoporous carbon with controlled morphology for methanol electrochemical oxidation. *Appl. Surf. Sci.* **256**, 6688-6693, (2010).

167 Ishii, A., Yamamoto, M., Asano, H. & Fujiwara, K. DFT calculation for adatom adsorption on graphene sheet as a prototype of carbon nanotube functionalization. *Journal of Physics: Conference Series* **100**, 052087 (2008).

168 Eichler, A. & Hafner, J. Molecular precursors in the dissociative adsorption of O2 on Pt(111). *Physical Review Letters* **79**, 4481-4484 (1997).

169 Marek, G., Andreas, E. & Jürgen, H. CO adsorption on close-packed transition and noble metal surfaces: trends from ab initio calculations. *Journal of Physics: Condensed Matter* **16**, 1141 (2004).

170 Stewart, R. B., Jacobsen, R. T. & Wagner, W. Thermodynamic properties of oxygen from the triple point to 300 K with pressures to 80 MPa. *Journal of Physical and Chemical Reference Data* **20**, 917-1021, (1991).

171 Xu, J., Zheng, A., Wang, X., Qi, G., Su, J., Du, J., Gan, Z., Wu, J., Wang, W. & Deng, F. Room temperature activation of methane over Zn modified H-ZSM-5 zeolites: Insight from solid-state NMR and theoretical calculations. *Chemical Science* **3**, 2932-2940, (2012).

172 An, W., Zeng, X. C. & Turner, C. H. First-principles study of methane dehydrogenation on a bimetallic Cu/Ni(111) surface. *The Journal of Chemical Physics* **131**, (2009).

173 Chen, A., Zhang, W., Li, X., Tan, D., Han, X. & Bao, X. One-pot encapsulation of Pt nanoparticles into the mesochannels of SBA-15 and their catalytic dehydrogenation of methylcyclohexane. *Catalysis Letters* **119**, 159-164, (2007).

174 Kresse, G. & Furthmüller, J. Efficiency of ab-initio total energy calculations for metals and semiconductors using a plane-wave basis set. *Computational Materials Science* **6**, 15-50, (1996).

175 Kresse, G. & Hafner, J. Ab initio molecular-dynamics simulation of the liquid-metal–amorphous-semiconductor transition in germanium. *Physical Review B* **49**, 14251-14269 (1994).

176 Hammer, B., Hansen, L. B. & Nørskov, J. K. Improved adsorption energetics within density-functional theory using revised Perdew-Burke-Ernzerhof functionals. *Physical Review B* **59**, 7413-7421 (1999).

177 Gil, V. Orbitals in chemistry: a modern guide for students. (Cambridge University Press, 2000).

178 Resasco, D. E. in Encyclopedia of Catalysis (John Wiley & Sons, Inc., 2002).